



CHAPTER 5

RECIPROCITY-EXPRESSION-BASED APPROACH FOR MUTUAL ADMITTANCE BETWEEN CPW-FED SLOTS ON CONDUCTOR-BACKED TWO-LAYER SUBSTRATES

5.1 INTRODUCTION

In this chapter, a computational strategy, based on a well-known reciprocity-based expression, is developed for finding the mutual admittance between CPW-fed slots on a two-layer parallel-plate substrate. The geometry is shown in Fig. 5.1.¹ The mutual admittance between the slots can be viewed as the sum of external and internal mutual admittances: the external mutual admittance is due to coupling that takes place in the half-space adjacent to the slots, while the internal mutual admittance is due to coupling inside the substrate.

The method for calculating mutual admittance that is developed here is intended to serve as a simpler alternative to a moment-method-based approach, yet of comparable accuracy. Moment-method-based techniques have been used for finding mutual coupling between various kinds of planar radiating elements, including CPW-fed slots on multi-layer dielectric substrates without a back conductor [38], rectangular centre-fed slots on planar substrates [57, 61], and microstrip-fed printed antennas [62–64]. Mutual coupling in planar multi-port circuits have similarly been accounted for [65].

Of particular interest amongst the above is the rigorous moment-method analysis of CPW-fed twin slot antennas on multi-layer dielectric substrates without a back plane in [38]. In order to obtain the two-port impedance-matrix (Z) parameters for a particular twin slot configuration, the

¹ It differs from the twin slots of Fig. 4.1 only in allowing for different radiating slot dimensions.

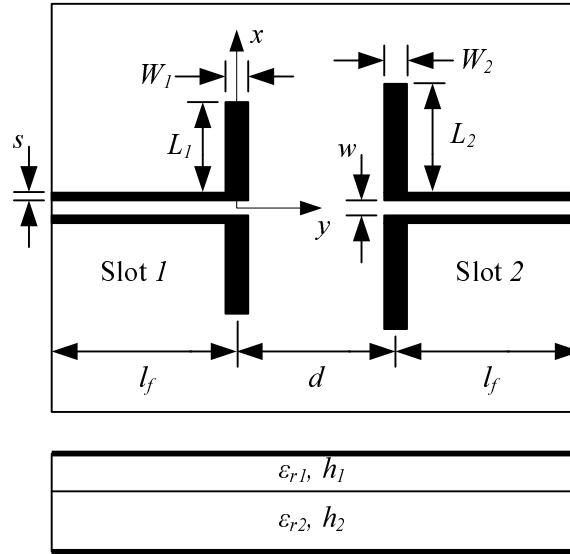


FIGURE 5.1: Top and side views of broadside (non-identical) CPW-fed twin slot antennas on conductor-backed two-layer substrate. $L_1, L_2 \equiv$ half-lengths and $W_1, W_2 \equiv$ widths of radiating slots; $d \equiv$ distance between radiating slots; $s \equiv$ slot width and $w \equiv$ centre strip width of feed lines; $h_1, h_2 \equiv$ dielectric layer heights; $\epsilon_{r1}, \epsilon_{r2} \equiv$ relative dielectric constants; $l_f \equiv$ feed line lengths. The ground plane containing the slots coincides with the plane $z = 0$. A coordinate system is defined with its origin at the centre of slot I ; the z axis points into the page.

moment method matrix equation is solved twice, once for an even excitation and once for an odd excitation (these labels refer to the phase relationship between the current sources placed at the terminals of each CPW-fed slot). Input impedances are calculated for each case, and used in simple algebraic equations to obtain the two-port Z parameters. Because of the symmetry of the twin slots, only two independent excitations are required (a more general procedure applied to non-symmetrical microstrip-fed planar dipoles can be found in [64]). A notable finding in [38] pertains to a simplification that involves removing the CPW feed lines and exciting the radiating slots by delta-gap current sources at their centres (this presumably involves forming single rectangular radiating slots from the two half-lengths of each of the former CPW-fed slots). The finding was that the phases of S parameters, and hence resonant frequencies, could only be predicted with sufficient accuracy for oscillator applications if the condition $\frac{w + 2s}{\lambda_{eff}} < \frac{1}{50}$ held, where λ_{eff} presumably is the wavelength of the slotline corresponding to the radiating slot – in other words if very narrow CPW feeds were used. This appears to be interpreted in [10] as support for the notion that network-based simplifications do not apply as well to CPW-fed slots as to slots fed by other means, and that a complete full-wave, finely-meshed analysis of both the radiating slots and their CPW feeds is necessary when characterizing CPW-fed twin slot and double-slot (*i.e.*, H-configured)



antennas.²

Iterative array design algorithms require that the mutual admittance between all possible slot pairs in the array be calculated during every iteration, *e.g.*, [35]. For example, a linear array of N slots requires $N(N-1)/2$ mutual admittance calculations per iteration.³ (In certain cases, the mutual coupling between slots that are far enough apart may be neglected.) Slot dimensions evolve over iterations until the algorithm converges to a solution that is satisfactory with respect to both the input impedance and aperture distribution requirements of the array. Carrying out a full moment-method analysis for each of these mutual admittance calculations would be very cumbersome.

In Chapter 1, it was noted that [35] reduces the problem of finding the mutual admittance between slots in a linear CPW-fed array on an electrically thin single-layer substrate to an equivalent problem that involves finding the mutual impedance between two wire dipoles in a homogeneous medium using a well-known variational formula derived for the latter purpose [18]. The Green's function of the substrate is not used. It was also observed that the validity of the relevant approximations and assumptions remains to be tested via the design of a non-uniform array subject to a stringent sidelobe level requirement; the approximations include replacing the array by its complementary strip-dipole array, and assuming a homogeneous medium with effective permittivity ϵ_{eff} , where ϵ_{eff} is the geometrical mean of the various slot effective permittivities. In the present work, no approximations regarding the inhomogeneous nature of the medium will be made; instead, the conductor-backed two-layer substrate will be rigorously accounted for by use of the appropriate Green's function.

The organization of the chapter is as follows. In Section 5.2, an approach that relies on a standard reciprocity-based expression is developed for finding the mutual admittance between CPW-fed twin slots on an infinite conductor-backed two-layer substrate. Section 5.3 contains an original derivation of the spatial-domain Green's function for two-layer parallel-plate substrates that is required for implementing the internal mutual admittance formulation that forms part of Section 5.2. Section 5.4 presents and discusses results for broadside CPW-fed twin slots and non-identical slot pairs on a variety of two-layer parallel-plate substrates. These results are compared to moment-method-based simulations using IE3D [60] and a measurement. Conclusions are stated in Section 5.5.

² As an alternative to the above full-wave analysis, the authors [10] introduce a new analysis for CPW-fed slots on semi-infinite substrates that reduces the number of unknowns but has the same accuracy as a finely-meshed MoM; the analysis relies on the representation of equivalent magnetic currents in terms of entire-domain basis functions defined in terms of analytical Green's functions of canonical geometries such as an infinite slotline.

³ This number takes into account that $Y_{mn} = Y_{nm}$ due to reciprocity.



5.2 FORMULATION OF RECIPROCITY-EXPRESSION APPROACH FOR MUTUAL ADMITTANCE BETWEEN CPW-FED SLOTS ON CONDUCTOR-BACKED TWO-LAYER SUBSTRATE

5.2.1 Mutual admittance between centre-fed slots radiating into half-space

Consider two narrow rectangular slots labeled 1 and 2 in an infinite, perfectly conducting ground plane at $z = 0$ that radiate into the half-space $z > 0$, as shown in Fig. 5.2(a). The slots are assumed to be center-fed via two-wire lines by lumped voltage sources. The slots are backed by an arbitrary substrate (for example, the substrate could be an air half-space, as in the case of center-fed narrow slots in an infinite ground plane which is the dual of slender electric dipoles in free space, or a layered substrate such as the conductor-backed two-layer substrate of Fig. 5.1). The tangential electric field components in the slots are denoted $\mathbf{E}_{1,slot}$ and $\mathbf{E}_{2,slot}$.

An equivalent problem that pertains to the region $z > 0$ may be set up as follows. Using the surface equivalence theorem [52], the slots may be replaced by two equivalent magnetic surface current densities $\mathbf{M}_{1,eq} = \mathbf{E}_{1,slot} \times \hat{z}$ and $\mathbf{M}_{2,eq} = \mathbf{E}_{2,slot} \times \hat{z}$ on an infinite ground plane radiating into the half-space $z > 0$, as shown in Fig. 5.2(b). These equivalent currents ensure that the electromagnetic fields in the half-space $z > 0$ remain unchanged from their values in the situation of Fig. 5.2(a). (Details of applying the surface equivalence theorem are presented in Section 5.2.2.1.)

Based on a standard formulation [66], the mutual admittance between slots 1 and 2 of Fig. 5.2 due to coupling in the half-space $z > 0$ can be expressed as

$$Y_{12} = -\frac{1}{V_1 V_2'} \int_{S_2} \mathbf{H}_{21} \cdot \mathbf{M}'_2 dS_2 \quad (5.1)$$

with

\mathbf{H}_{21} the magnetic field of magnetic current \mathbf{M}_1 at the position of slot 2 when slot 1 is excited and radiates in *isolation* (\mathbf{M}_1 is the equivalent magnetic current representing slot 1 when slot 1 is excited and radiates in *isolation*)

\mathbf{M}'_2 the equivalent magnetic current representing slot 2 when slot 2 is excited and radiates in the presence of a short-circuited slot 1

V_1 the terminal voltage of slot 1, or the total magnetic current through the terminals of slot 1, when slot 1 is excited and radiates in *isolation*

V_2' the terminal voltage of slot 2, or the total magnetic current through the terminals of slot 2, when slot 2 is excited and radiates in the presence of a short-circuited slot 1

S_2 the surface area of slot 2

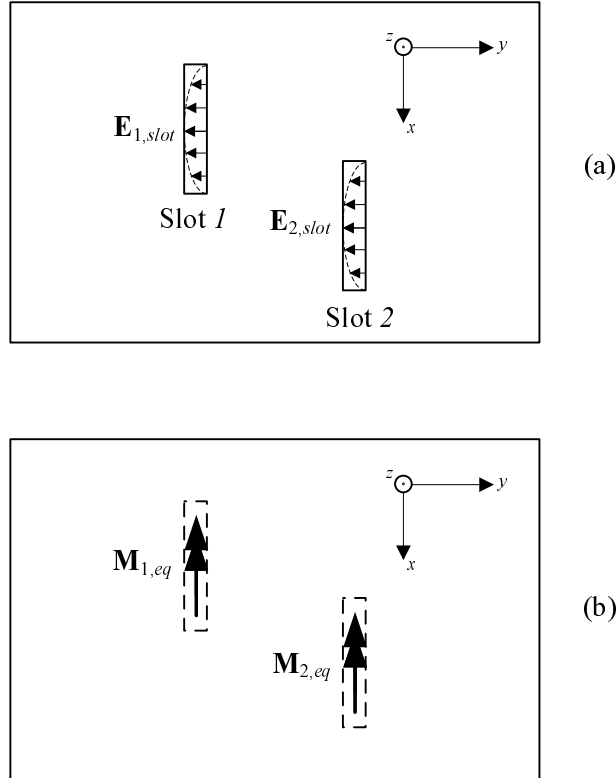


FIGURE 5.2: (a) Two narrow center-fed slots on a perfectly conducting ground plane radiating into the half-space $z > 0$. (b) The equivalent problem: two magnetic currents on a perfectly conducting ground plane. The dashed lines indicate the positions of the slots represented by the magnetic currents.

Crucial to the derivation of Eq. (5.1) is that the slots are center-fed by infinitesimal sources, which permits the introduction of terminal voltages and currents (hence the appearance of V_1 and V_2 in the equation). Noting that computation of \mathbf{H}'_{21} requires use of the vector potential \mathbf{F} for a magnetic current density radiating into a half-space on an infinite perfect electric conductor (PEC), Eq. (5.1) is consistent with [67, Eq. (14)].

If it can be assumed that the shape of the electric field in slot 2 when radiating in isolation is not significantly different when slot 2 radiates in the presence of a short-circuited slot 1, Eq. (5.1) can be expressed in a form that is more readily implemented:

$$Y_{12} = -\frac{1}{V_1 V_2} \int_{S_2} \mathbf{H}_{21} \cdot \mathbf{M}_2 dS_2 \quad (5.2)$$

with

\mathbf{H}_{21} the magnetic field of magnetic current \mathbf{M}_1 at the position of slot 2 when slot 1 is excited and radiates in *isolation* (\mathbf{M}_1 is the equivalent magnetic current representing slot



I when slot I is excited and radiates in *isolation*)

M_2 the equivalent magnetic current representing slot 2 when slot 2 is excited and radiates in *isolation*

V_1 the terminal voltage of slot I , or the total magnetic current through the terminals of slot I , when slot I is excited and radiates in *isolation*

V_2 the terminal voltage of slot 2, or the total magnetic current through the terminals of slot 2, when slot 2 is excited and radiates in *isolation*

S_2 the surface area of slot 2

5.2.2 Mutual admittance between CPW-fed slots on conductor-backed two-layer substrate

Consider now two CPW-fed slots on a two-layer parallel-plate substrate that radiate into the half-space $z < 0$, as shown in Fig. 5.1.⁴ Each slot can be conceived of as center-fed by a voltage (or current) source in the sense of Fig. 5.3. In other words, the CPW feed line can be thought of as originating from a short section of slotline which is excited at its centre by a lumped voltage source; the section of slotline is then extended via 90° angles to form the CPW. This excitation technique is consistent with the excitation of CPW and/or CPW-fed slots in moment-method-based analyses [68]. Since the overall composite slot is center-fed, the implication is that Eq. (5.1) can be used to find the mutual admittance between CPW-fed slots as well. The more complex shape of these slots (compared to center-fed rectangular slots) does not affect the form of that equation. For the relatively narrow CPW-fed slots on a two-layer parallel-plate substrate considered in this thesis, the shape of the electric field in slot 2 when radiating in isolation is not significantly different from the field when slot 2 radiates in the presence of a short-circuited slot I ; this was confirmed using IE3D. Hence Eq. (5.2) can be used instead of Eq. (5.1).

In Sections 5.2.2.1 and 5.2.2.2 below, equivalent problems are formulated for the external and internal mutual admittance between CPW-fed slots on a two-layer parallel-plate substrate. For each equivalent problem, Eq. (5.2) can be used in conjunction with the appropriate Green's function to find the relevant contribution to the total mutual admittance, *i.e.*, external or internal. In both the external and internal cases, the following assumptions and conventions are adopted.

First, in order to simplify the integration in Eq. (5.2), the effects of mutual coupling between the respective CPW feed lines (including the originating slotline sections), and between CPW feed lines and radiating slots are assumed to be negligible. Mutual coupling between the originating slotline

⁴ Denoting the air half-space by $z < 0$, as opposed to the above $z > 0$, is done for mathematical convenience and makes no difference to the argument that follows.

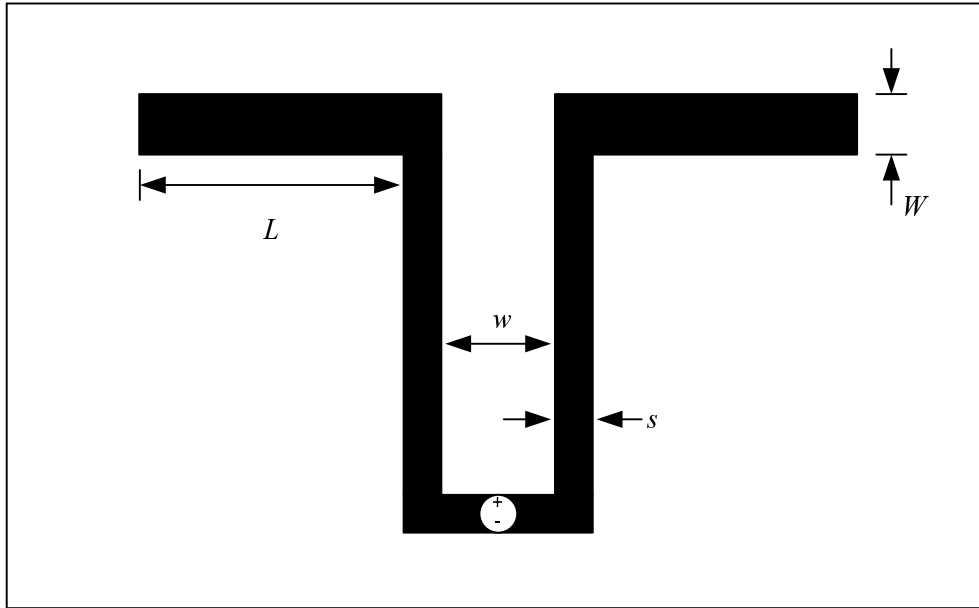


FIGURE 5.3: Top view of CPW-fed slot on conductor-backed two-layer substrate. The slot can be thought of as center-fed by a localized infinitesimal voltage source. $L \equiv$ half-length and $W \equiv$ width of radiating slot; $s \equiv$ slot width and $w \equiv$ centre strip width of CPW feed line.

sections (*cf.* Fig. 5.3) and radiating slots is also considered negligible (this assumption follows if the CPW feeds are sufficiently long). Hence for the purposes of evaluating the above reaction integral, only the radiating portions of CPW-fed slots 1 and 2 are taken into account, as illustrated in Fig. 5.4.

Second, the mutual admittance Y_{12} is referred to positions on the CPW feed lines that are some distance l_f away from radiating slot centres. Fig. 5.5 shows these reference planes, labelled $11'$ and $22'$; the terminal voltages V_1 and V_2 of Eq. (5.2) would need to be determined at these planes for each slot radiating in isolation. The tangential electric field in a CPW-fed slot (including the feed line) can be determined using the moment method [14, 15]; Figs. 4.9 and 4.10 show radiating slot fields obtained using IE3D. When for instance slot 1 is analyzed (in isolation) in IE3D, the excitation port can be user-defined to coincide with reference plane $11'$.⁵ IE3D finds the port voltage – which is the same as the terminal voltage V_1 – in addition to the slot tangential electric field. It was verified that the port voltage is the integral of the electric field in one of the two CPW slots over the width of the slot. For example, if a moment-method discretization allowing for only one cell across the slot width is assumed, $V_1 = wE_{1x}^{CPW}$ at terminal plane $11'$, with w the slot width and $E_{1x}^{CPW}\hat{x}$ the electric field in the centre of the slot.⁶ The implementation of terminal voltages will be discussed further in Section 5.4.1.

⁵ It is assumed that the results of the manner in which IE3D excites the slot and the manner suggested in Fig. 5.3 will be the same at the reference planes and beyond (*i.e.*, towards the radiating slot).

⁶ A discretization using edge cells in IE3D resulted in only a marginal difference in the port voltage.

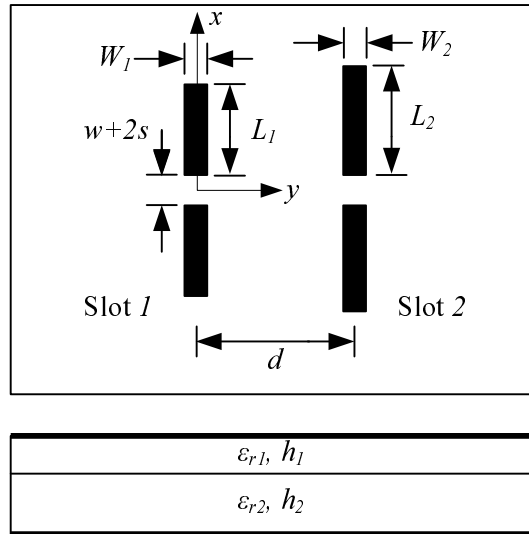


FIGURE 5.4: Top and side views of broadside slots on conductor-backed two-layer substrate. The CPW feed lines have been removed. $L_1, L_2 \equiv$ half-lengths and $W_1, W_2 \equiv$ widths of radiating slots; $d \equiv$ distance between radiating slots; $h_1, h_2 \equiv$ dielectric layer heights; $\epsilon_{r1}, \epsilon_{r2} \equiv$ relative dielectric constants. The ground plane containing the slots coincides with the plane $z = 0$; the z axis points into the page.

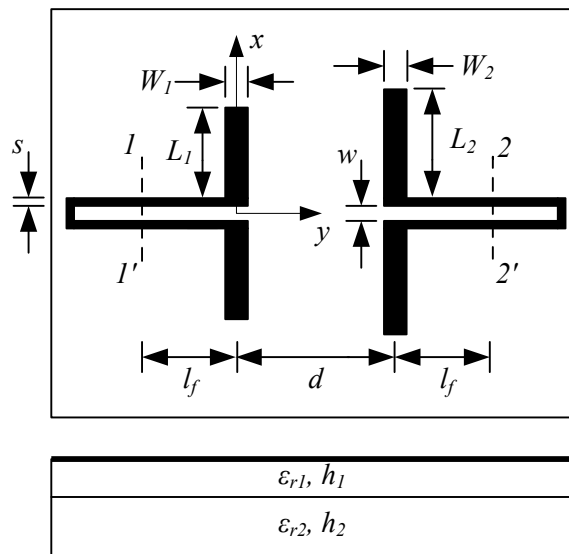


FIGURE 5.5: Broadside CPW-fed slot antennas on conductor-backed two-layer substrate with terminal reference planes $11'$ and $22'$. Each slot can be thought of as being excited in the manner shown in Fig. 5.3.

5.2.2.1 External mutual admittance formulation

In this section, it is showed how Eq. (5.2) may be applied to find the external mutual admittance between two CPW-fed slots on an infinite two-layer parallel-plate substrate. This involves setting

up equivalent problems for finding the quantities \mathbf{H}_{21} and \mathbf{M}_2 that appear in the integral. Here, the quantities will be referred to as \mathbf{H}_{21}^{ext} and \mathbf{M}_2^{ext} in order to distinguish them from the internal problem. Hence,

$$Y_{12}^{ext} = -\frac{1}{V_1 V_2} \int_{S_2} \mathbf{H}_{21}^{ext} \cdot \mathbf{M}_2^{ext} dS_2 \quad (5.3)$$

With respect to the equivalent problem required to find \mathbf{H}_{21}^{ext} , consider Fig. 5.6(a), which is based on a side view of the two-layer parallel-plate substrate containing radiating slots only (*cf.* Fig. 5.4). Slot 2 has been removed, *i.e.*, replaced by conductor, in order to adhere to the definition of \mathbf{H}_{21}^{ext} in Eq. (5.2) as the magnetic field due to slot 1 at the position of slot 2 when slot 1 radiates in isolation. The ground plane containing slot 1 is situated at $z = 0$. The half-space external to the slots is denoted by $z < 0$; hence the unit surface normal vector \hat{n} points in the negative z direction. The tangential components of the electric field in the aperture of slot 1 are assumed to be known and given by $\mathbf{E}_{1,slot}$.

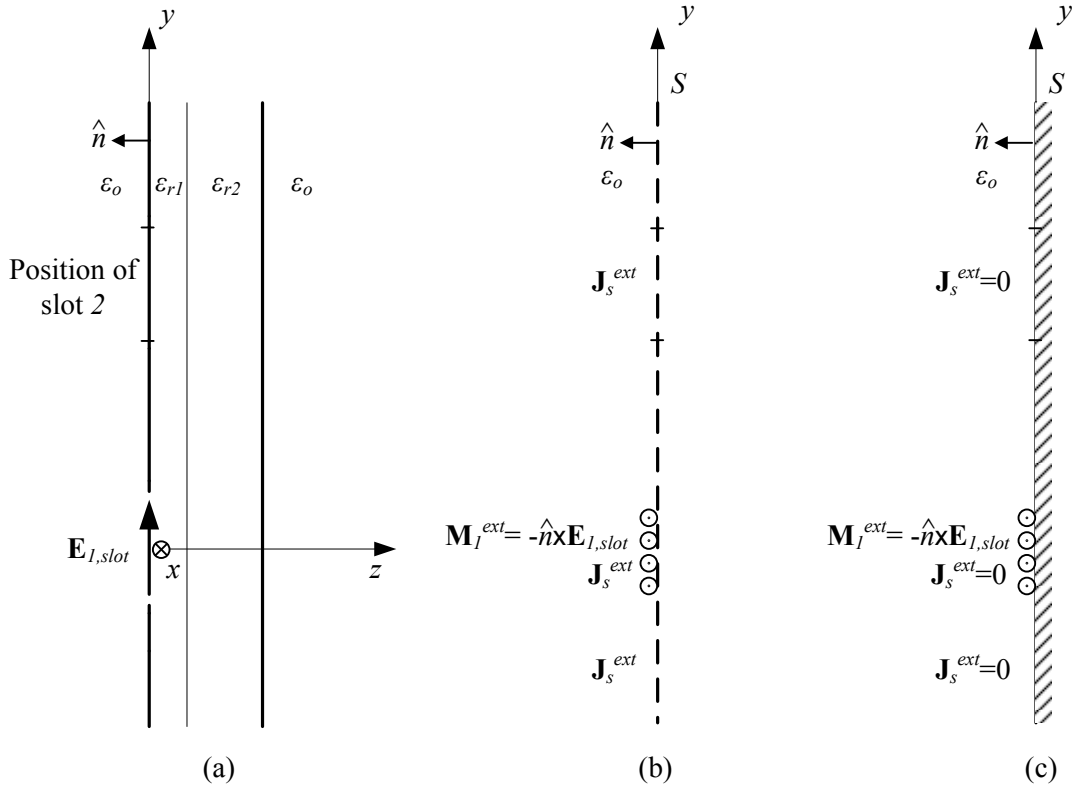


FIGURE 5.6: Steps in setting up an external equivalent model for one slot on a two-layer parallel-plate substrate. In (a)–(c), electromagnetic fields are the same in the region $z < 0$.

Fig. 5.6(b) and (c) demonstrate application of the surface equivalence theorem [69] to the slot of Fig. 5.6(a). In Fig. 5.6(b), an imaginary closed surface S , which is a plane of infinite extent, replaces the conducting plane containing the slot. Equivalent magnetic and electric surface current densities \mathbf{M}_1^{ext} and \mathbf{J}_s^{ext} are formed on this surface to ensure that the electromagnetic fields in the half-space



$z < 0$ remain unchanged from their values in the situation of Fig. 5.6(a). \mathbf{M}_1^{ext} is non-zero only over the position of slot 1, while \mathbf{J}_s^{ext} is non-zero everywhere. If it is assumed that $\mathbf{E}_{1,slot} = E_{1y,slot}\hat{y}$, and since $\hat{n} = -\hat{z}$ for the external problem,

$$\mathbf{M}_1^{ext} = -\hat{n} \times E_{1y,slot}\hat{y} = -E_{1y,slot}\hat{x} = M_{1x}^{ext}\hat{x} \quad (5.4)$$

(The above assumption regarding aperture electric field components will be adhered to throughout. An investigation using IE3D of the centre fields along the lengths of representative CPW-fed slots revealed that the \hat{x} component is in fact negligible.) In 5.6(c), a perfectly conducting plane approaches S from the right, shorting out \mathbf{J}_s^{ext} everywhere but leaving \mathbf{M}_1^{ext} intact.

In a half-space consisting of air over a PEC, the magnetic field \mathbf{H} due to a general magnetic current density \mathbf{M} can be calculated from

$$\mathbf{H} = -j\omega\mathbf{F} - j\frac{1}{\omega\mu_0\varepsilon_0}\nabla(\nabla \cdot \mathbf{F}) \quad (5.5a)$$

where the vector potential \mathbf{F} is given as

$$\mathbf{F}(x, y, z) = \frac{\varepsilon_0}{2\pi} \int_V \mathbf{M}(x', y', z') \frac{e^{-jk_0R}}{R} dV' \quad (5.5b)$$

In the above, $R = \sqrt{(x-x')^2 + (y-y')^2 + (z-z')^2}$, and $k_0 = \omega\sqrt{\mu_0\varepsilon_0}$ is the free-space wave-number. Eqs. (5.5a) and (5.5b) correspond to [69, eqs. (6-109), (6-111)] except for the factor $\frac{1}{2\pi}$ in Eq. (5.5b) which reflects the fact that the magnetic current radiates in a half-space bordered by an infinite ground plane instead of free-space (*cf.* [70]).

The equivalent problem for \mathbf{M}_2^{ext} , which entails that slot 2 radiates in isolation, is derived in the same manner as that for slot 1. The result is identical to that presented in Fig. 5.6(c) except that the equivalent magnetic surface current density is \mathbf{M}_2^{ext} at the position of slot 2. Assuming that $\mathbf{E}_{2,slot} = E_{2y,slot}\hat{y}$,

$$\mathbf{M}_2^{ext} = -E_{2y,slot}\hat{x} = M_{2x}^{ext}\hat{x} \quad (5.6)$$

Based on Eq. (5.6), Eq. (5.3) reduces to (*cf.* Fig. 5.4)



$$\begin{aligned}
 Y_{12}^{ext} &= -\frac{1}{V_1 V_2} \int_{S_2} H_{21x}^{ext} M_{2x}^{ext} dS_2 \\
 &= -\frac{1}{V_1 V_2} \left\{ \int_{x=-\left(\frac{w}{2}+s+L_2\right)}^{-\left(\frac{w}{2}+s\right)} \int_{y=d-\frac{W_2}{2}}^{d+\frac{W_2}{2}} H_{21x}^{ext} M_{2x}^{ext} dx dy \right. \\
 &\quad \left. + \int_{x=\frac{w}{2}+s}^{\frac{w}{2}+s+L_2} \int_{y=d-\frac{W_2}{2}}^{d+\frac{W_2}{2}} H_{21x}^{ext} M_{2x}^{ext} dx dy \right\} \quad (5.7)
 \end{aligned}$$

By combining Eqs. (5.4), (5.5b) and (5.5a) and considering rectangular vector components separately, H_{21x}^{ext} can be expressed as (cf. [69, Eqs. (6-111a), (6-108d), (6-108e)])

$$H_{21x}^{ext}(x, y, z) = -\frac{j}{2\pi k_0 \eta_0} \int_{S_1} [G_1 M_{1x}^{ext}(x', y') + (x - x')^2 G_2 M_{1x}^{ext}(x', y')] e^{-jk_0 R} dx' dy' \quad (5.8a)$$

with

$$G_1 = \frac{-1 - jk_0 R + k_0^2 R^2}{R^3} \quad (5.8b)$$

$$G_2 = \frac{3 + j3k_0 R - k_0^2 R^2}{R^5} \quad (5.8c)$$

In the above, $\eta_0 = \sqrt{\frac{\mu_0}{\epsilon_0}}$ is the intrinsic impedance of free space, and $R = \sqrt{(x - x')^2 + (y - y')^2}$ (i.e., in the plane of slot 2).

5.2.2.2 Internal mutual admittance formulation

Eq. (5.2) may be used in a similar manner to find the internal mutual admittance Y_{12}^{int} between two CPW-fed slots on an infinite two-layer parallel-plate substrate. In particular,

$$Y_{12}^{int} = -\frac{1}{V_1 V_2} \int_{S_2} \mathbf{H}_{21}^{int} \cdot \mathbf{M}_2^{int} dS_2 \quad (5.9)$$

(Eq. (5.2) holds even though the slots are now considered to be radiating into the substrate, as the validity of the Lorentz reciprocity theorem, from which Eq. (5.2) is derived, extends to isotropic media that may be inhomogeneous [69].)

An equivalent problem for finding \mathbf{H}_{21}^{int} , which involves slot 1 radiating in isolation, is set up as follows. Fig. 5.7(a) shows a side view of the two-layer parallel-plate substrate containing radiating slots only with slot 2 removed. The unit surface normal vector \hat{n} now points into the substrate. As before, the tangential electric field in slot 1 is $\mathbf{E}_{1,slot}$.

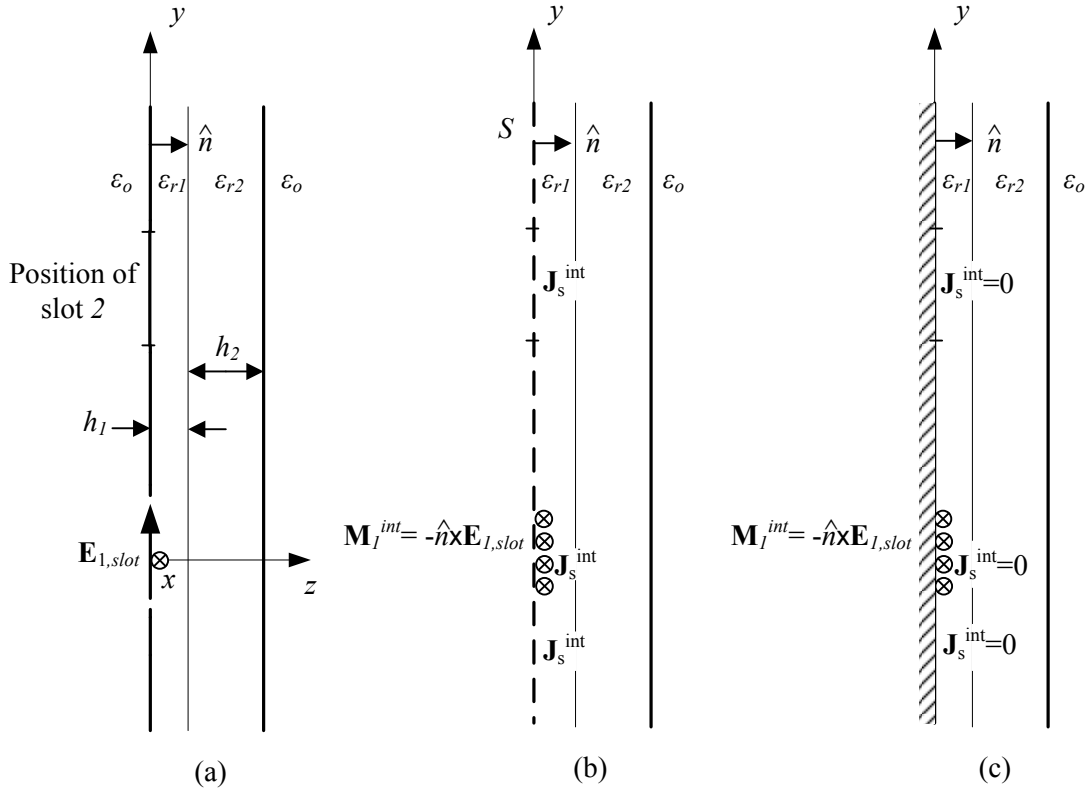


FIGURE 5.7: Steps in setting up an internal equivalent model for one slot on a two-layer parallel-plate substrate. In (a)–(c), electromagnetic fields are the same in the region $0 < z < h_1 + h_2$.

Application of the surface equivalence theorem yields equivalent currents in the place of slot 1 such that the fields inside the substrate, *i.e.*, for $0 < z < h_1 + h_2$, remain unchanged from their values in Fig. 5.7(a). Fig. 5.7(b) shows an imaginary closed surface S , which is an infinite plane, replacing the conducting plane containing the slot. Equivalent magnetic and electric current densities \mathbf{M}_1^{int} and \mathbf{J}_s^{int} are formed on this surface on the side facing the substrate. \mathbf{M}_1^{int} is non-zero only over the positions of slot 1, while \mathbf{J}_s^{int} is non-zero everywhere. If $\mathbf{E}_{1,slot} = E_{1y,slot} \hat{y}$, and since $\hat{n} = \hat{z}$,

$$\mathbf{M}_1^{int} = -\hat{n} \times E_{1y,slot} \hat{y} = E_{1y,slot} \hat{x} = M_{1x}^{int} \hat{x} \quad (5.10)$$

It is then assumed that an imaginary conducting plane approaches S from the left, shorting out \mathbf{J}_s^{int} everywhere but leaving \mathbf{M}_1^{int} intact, as shown in Fig. 5.7(c).

The equivalent problem for \mathbf{M}_2^{int} is derived in the same manner as for slot 1. The result only differs from that presented in Fig. 5.7(c) in that the equivalent magnetic current density is \mathbf{M}_2^{int} at the position of slot 2. Assuming that $\mathbf{E}_{2,slot} = E_{2y,slot} \hat{y}$,

$$\mathbf{M}_2^{int} = E_{2y,slot} \hat{x} = M_{2x}^{int} \hat{x} \quad (5.11)$$



Substituting Eq. (5.11) into Eq. (5.9) yields

$$\begin{aligned}
 Y_{12}^{int} &= -\frac{1}{V_1 V_2} \int_{S_2} H_{21x}^{int} M_{2x}^{int} dS_2 \\
 &= -\frac{1}{V_1 V_2} \left\{ \int_{x=-\left(\frac{w}{2}+s+L_2\right)}^{-\left(\frac{w}{2}+s\right)} \int_{y=d-\frac{W_2}{2}}^{d+\frac{W_2}{2}} H_{21x}^{int} M_{2x}^{int} dx dy \right. \\
 &\quad \left. + \int_{x=\frac{w}{2}+s}^{\frac{w}{2}+s+L_2} \int_{y=d-\frac{W_2}{2}}^{d+\frac{W_2}{2}} H_{21x}^{int} M_{2x}^{int} dx dy \right\} \quad (5.12)
 \end{aligned}$$

H_{21x}^{int} can be found from

$$H_{21x}^{int}(\mathbf{r}) = \int_{S_1} G_{xx}^{HM}(\mathbf{r}, \mathbf{r}') M_{1x}^{int}(\mathbf{r}') dS_1' \quad (5.13a)$$

which in the plane of the slots becomes

$$\begin{aligned}
 H_{21x}^{int}(x, y, 0) &= \int_{S_1} G_{xx}^{HM}(x, y, 0; x', y', 0) M_{1x}^{int}(x', y') dx' dy' \\
 &= \int_{x'=-\left(\frac{w}{2}+s+L_1\right)}^{-\left(\frac{w}{2}+s\right)} \int_{y'=-\frac{W_1}{2}}^{\frac{W_1}{2}} G_{xx}^{HM}(x, y, 0; x', y', 0) M_{1x}^{int}(x', y') dx' dy' \\
 &\quad + \int_{x'=\frac{w}{2}+s}^{\frac{w}{2}+s+L_1} \int_{y'=-\frac{W_1}{2}}^{\frac{W_1}{2}} G_{xx}^{HM}(x, y, 0; x', y', 0) M_{1x}^{int}(x', y') dx' dy' \quad (5.13b)
 \end{aligned}$$

In the above, $G_{xx}^{HM}(x, y, 0; x', y', 0)$ is the \hat{x} component of the spatial-domain magnetic field due to an \hat{x} -directed horizontal magnetic dipole (HMD) at $(x', y', 0)$ on the ground plane adjacent to the higher-permittivity dielectric layer inside a two-layer parallel-plate substrate (primed and unprimed coordinates correspond to source and observation coordinates respectively). Section 5.3 is devoted to the derivation of G_{xx}^{HM} .

5.3 SPATIAL-DOMAIN GREEN'S FUNCTION FOR CONDUCTOR-BACKED TWO-LAYER SUBSTRATE

In this chapter, a spatial-domain expression is derived for the magnetic field H_x due to an \hat{x} -directed horizontal magnetic dipole (HMD) placed against the top plate inside a two-layer parallel-plate substrate (by “top plate” is meant the conducting plane that borders the higher-permittivity layer, *i.e.*, layer I). The position of the HMD coincides with the origin of the coordinate axes. Fig. 5.8 shows

the substrate and the placement of the HMD (*cf.* Fig. 5.1). It is only necessary to account for H_x at points in the plane of the magnetic dipole (*i.e.*, $z = 0$), since Eq. (5.12) requires the \hat{x} -component of the magnetic field due to slot 1 at the position of slot 2, with both slots situated in the plane $z = 0$; hence the objective is to find $H_x(x, y, 0)$.

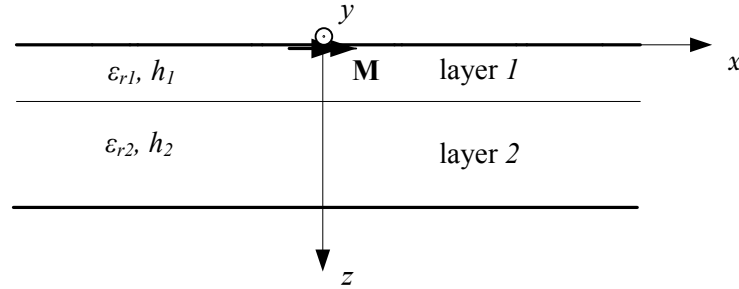


FIGURE 5.8: \hat{x} -directed horizontal magnetic dipole (HMD) inside a two-layer parallel-plate substrate. ϵ_{r1} and ϵ_{r2} are relative dielectric constants; $\mu = \mu_0$ in all layers.

The process of determining H_x is divided into two stages. First, the spectral-domain equivalent of H_x is found in closed form from general spectral-domain field expressions for multilayered media derived by Bhattacharya [71].⁷ Second, the spatial domain field H_x is obtained from its spectral domain equivalent by means of an inverse Fourier transform (*e.g.*, [71]), resulting in expressions containing Sommerfeld integrals that need to be evaluated numerically. To the author's knowledge, the spatial domain expressions for a two-layer parallel-plate substrate excited by a HMD that result from applying this procedure, and details of the treatment of the singularities in the integrals, are not currently available in the literature.^{8,9}

For the sake of completeness, Bhattacharya's method for finding the fields in a planar multilayered medium consisting of an arbitrary number of layers excited by planar electric and/or magnetic current distributions is now briefly outlined (full details can be found in [71, Chapters 1 and 2]). The geometry of such a medium is shown in Fig. 5.9. Its non-homogeneity pertains to its permittivity which can be expressed as $\epsilon = \epsilon(z)$, where z is the direction perpendicular to the interfaces between layers. The non-homogeneity is stepwise in nature, *i.e.*, within layer i of height h_i , $\epsilon(z) = \epsilon_0 \epsilon_{ri}$, which is a constant (ϵ_{ri} is the relative permittivity in layer i , and ϵ_0 is the permittivity of free space). For the purposes of the present work, it can be assumed without a loss of generality

⁷ A comprehensive review of techniques for finding Green's functions in planar layered media can be found in [72].

⁸ The spectral-domain Green's function for the two-layer parallel-plate substrate presented in [73] appears to be incorrect.

⁹ The spatial-domain Green's function for a single-layer parallel-plate substrate can be determined either in integral form or as a double infinite series [74]. Another instance of the latter form is the Green's function for an infinite periodic two-layer parallel-plate waveguide that can be determined in infinite-series form employing hybrid modes [75].

that the permeability $\mu = \mu_0$ everywhere.

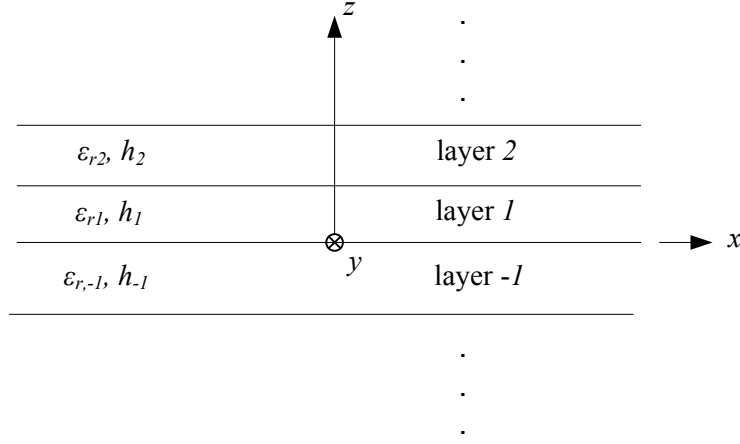


FIGURE 5.9: Geometry of a planar multilayered structure consisting of an arbitrary number of layers. $\mu = \mu_0$ in all layers.

In the above medium, the electromagnetic field outside of the source region can be decomposed into transverse magnetic (TM) and transverse electric (TE) components with respect to a reference direction perpendicular to the layer interfaces, *i.e.*, the \hat{z} -direction in Fig. 5.9. The total field can be expressed as the sum of TM_z and TE_z modes;¹⁰ the subscript z will be suppressed in what follows. For TM mode fields, once the longitudinal component of the electric flux density vector, D_z^{TM} is known, the remaining field components D_x^{TM} , D_y^{TM} , B_x^{TM} , and B_y^{TM} can be found ($B_z^{TM} = 0$). Similarly for TE mode fields, if the longitudinal component of the magnetic flux density vector, B_z^{TE} is known, B_x^{TE} , B_y^{TE} , D_x^{TE} , and D_y^{TE} can be determined.

Bhattacharyya [71] derives spatial-domain non-linear, non-homogeneous differential equations for each of D_z^{TM} and B_z^{TE} that are valid everywhere in the substrate. Two-dimensional Fourier transforms of $D_z^{TM}(x, y, z)$ and $B_z^{TE}(x, y, z)$ with respect to their transverse coordinates x and y yield their spectral-domain equivalents, $\tilde{D}_z^{TM}(k_x, k_y, z)$ and $\tilde{B}_z^{TE}(k_x, k_y, z)$, with the two-dimensional Fourier transform of a function $f(x, y)$ defined as

$$\tilde{f}(k_x, k_y) = \mathcal{F}\{f(x, y)\} = \frac{1}{4\pi^2} \int_{-\infty}^{\infty} \int_{-\infty}^{\infty} f(x, y) e^{jk_x x} e^{jk_y y} dx dy \quad (5.14a)$$

and the inverse transform as

$$f(x, y) = \mathcal{F}^{-1}\{\tilde{f}(k_x, k_y)\} = \int_{-\infty}^{\infty} \int_{-\infty}^{\infty} \tilde{f}(k_x, k_y) e^{-jk_x x} e^{-jk_y y} dk_x dk_y \quad (5.14b)$$

¹⁰ For some combinations of multilayered media and sources, the independent existence of either TM_z or TE_z waves is possible; this however does not apply to the present problem.



Replacing D_z^{TM} and B_z^{TE} with their inverse transforms in the above differential equations and taking the forward transforms yield differential equations for $\tilde{D}_z^{TM}(z)$ and $\tilde{B}_z^{TE}(z)$. Each differential equation can be combined with the Fourier transform of the appropriate Maxwell's divergence equation to yield a pair of transmission line equations in the spatial variable z , one pair containing $\tilde{D}_z^{TM}(z)$ and the other pair containing $\tilde{B}_z^{TE}(z)$. Within each pair, $\tilde{D}_z^{TM}(z)$ and $\tilde{B}_z^{TE}(z)$ are equivalent to the voltage $V(z)$ along the line, for which Bhattacharyya [71] presents closed-form solutions for planar electric and magnetic sources respectively.

These general solutions in the spectral domain, valid for an arbitrary number of dielectric layers excited by planar electric or magnetic sources, are used in the present work as a point of departure for deriving spatial-domain solutions H_x^{TM} and H_x^{TE} in the two-layer parallel-plate substrate of Fig. 5.8 due to a \hat{x} -directed HMD at the origin (see Sections 5.3.1 and 5.3.2), from which H_x can then be found in the plane of the slots (*i.e.*, $z = 0$) as

$$H_x(x, y, 0) = H_x^{TM}(x, y, 0) + H_x^{TE}(x, y, 0) \quad (5.15)$$

In what follows, the parallel plates of the two-layer parallel-plate substrate are assumed to be perfect electric conductors (PECs), and the dielectrics are assumed to be lossless.

5.3.1 H_x^{TM} for \hat{x} -directed HMD against top conducting plate inside two-layer parallel-plate substrate

Consider the two-layer parallel-plate structure of Fig. 5.8. The substrate is excited by a HMD at the origin which can be expressed as a volume current density,

$$\mathbf{M} = \delta(x)\delta(y)\delta(z)\hat{x} \quad (5.16a)$$

or equivalently a surface current density in the plane $z = 0$,

$$\mathbf{M}_s = M_{sx}\hat{x} = \delta(x)\delta(y)\hat{x} \quad (5.16b)$$

The preceding equations are related by $\mathbf{M} = \mathbf{M}_s\delta(z)$.

The objective is to find \tilde{D}_z^{TM} from which all remaining TM field components, including H_x^{TM} , can be determined [71, p. 5] (for the sake of succinctness, the superscript TM is omitted for the remainder of the section). D_z and \tilde{D}_z are a Fourier transform pair related according to Eq. (5.14),

$$\tilde{D}_z(k_x, k_y, z) = \frac{1}{4\pi^2} \int_{-\infty}^{\infty} \int_{-\infty}^{\infty} D_z(x, y, z) e^{jk_x x} e^{jk_y y} dx dy \quad (5.17a)$$

$$D_z(x, y, z) = \int_{-\infty}^{\infty} \int_{-\infty}^{\infty} \tilde{D}_z(k_x, k_y, z) e^{-jk_x x} e^{-jk_y y} dk_x dk_y \quad (5.17b)$$

In layer i , H_x can be expressed directly in terms of \tilde{D}_z [71, p. 23] as follows:

$$H_x(x, y, z) = \omega \int_{-\infty}^{\infty} \int_{-\infty}^{\infty} \frac{k_y \tilde{D}_z(k_x, k_y, z)}{k_i^2 - k_{iz}^2} e^{-jk_x x} e^{-jk_y y} dk_x dk_y \quad (5.18)$$

In the above inverse Fourier transform, $k_{iz} = \sqrt{k_i^2 - k_x^2 - k_y^2}$ where $k_i = \omega \sqrt{\mu_i \epsilon_i} = \omega \sqrt{\mu_0 \epsilon_0 \epsilon_{ri}}$ is the wave number for dielectric layer i , and $i = 1$ or 2 .

For a two-layer parallel-plate substrate, the general multilayer TM mode spectral domain equivalent transmission line circuit ([71], Fig. 2.3) reduces to the circuit shown in Fig. 5.10, where the transmission line voltage $V(z)$ equals $\tilde{D}_z(k_x, k_y, z)$ of Eq. (5.18). The sections of transmission line with characteristic admittances y_{01}^m and y_{02}^m correspond to substrate layers 1 and 2 respectively. The parallel plates of the substrate (cf. Fig. 5.8), which are PECs, are represented by open circuits in the equivalent circuit. This is required since the component of an electric field perpendicular to a PEC (D_z in this case) is a maximum on the PEC.

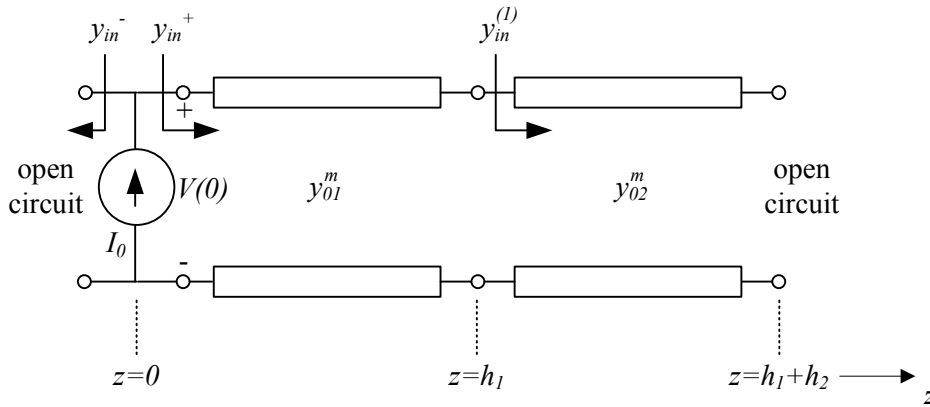


FIGURE 5.10: TM mode spectral domain equivalent circuit for two-layer parallel-plate substrate with planar magnetic current excitation at $z = 0$.

As only points in the plane $z = 0$ plane need to be considered, Eq. (5.18) reduces to

$$\begin{aligned} H_x(x, y, 0) &= \omega \int_{-\infty}^{\infty} \int_{-\infty}^{\infty} \frac{k_y \tilde{D}_z(k_x, k_y, 0)}{k_i^2 - k_{iz}^2} e^{-jk_x x} e^{-jk_y y} dk_x dk_y \\ &= \omega \int_{-\infty}^{\infty} \int_{-\infty}^{\infty} \frac{k_y V(0)}{k_i^2 - k_{iz}^2} e^{-jk_x x} e^{-jk_y y} dk_x dk_y \end{aligned} \quad (5.19)$$



In Eq. (5.19), $V(0)$ can be determined from [71, Eqs. (2.25) and (2.43)]; that is,

$$V(0) = \frac{I_0}{y_{in}^m} \quad (5.20)$$

In the preceding equation, I_0 is the value of the current source in the equivalent circuit, and $y_{in}^m = y_{in}^+ + y_{in}^-$ is the total input admittance at the source, with y_{in}^+ and y_{in}^- the input admittances seen when looking from the source into the transmission line in the $+z$ and $-z$ directions. I_0 in Eq. (5.20) can be found from [71, Table 2.1] as

$$I_0 = j(\mathbf{k}_\rho \times \tilde{\mathbf{M}}_s) \cdot \hat{z} \quad (5.21a)$$

In Eq. (5.21a), $\mathbf{k}_\rho = k_\rho \hat{\rho} = k_x \hat{x} + k_y \hat{y}$, and the Fourier transform of Eq. (5.16b) yields

$$\tilde{M}_{sx} = \frac{1}{4\pi^2} \quad (5.21b)$$

Hence

$$I_0 = -j \frac{k_y}{4\pi^2} \quad (5.21c)$$

y_{in}^m in Eq. (5.20) can be found by noting that $y_{in}^- = 0$, and calculating y_{in}^+ using standard transmission line theory. In particular,

$$y_{in}^+ = y_{01}^m \frac{y_{in}^{(1)} + jy_{01}^m \tan k_{1z} h_1}{y_{01}^m + jy_{in}^{(1)} \tan k_{1z} h_1} \quad (5.22a)$$

with

$$y_{in}^{(1)} = jy_{02}^m \tan k_{2z} h_2 \quad (5.22b)$$

In the preceding two equations, $y_{0i}^m = jk_{iz}/\varepsilon_i$ is the (TM) characteristic admittance of transmission line i [71, Table 2.1] and $k_{iz} = \sqrt{k_i^2 - k_x^2 - k_y^2} = \sqrt{k_i^2 - k_\rho^2}$, where $i = 1$ or 2 . From Eqs. (5.22a)–(5.22b) and $y_{in}^- = 0$ follows

$$y_{in}^m = \frac{k_{1z}}{\varepsilon_1} \frac{D_{TM}}{\varepsilon_2 k_{1z} - \varepsilon_1 k_{2z} \tan k_{1z} h_1 \tan k_{2z} h_2} \quad (5.22c)$$

In Eq. (5.22c), D_{TM} is the TM characteristic equation of the two-layer parallel-plate substrate [56], namely

$$D_{TM} = -\varepsilon_1 k_{2z} \tan k_{2z} h_2 - \varepsilon_2 k_{1z} \tan k_{1z} h_1 \quad (5.22d)$$

Combining Eqs. (5.21), (5.22), (5.20), and (5.19) yields

$$H_x(x, y, 0) = \frac{\omega}{j4\pi^2} \int_{-\infty}^{\infty} \int_{-\infty}^{\infty} \frac{k_y^2}{k_\rho^2} \frac{1}{y_{in}^m(k_x, k_y)} e^{-jk_x x} e^{-jk_y y} dk_x dk_y \quad (5.23)$$



Now make the change of variables

$$x = \rho \cos \phi \quad (5.24a)$$

$$y = \rho \sin \phi \quad (5.24b)$$

$$k_x = k_\rho \cos \alpha \quad (5.24c)$$

$$k_y = k_\rho \sin \alpha \quad (5.24d)$$

in Eq. (5.23) in order to effect a transformation in the spectral domain from rectangular coordinates (k_x, k_y) to cylindrical coordinates (k_ρ, α) . This gives

$$\begin{aligned} H_x(\rho, \phi, 0) &= C \int_{\alpha=0}^{2\pi} \int_{k_\rho=0}^{\infty} \frac{k_\rho^2 \sin^2 \alpha}{k_\rho^2} \frac{1}{y_{in}^m(k_\rho)} e^{-j(k_\rho \cos \alpha \cdot \rho \cos \phi + k_\rho \sin \alpha \cdot \rho \sin \phi)} k_\rho dk_\rho d\alpha \\ &= C \int_0^{\infty} \frac{1}{y_{in}^m(k_\rho)} \int_0^{2\pi} \sin^2 \alpha e^{-jk_\rho \rho \cos(\alpha-\phi)} d\alpha k_\rho dk_\rho \\ &= C \int_0^{\infty} \frac{1}{y_{in}^m(k_\rho)} I_\alpha(k_\rho) k_\rho dk_\rho \end{aligned} \quad (5.25a)$$

with

$$I_\alpha(k_\rho) = \int_{-\phi}^{2\pi-\phi} \sin^2(\alpha + \phi) e^{-jk_\rho \rho \cos \alpha} d\alpha \quad (5.25b)$$

In the above, $C = \frac{\omega}{j4\pi^2}$, $\rho = \sqrt{x^2 + y^2}$, and $k_\rho = \sqrt{k_x^2 + k_y^2}$. Substituting the identity (cf. [56, Eq. (5-101)])

$$e^{-jk_\rho \rho \cos \alpha} = \sum_{n=-\infty}^{\infty} j^{-n} J_n(k_\rho \rho) e^{jn\alpha} \quad (5.26a)$$

into Eq. (5.25b) yields

$$I_\alpha(k_\rho) = \sum_{n=-\infty}^{\infty} j^{-n} J_n(k_\rho \rho) e^{-jn\phi} \int_0^{2\pi} e^{jn\alpha} \sin^2 \alpha d\alpha \quad (5.26b)$$

The integral on the right hand side of Eq. (5.26b) can be solved using a standard identity [76, Eq. 14.523] in conjunction with l'Hospital's rule, giving

$$\int_0^{2\pi} e^{jn\alpha} \sin^2 \alpha d\alpha = \begin{cases} \pi, & n = 0 \\ -\frac{\pi}{2}, & n = -2, 2 \\ 0, & \text{otherwise} \end{cases} \quad (5.26c)$$

Substitution of Eq. (5.26c) into Eq. (5.26b) yields

$$I_\alpha(k_\rho) = \frac{\pi}{2} J_{-2}(k_\rho \rho) e^{j2\phi} + \pi J_0(k_\rho \rho) + \frac{\pi}{2} J_2(k_\rho \rho) e^{-j2\phi} \quad (5.26d)$$



From the identity $J_{-n}(x) = (-1)^n J_n(x)$ [69, Eq. (IV-8)], it follows that $J_{-2}(x) = J_2(x)$. Substitution in Eq. (5.26d) gives

$$I_\alpha(k_\rho) = \pi J_0(k_\rho \rho) + \pi J_2(k_\rho \rho) \cos 2\phi \quad (5.26e)$$

Substitution of Eq. (5.26e) in Eq. (5.25a) gives

$$\begin{aligned} H_x(\rho, \phi, 0) &= C\pi \int_0^\infty \frac{1}{y_{in}^m(k_\rho)} J_0(k_\rho \rho) k_\rho dk_\rho \\ &+ C\pi \cos 2\phi \int_0^\infty \frac{1}{y_{in}^m(k_\rho)} J_2(k_\rho \rho) k_\rho dk_\rho \\ &= \int_0^\infty F_0(k_\rho) dk_\rho + \cos 2\phi \int_0^\infty F_2(k_\rho) dk_\rho \\ &= I_0(\rho) + \cos 2\phi I_2(\rho) \end{aligned} \quad (5.27a)$$

Using Eq. (5.22c), the integrands $F_0(k_\rho)$ and $F_2(k_\rho)$ in Eq. (5.27a) may be expressed as

$$F_0(k_\rho) = C\pi \frac{k_\rho \varepsilon_1 \varepsilon_2 k_{1z} - \varepsilon_1 k_{2z} \tan k_{1z} h_1 \tan k_{2z} h_2}{k_{1z} D_{TM}} J_0(k_\rho \rho) \quad (5.27b)$$

$$F_2(k_\rho) = C\pi \frac{k_\rho \varepsilon_1 \varepsilon_2 k_{1z} - \varepsilon_1 k_{2z} \tan k_{1z} h_1 \tan k_{2z} h_2}{k_{1z} D_{TM}} J_2(k_\rho \rho) \quad (5.27c)$$

The integrals $I_0(\rho)$ and $I_2(\rho)$ in Eq. (5.27a) are Sommerfeld integrals that need to be evaluated numerically. While the integration path could be deformed (*e.g.*, [77]), the most straightforward approach is to integrate over the positive $\Re e(k_\rho)$ axis (*e.g.*, [78]).¹¹ Each integrand potentially is multi-valued (*i.e.*, four-valued) because of the two possible values each of $k_{1z} = \pm \sqrt{k_1^2 - k_\rho^2}$ and $k_{2z} = \pm \sqrt{k_2^2 - k_\rho^2}$. However, closer inspection of Eqs. (5.27b) and (5.27c) reveals that both integrands are even functions of k_{1z} and k_{2z} ; hence there are no branch points associated with $k_\rho = k_1$ and $k_\rho = k_2$.¹² Plots of the (purely imaginary) integrands $F_0(k_\rho)$ and $F_2(k_\rho)$ are shown in Figs. 5.11–5.14 at $f = 10$ GHz for $h_1 = 0.813$ mm = $0.05\lambda_d$, $h_2 = 5$ mm = $\lambda_0/6$, $\varepsilon_{r1} = 3.38$, and $\varepsilon_{r2} = 1$ (*i.e.*, Substrate I described in Section 5.4.2.1 below; λ_d is the wavelength in the dielectric at 10 GHz, and λ_0 the free-space wavelength). The plots in Figs. 5.11 and 5.12 correspond to $\rho = 20$ mm, while those in Figs. 5.13 and 5.14 are for $\rho = 64.5$ mm; the increased frequency of oscillation in the latter case is due to the larger arguments of the Bessel functions in Eqs. (5.27b) and (5.27c). (These ρ values approximately correspond to the beginning and final inter-slot distance value d in

¹¹ In general, $k_\rho = k'_\rho + jk''_\rho$; however, since the integration path does not involve imaginary values of k_ρ , the integration variable will be denoted as k_ρ throughout.

¹² This is consistent with the observation by Chew [79, p. 113] that branch points are physically associated with lateral waves that are only possible if the outer layers of the substrate are unbounded.



Figs. 5.24–5.40 of Chapter 5.)

Each of the integrations $I_0(\rho)$ and $I_2(\rho)$ can be divided into three regions that are evaluated separately [78]; the regions are $0 \leq k_\rho \leq k_2$ (Region 1), $k_2 \leq k_\rho \leq k_1$ (Region 2), and $k_1 \leq k_\rho$ (Region 3). Total answers are obtained by adding the contributions from the three regions. Region boundaries are indicated in Figs. 5.11–5.14.¹³

The numerical integration in Region 1 is straightforward; while a change of integration variable $k_\rho = k_2 \cos t$ can be performed in order to render the integrand more smooth [78], it is not strictly necessary here.

In Region 2, where $k_2 \leq k_\rho \leq k_1$, the singularities at the poles $k_\rho = k_{\rho,0}$ (cf. Figs. 5.11 and 5.13) and $k_\rho = k_{\rho,2}$ (cf. Figs. 5.12 and 5.14) require special attention. A familiar singularity extraction procedure [78, pp. 253-256] [80] is followed, which entails that a function containing the singularity is subtracted from the integrand (which may be F_0 or F_2), and then added to it. The integral of the function containing the singularity can be evaluated analytically, while the difference between the integrand and the function containing the singularity is an analytical function that can be integrated numerically. Thus,

$$\begin{aligned} F_i(k_\rho) &= [F_i(k_\rho) - F_{sing,i}(k_\rho)] + F_{sing,i}(k_\rho) \\ &= F_{d,i}(k_\rho) + F_{sing,i}(k_\rho) \end{aligned} \quad (5.28a)$$

where F_i is the integrand, $F_{d,i} = F_i(k_\rho) - F_{sing,i}(k_\rho)$ is the function from which the singularity has been extracted that can be integrated numerically, and $F_{sing,i}$ is the function containing the singularity given by

$$F_{sing,i} = \frac{R_i}{k_\rho - k_{\rho,i}} \quad (5.28b)$$

In the above, R_i is the residue of the integrand F_i at the pole $k_{\rho,i}$ where $i = 0$ or 2 . Hence the integrals I_i in Eq. (5.27a) can be expressed in Region 2 as (cf. [78])

$$I_i = I_{d,i} + I_{sing,i} \quad (5.29a)$$

with

$$I_{d,i} = \int_{k_2}^{k_1} [F_i(k_\rho) - F_{sing,i}(k_\rho)] dk_\rho \quad (5.29b)$$

and

$$I_{sing,i} = \int_{k_2}^{k_1} F_{sing,i}(k_\rho) dk_\rho = R_i \ln \left(\frac{k_1 - k_{\rho,i}}{k_{\rho,i} - k_2} \right) \quad (5.29c)$$

¹³ Since $k_1 = \sqrt{\varepsilon_r} k_0$ and $k_2 = k_0$ for the present substrate, $k_1 > k_2$.

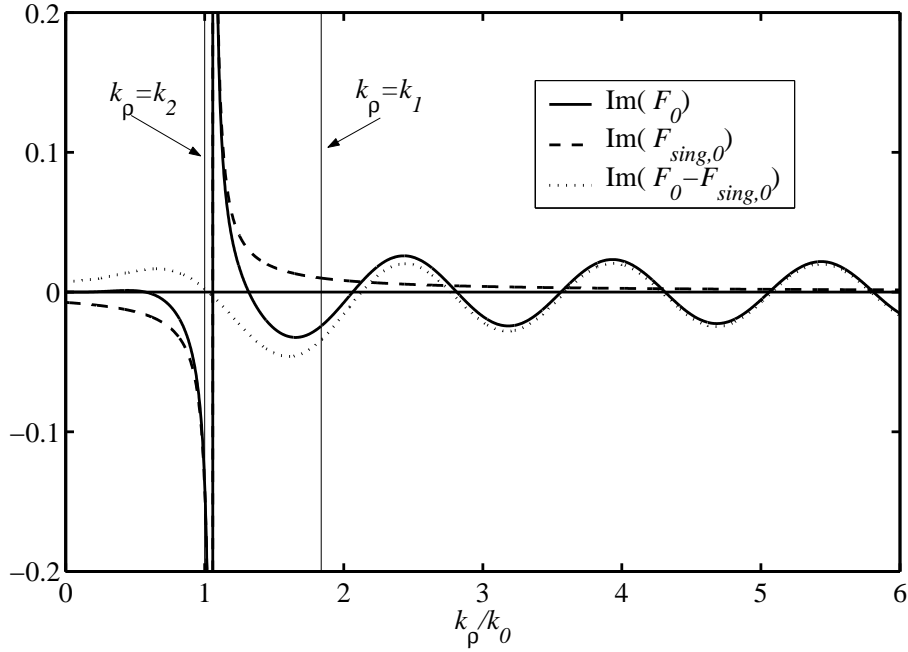


FIGURE 5.11: The integrand $F_0(k_\rho)$, the function containing the singularity $F_{sing,0}(k_\rho)$, and their difference. $f = 10$ GHz, $\rho = 20$ mm, $h_1 = 0.813$ mm $= 0.05\lambda_d$, $h_2 = 5$ mm $= \lambda_0/6$, $\epsilon_{r1} = 3.38$, $\epsilon_{r2} = 1$.

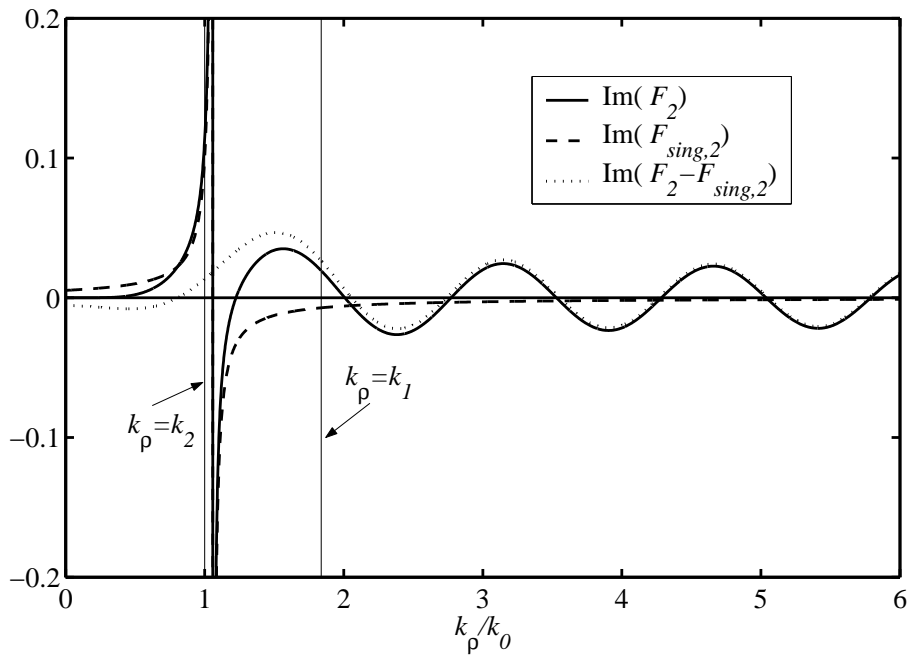


FIGURE 5.12: The integrand $F_2(k_\rho)$, the function containing the singularity $F_{sing,2}(k_\rho)$, and their difference. $f = 10$ GHz, $\rho = 20$ mm, $h_1 = 0.813$ mm $= 0.05\lambda_d$, $h_2 = 5$ mm $= \lambda_0/6$, $\epsilon_{r1} = 3.38$, $\epsilon_{r2} = 1$.

The smoothness of the difference function $F_{d,i}$ can be enhanced by the change of variables $k_\rho = k_0 \cosh t$ [78]. Eq. (5.29b) then becomes (similar to [78, Eq. (7.90)])¹⁴

¹⁴ In Eq. (7.90) of [78], the radical sign in the upper boundary has erroneously been omitted.

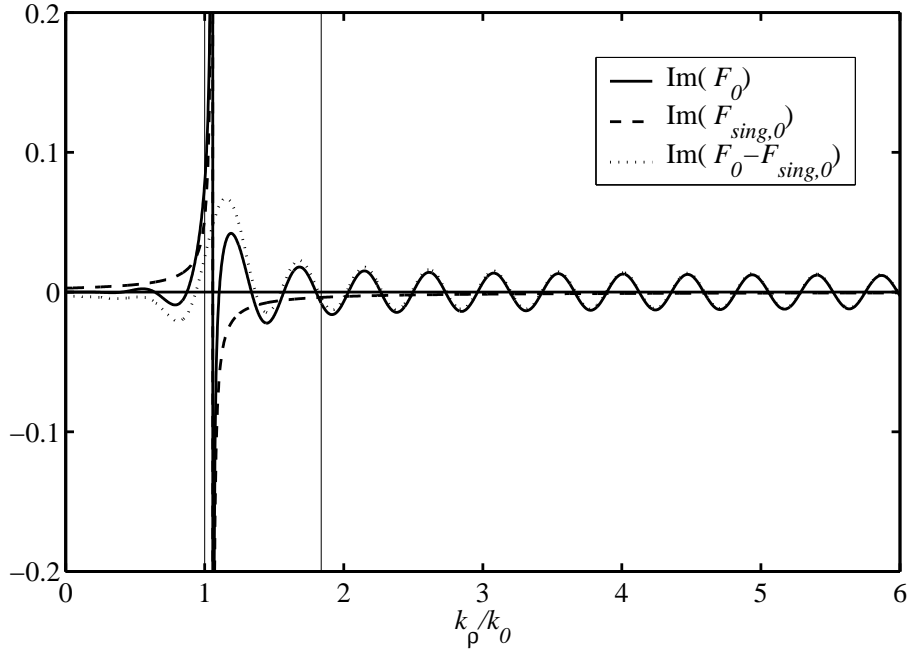


FIGURE 5.13: The integrand $F_0(k_\rho)$, the function containing the singularity $F_{sing,0}(k_\rho)$, and their difference. $f = 10$ GHz, $\rho = 64.5$ mm, $h_1 = 0.813$ mm $= 0.05\lambda_d$, $h_2 = 5$ mm $= \lambda_0/6$, $\epsilon_{r1} = 3.38$, $\epsilon_{r2} = 1$.

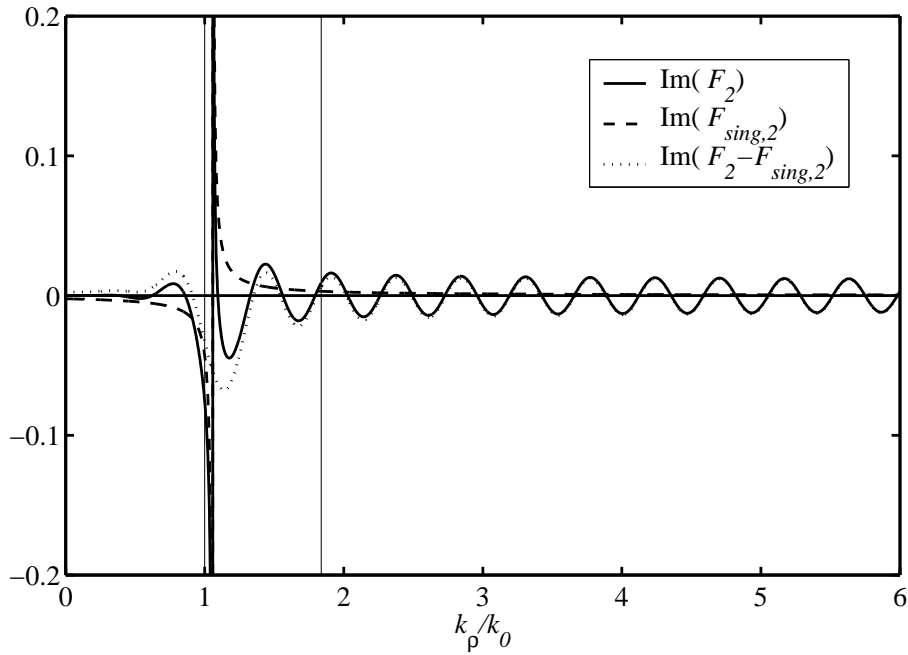


FIGURE 5.14: The integrand $F_2(k_\rho)$, the function containing the singularity $F_{sing,2}(k_\rho)$, and their difference. $f = 10$ GHz, $\rho = 64.5$ mm, $h_1 = 0.813$ mm $= 0.05\lambda_d$, $h_2 = 5$ mm $= \lambda_0/6$, $\epsilon_{r1} = 3.38$, $\epsilon_{r2} = 1$.

$$I_{d,i} = \int_0^{\cosh^{-1} \sqrt{\epsilon_{r1}}} [F_i(k_0 \cosh t) - F_{sing,i}(k_0 \cosh t)] k_0 \sinh t dt \quad (5.29d)$$



The residue R_i in Eq. (5.29c) may be evaluated by noting that if a complex function $f(k_\rho)$ can be written as a quotient $f(k_\rho) = \frac{g(k_\rho)}{h(k_\rho)}$ with $g(k_\rho)$ and $h(k_\rho)$ analytical at $k_\rho = k_{\rho 0}$, and if h has a zero of order 1 at $k_\rho = k_{\rho 0}$ such that f has a simple pole at $k_\rho = k_{\rho 0}$, then

$$\text{Res}(f(k_\rho), k_{\rho 0}) = \frac{g(k_{\rho 0})}{h'(k_{\rho 0})} \quad (5.30)$$

where $\text{Res}(f(k_\rho), k_{\rho 0})$ is the residue of f at the pole $k_{\rho 0}$ [81, p. 875]. From Eqs. (5.27b)–(5.27c), the integrand F_i , where $i = 0$ or 2 , can be expressed as

$$F_i(k_\rho) = \frac{g_i(k_\rho)}{h(k_\rho)} \quad (5.31a)$$

with

$$g_i(k_\rho) = C\pi\varepsilon_1(j\varepsilon_2k_{1z} - j\varepsilon_1k_{2z} \tan k_{1z}h_1 \tan k_{2z}h_2)J_i(k_\rho\rho)k_\rho \quad (5.31b)$$

$$h(k_\rho) = jk_{1z}D_{TM} \quad (5.31c)$$

The residue R_i of F_i at the pole $k_{\rho 0, i}$ is given by

$$\begin{aligned} R_i &= \text{Res}(F_i, k_{\rho 0, i}) \\ &= \frac{g_i(k_{\rho 0, i})}{h'(k_{\rho 0, i})} \end{aligned} \quad (5.32)$$

In the above, the numerator $g_i(k_{\rho 0, i})$ can be found from Eq. (5.31b), while the denominator $h'(k_{\rho 0, i})$ can be expressed as

$$h'(k_{\rho 0, i}) = \left[D_{TM} \frac{d}{dk_\rho} \{jk_{1z}\} + jk_{1z} \frac{d}{dk_\rho} \{D_{TM}\} \right]_{k_\rho=k_{\rho 0, i}} \quad (5.33a)$$

The derivatives in Eq. (5.33a) can be determined as follows. First,

$$\frac{d}{dk_\rho} \{jk_{1z}\} = -j \frac{k_\rho}{k_{1z}} \quad (5.33b)$$

Second,

$$\frac{d}{dk_\rho} \{D_{TM}\} = \frac{d}{dk_\rho} \{D_{TM1}\} + \frac{d}{dk_\rho} \{D_{TM2}\} \quad (5.33c)$$

In the preceding equation,

$$\begin{aligned} D_{TM1} &= -\varepsilon_1 k_{2z} \tan k_{2z} h_2 \\ D_{TM2} &= -\varepsilon_2 k_{1z} \tan k_{1z} h_1 \end{aligned} \quad (5.33d)$$

and

$$\begin{aligned} \frac{d}{dk_\rho} \{D_{TM1}\} &= -\varepsilon_2 \left[-k_\rho h_1 \sec^2 k_{1z} h_1 - \frac{k_\rho}{k_{1z}} \tan k_{1z} h_1 \right] \\ \frac{d}{dk_\rho} \{D_{TM2}\} &= -\varepsilon_1 \left[-k_\rho h_2 \sec^2 k_{2z} h_2 - \frac{k_\rho}{k_{2z}} \tan k_{2z} h_2 \right] \end{aligned} \quad (5.33e)$$



In Region 3, the integrands F_0 and F_2 are slowly converging oscillating functions that can be difficult to integrate numerically.¹⁵ The corresponding integrals I_i in Eq. (5.27a) can be expressed as

$$I_i = \int_{k_1}^{k_{\rho,upper}} F_i(k_{\rho}\rho) dk_{\rho} \quad (5.34)$$

where $i = 0$ or 2 . In order to determine how large the upper integration boundary $k_{\rho,upper}$ had to be set, an iterative procedure suggested by Davidson [78, p. 257] was implemented. This involves repeatedly evaluating the integral with an increasing upper bound until a further increase in the upper bound makes no significant difference to the answer. In particular, the integral was initially evaluated for $k_{\rho,upper} = 10k_2 (= 10k_0)$ and $k_{\rho,upper} = 20k_2$. The difference between the results was computed and normalized by the magnitude of the integral in Region 2, which typically contributes the most to the total integral due to the presence of the pole. If the normalized difference was above a threshold value (which always was the case), the upper integration limits were doubled, *i.e.*, to $k_{\rho,upper} = 20k_2$ and $k_{\rho,upper} = 40k_2$ for the second iteration, and a new normalized difference computed for comparison to the threshold. This procedure was repeated until the normalized difference was below the threshold value (typically 2% of the magnitude of the integral in Region 2). Similar results were obtained by independently using a strategy based on the method of weighted averages for evaluating the tails of Sommerfeld integrals described in [80] and explained in greater detail in [83].

Since the integrals I_0 and I_2 in Eq. (5.27a) are functions of ρ only, it was only necessary to evaluate them once for a suitable range of ρ , and then store the resulting values in a lookup table from where they could be retrieved and/or interpolated in the course of evaluating Y_{12}^{int} (*cf.* Eqs. (5.12) and (5.13b)).

5.3.2 H_x^{TE} for \hat{x} -directed HMD against top conducting plate inside two-layer parallel-plate substrate

Consider the two-layer parallel-plate substrate of Fig. 5.8. As before, the substrate is excited by a HMD at the origin,

$$\mathbf{M}_s = M_{sx}\hat{x} = \delta(x)\delta(y)\hat{x} \quad (5.35)$$

The objective is to find \tilde{B}_z^{TE} from which all remaining TE field components can be determined (the superscript TE will be omitted for the remainder of the section). B_z and \tilde{B}_z are a Fourier transform pair (*cf.* Eq. (5.14)). In layer i , H_x can be expressed directly in terms of \tilde{B}_z [71, p. 28] as follows:

$$H_x(x, y, z) = -\frac{j}{\mu_0} \int_{-\infty}^{\infty} \int_{-\infty}^{\infty} \frac{k_x}{k_i^2 - k_{iz}^2} \frac{\partial \tilde{B}_z(k_x, k_y, z)}{\partial z} e^{-jk_x x} e^{-jk_y y} dk_x dk_y \quad (5.36)$$

¹⁵ Integration of the oscillating tails of Sommerfeld integrals is discussed at length in [82].

In the above, $k_{iz} = \sqrt{k_i^2 - k_x^2 - k_y^2}$ where $k_i = \omega\sqrt{\mu_i\varepsilon_i} = \omega\sqrt{\mu_0\varepsilon_0\varepsilon_{ri}}$ is the wavenumber of dielectric layer i , and $i = 1$ or 2 .

For a two-layer parallel-plate substrate, the general multilayer TE mode spectral domain equivalent transmission line circuit ([71], Fig. 2.2) reduces to the circuit shown in Fig. 5.15, where the transmission line voltage $V(z)$ equals $\tilde{B}_z(k_x, k_y, z)$ of Eq. (5.36). The parallel-plates of the substrate are represented by short circuits in the equivalent circuit. This is required since B_z , the component of the magnetic field normal to the plates, is zero on them. The voltage at the input to the transmission line is denoted $V(0^+)$ (as opposed to $V(0)$ in the TM equivalent circuit of Fig. 5.10), as a discontinuity in voltage is presented by the series voltage source V_0 .

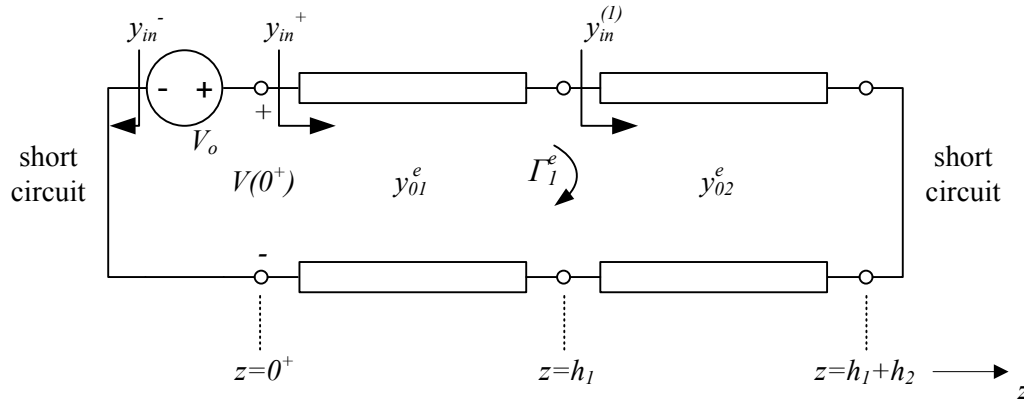


FIGURE 5.15: TE mode spectral domain equivalent circuit for two-layer parallel-plate substrate with planar magnetic current excitation at $z = 0$.

If only points in the plane $z = 0$ are considered, Eq. (5.36) reduces to¹⁶

$$\begin{aligned}
 H_x(x, y, 0^+) &= -\frac{j}{\mu_0} \int_{-\infty}^{\infty} \int_{-\infty}^{\infty} \frac{k_x}{k_1^2 - k_{1z}^2} \left[\frac{\partial \tilde{B}_z(k_x, k_y, z)}{\partial z} \right]_{z=0^+} e^{-jk_x x} e^{-jk_y y} dk_x dk_y \\
 &= -\frac{j}{\mu_0} \int_{-\infty}^{\infty} \int_{-\infty}^{\infty} \frac{k_x}{k_1^2 - k_{1z}^2} \left[\frac{\partial V_1(z)}{\partial z} \right]_{z=0^+} e^{-jk_x x} e^{-jk_y y} dk_x dk_y \quad (5.37a)
 \end{aligned}$$

In Eq. (5.37a), $V_1(z)$ is the transmission line voltage corresponding to layer 1. $V_1(z)$ can be found from [71, Eq. (2.25)] as

$$V_1(z) = V(0^+) \frac{e^{-jk_{1z}(z-h_1)} + \Gamma_1^e e^{jk_{1z}(z-h_1)}}{e^{jk_{1z}h_1} + \Gamma_1^e e^{-jk_{1z}h_1}} \quad (5.37b)$$

¹⁶ For practical purposes there is negligible difference between H_x evaluated at $z = 0^+$ and $z = 0$ due to continuity of the tangential magnetic field. The former form is however preferred for mathematical convenience as it lends itself to ready application of certain mathematical identities.



In Eq. (5.37b), Γ_1^e is given by

$$\Gamma_1^e = \frac{y_{01}^e - y_{in}^{(1)}}{y_{01}^e + y_{in}^{(1)}} \quad (5.37c)$$

where $y_{in}^{(1)} = -jy_{02}^e \cot k_{2z}h_2$, $y_{0i}^e = jk_{iz}/\mu_0$ is the (TE) characteristic admittance of transmission line i , and $i = 1$ or 2 . Differentiating Eq. (5.37a) once with respect to z yields

$$\begin{aligned} \left[\frac{dV_1(z)}{dz} \right]_{z=0^+} &= jk_{1z}V(0^+) \frac{-1 + \Gamma_1^e e^{-2jk_{1z}h_1}}{1 + \Gamma_1^e e^{-2jk_{1z}h_1}} \\ &= jk_{1z}V_0 \frac{-1 + \Gamma_1^e e^{-2jk_{1z}h_1}}{1 + \Gamma_1^e e^{-2jk_{1z}h_1}} \end{aligned} \quad (5.37d)$$

In the above, V_0 is the value of the voltage source in the equivalent circuit, given by [71, Table 2.1] as

$$V_0 = \tilde{\rho}_{ms} \quad (5.38a)$$

In the above, $\tilde{\rho}_{ms}$ is the Fourier transform of ρ_{ms} , the magnetic surface charge density of the source. ρ_{ms} can be related to the magnetic surface current density \mathbf{M}_s by means of the continuity relation

$$\nabla \cdot \mathbf{M}_s = -j\omega\rho_{ms} \quad (5.38b)$$

Taking the two-dimensional Fourier transform of Eq. (5.38b) yields

$$-j\omega\tilde{\rho}_{ms} = -j\mathbf{k}_\rho \cdot \tilde{\mathbf{M}}_s \quad (5.38c)$$

Combining Eqs. (5.21b), (5.38a) and (5.38c) gives

$$V_0 = \frac{k_x}{4\pi^2\omega} \quad (5.38d)$$

and combining Eqs. (5.38d), (5.37d), and (5.37a) yields

$$H_x(x, y, 0^+) = -\frac{j}{4\pi^2\omega\mu_0} \int_{-\infty}^{\infty} \int_{-\infty}^{\infty} \frac{k_x^2}{k_1^2 - k_{1z}^2} jk_{1z}V_0 \frac{-1 + \Gamma_1^e e^{-2jk_{1z}h_1}}{1 + \Gamma_1^e e^{-2jk_{1z}h_1}} e^{-jk_x x} e^{-jk_y y} dk_x dk_y \quad (5.39)$$

Now substitute Eq. (5.24) in Eq. (5.39) in order to effect a transformation in the spectral domain from rectangular coordinates (k_x, k_y) into cylindrical coordinates (k_ρ, α) . This gives

$$\begin{aligned} H_x(x, y, 0^+) &= C \int_{\alpha=0}^{2\pi} \int_{k_\rho=0}^{\infty} \frac{k_\rho^2 \cos^2 \alpha}{k_\rho^2} G(k_\rho) e^{-j(k_\rho \cos \alpha \cdot \rho \cos \phi + k_\rho \sin \alpha \cdot \rho \sin \phi)} k_\rho dk_\rho d\alpha \\ &= C \int_0^{\infty} G(k_\rho) \int_0^{2\pi} \cos^2 \alpha e^{-jk_\rho \rho \cos(\alpha-\phi)} d\alpha k_\rho dk_\rho \\ &= C \int_0^{\infty} G(k_\rho) I_\alpha(k_\rho) k_\rho dk_\rho \end{aligned} \quad (5.40a)$$



In Eq. (5.40a), $C = \frac{1}{4\pi^2\omega}$,¹⁷ while $G(k_\rho)$ and $I_\alpha(k_\rho)$ are given by

$$G(k_\rho) = k_{1z} \frac{-1 + \Gamma_1^e e^{-2jk_{1z}h_1}}{1 + \Gamma_1^e e^{-2jk_{1z}h_1}} \quad (5.40b)$$

$$I_\alpha(k_\rho) = \int_{-\phi}^{2\pi-\phi} \cos^2(\alpha + \phi) e^{-jk_\rho \rho \cos \alpha} d\alpha \quad (5.40c)$$

Substituting the identity Eq. (5.26a) into Eq. (5.40c) yields

$$I_\alpha(k_\rho) = \sum_{n=-\infty}^{\infty} j^{-n} J_n(k_\rho \rho) e^{-jn\phi} \int_0^{2\pi} e^{jn\alpha} \cos^2 \alpha d\alpha \quad (5.41a)$$

The integral on the right-hand side of Eq. (5.41a) can be solved using a standard identity [76, Eq. 14.524] in conjunction with l'Hospital's rule:

$$\int_0^{2\pi} e^{jn\alpha} \cos^2 \alpha d\alpha = \begin{cases} \pi, & n = 0 \\ \frac{\pi}{2}, & n = -2, 2 \\ 0, & \text{otherwise} \end{cases} \quad (5.41b)$$

Substituting Eq. (5.41b) into Eq. (5.41a) yields

$$I_\alpha(k_\rho) = -\frac{\pi}{2} J_{-2}(k_\rho \rho) e^{j2\phi} + \pi J_0(k_\rho \rho) - \frac{\pi}{2} J_2(k_\rho \rho) e^{-j2\phi} \quad (5.41c)$$

Since $J_{-2}(x) = J_2(x)$, Eq. (5.41c) becomes

$$I_\alpha(k_\rho) = \pi J_0(k_\rho \rho) - \pi J_2(k_\rho \rho) \cos 2\phi \quad (5.41d)$$

Substitution of Eq. (5.41d) in Eq. (5.40a) gives

$$\begin{aligned} H_x(x, y, 0^+) &= C\pi \int_0^\infty G(k_\rho) J_0(k_\rho \rho) k_\rho dk_\rho \\ &\quad - C\pi \cos 2\phi \int_0^\infty G(k_\rho) J_2(k_\rho \rho) k_\rho dk_\rho \\ &= \int_0^\infty F_0(k_\rho) dk_\rho - \cos 2\phi \int_0^\infty F_2(k_\rho) dk_\rho \\ &= I_0(\rho) - \cos 2\phi I_2(\rho) \end{aligned} \quad (5.42a)$$

Using Eq. (5.40b), the integrands $F_0(k_\rho)$ and $F_2(k_\rho)$ in Eq. (5.42a) may be written as

$$F_0(k_\rho) = C\pi k_\rho k_{1z} \frac{-1 + \Gamma_1^e e^{-2jk_{1z}h_1}}{1 + \Gamma_1^e e^{-2jk_{1z}h_1}} J_0(k_\rho \rho) \quad (5.42b)$$

¹⁷ Note that this value of C is different from the corresponding quantity in the derivation of H_x^{TM} in Section 5.3.1.

$$F_2(k_\rho) = C\pi k_\rho k_{1z} \frac{-1 + \Gamma_1^e e^{-2jk_{1z}h_1}}{1 + \Gamma_1^e e^{-2jk_{1z}h_1}} J_2(k_\rho \rho) \quad (5.42c)$$

The integrals $I_0(\rho)$ and $I_2(\rho)$ in Eq. (5.42a) are Sommerfeld integrals that need to be evaluated numerically, integrating over the positive $\Re(k_\rho)$ axis. The possible multi-valued nature of the integrands was investigated given that k_{1z} and k_{2z} each have two possible values. However, inspection of Eqs. (5.42b) and (5.42c) revealed that both integrands are even functions of k_{1z} and k_{2z} ; hence as in the TM case, there are no branch points associated with $k_\rho = k_1$ and $k_\rho = k_2$. Plots of the integrands $F_0(k_\rho)$ and $F_2(k_\rho)$ are shown in Fig. 5.16 at $f = 10$ GHz for $\rho = 20$ mm, $h_1 = 0.813$ mm $= 0.05\lambda_d$, $h_2 = 5$ mm $= \lambda_0/6$, $\epsilon_{r1} = 3.38$, and $\epsilon_{r2} = 1$ (i.e., Substrate I of Section 5.4). The figure confirms that the integrands $F_0(k_\rho)$ and $F_2(k_\rho)$ are non-convergent, rendering the integrals $I_0(\rho)$ and $I_2(\rho)$ singular and therefore unsuitable for direct numerical integration (cf. [79, p. 118]).

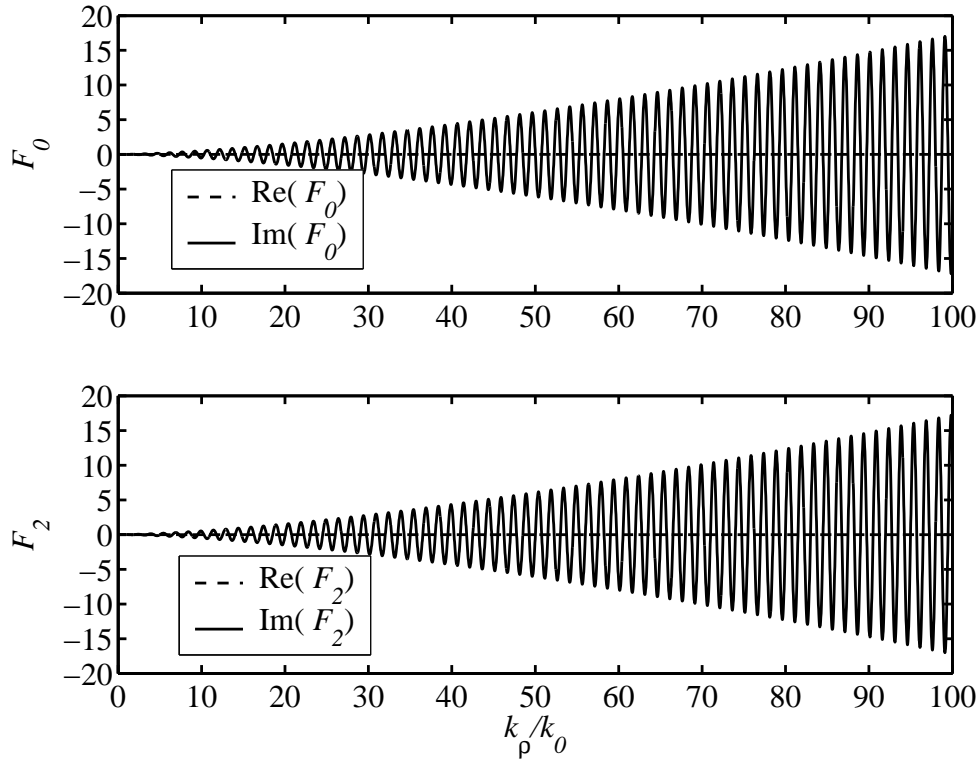


FIGURE 5.16: Plots of the TE integrands $F_0(k_\rho)$ and $F_2(k_\rho)$ for the two-layer parallel-plate substrate of Fig. 5.8. $f = 10$ GHz, $\rho = 20$ mm, $h_1 = 0.813$ mm $= 0.05\lambda_d$, $h_2 = 5$ mm $= \lambda_0/6$, $\epsilon_{r1} = 3.38$, $\epsilon_{r2} = 1$.

The evaluation of singular integrals of this nature, which typically arise when source and observation points lie in the same plane, is treated by Hansen [84] for substrates that have a conductor on one side only. The strategy implemented here to solve I_0 and I_2 in Eq. (5.42a) follows a broadly similar approach, requiring two further results. The first result entails expressions in integral form as



well as closed form for H_x^{TE} due to an \hat{x} -directed HMD placed at the origin of a homogenous medium with dielectric parameters $(\varepsilon_0\varepsilon_{r1}, \mu_0)$. The second is H_x^{TE} in integral form due to an \hat{x} -directed HMD inside the two-layer parallel-plate substrate of Fig. 5.8 with the conducting plane on the side of the source removed, and the adjacent half-space filled by a dielectric $(\varepsilon_0\varepsilon_{r1}, \mu_0)$ (the HMD is placed where it would have resided in the original two-layer parallel-plate substrate). These two results are derived in Sections 5.3.2.1 and 5.3.2.2 respectively. In Section 5.3.2.3, it is shown how they may be applied towards evaluating I_0 and I_2 in Eq. (5.42a).

5.3.2.1 H_x^{TE} of \hat{x} -directed HMD in homogenous medium

Consider a homogenous medium with permittivity $\varepsilon_1 = \varepsilon_0\varepsilon_{r1}$ and permeability μ_0 that is excited by a HMD at the origin, $\mathbf{M}_s = M_{sx}\hat{x} = \delta(x)\delta(y)\hat{x}$. As before, the objective is to find \tilde{B}_z^{TE} from which all TE field components can be determined (the superscript TE will be omitted for the remainder of the section). In half-space I corresponding to $z > 0$, H_x can be expressed directly in terms of \tilde{B}_z [71, p. 28]; that is,

$$H_x(x, y, z) = -\frac{j}{\mu_0} \int_{-\infty}^{\infty} \int_{-\infty}^{\infty} \frac{k_x}{k_1^2 - k_{1z}^2} \frac{\partial \tilde{B}_z(k_x, k_y, z)}{\partial z} e^{-jk_x x} e^{-jk_y y} dk_x dk_y \quad (5.43)$$

In the above, $k_{1z} = \sqrt{k_1^2 - k_x^2 - k_y^2}$ where $k_1 = \omega\sqrt{\mu_0\varepsilon_1}$ is the wave number.

For this medium, the general multilayer TE mode spectral domain equivalent transmission line circuit ([71], Fig. 2.2) reduces to the circuit shown in Fig. 5.17, which consists of two semi-infinite transmission lines fed by a series voltage source. The transmission line voltage $V(z)$ equals $\tilde{B}_z(k_x, k_y, z)$ of Eq. (5.43). Hence, for half-space I the latter equation becomes

$$H_x(x, y, z) = -\frac{j}{\mu_0} \int_{-\infty}^{\infty} \int_{-\infty}^{\infty} \frac{k_x}{k_1^2 - k_{1z}^2} \frac{\partial V_1(z)}{\partial z} e^{-jk_x x} e^{-jk_y y} dk_x dk_y \quad (5.44a)$$

$V_1(z)$ in Eq. (5.44a) can be determined from [71, Eq. (2.25)] as follows:

$$V_1(z) = V(0^+)e^{-jk_{1z}z} \quad (5.44b)$$

Since the characteristic admittances y_{01}^e and $y_{0,-1}^e$ are equal, voltage division yields

$$V(0^+) = \frac{V_0}{2} \quad (5.44c)$$

Combining the first derivative of Eq. (5.44b) with Eq. (5.44c) yields

$$\frac{dV_1(z)}{dz} = -jk_{1z} \frac{V_0}{2} e^{-jk_{1z}z} \quad (5.44d)$$

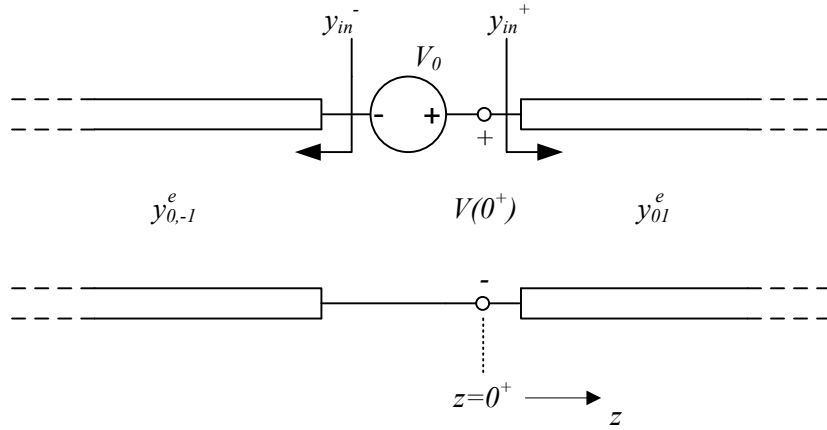


FIGURE 5.17: TE mode spectral domain equivalent circuit for homogeneous full-space with planar magnetic current excitation at $z = 0$.

Furthermore, combining Eqs. (5.38d), (5.44d) and (5.44a) gives

$$H_x(x, y, z) = \frac{1}{8\pi^2\omega\mu_0} \int_{-\infty}^{\infty} \int_{-\infty}^{\infty} \frac{k_x^2}{k_1^2 - k_{1z}^2} (-k_{1z} e^{-jk_{1z}z}) e^{-jk_x x} e^{-jk_y y} dk_x dk_y \quad (5.45)$$

Now substitute Eq. (5.24) in Eq. (5.45) in order to effect a transformation in the spectral domain from rectangular to cylindrical coordinates. A manipulation similar to that used to derive Eq. (5.42) from Eq. (5.40) gives

$$\begin{aligned} H_x(\rho, \phi, z) &= C^H \pi \int_0^{\infty} (-k_{1z} e^{-jk_{1z}z}) J_0(k_\rho \rho) k_\rho dk_\rho \\ &\quad - C^H \pi \cos 2\phi \int_0^{\infty} (-k_{1z} e^{-jk_{1z}z}) J_2(k_\rho \rho) k_\rho dk_\rho \\ &= C^H \pi [i_0^H(\rho, z) - \cos 2\phi i_2^H(\rho, z)] \end{aligned} \quad (5.46a)$$

In the preceding equation, $C^H = \frac{1}{8\pi^2\omega\mu_0}$ and

$$i_0^H(\rho, z) = \int_0^{\infty} (-k_{1z} e^{-jk_{1z}z}) J_0(k_\rho \rho) k_\rho dk_\rho \quad (5.46b)$$

$$i_2^H(\rho, z) = \int_0^{\infty} (-k_{1z} e^{-jk_{1z}z}) J_2(k_\rho \rho) k_\rho dk_\rho \quad (5.46c)$$



Restricting Eq. (5.46a) to points in the plane $z = 0^+$ results in

$$\begin{aligned}
 H_x(\rho, \phi, z = 0^+) &= \lim_{z \rightarrow 0^+} \left[C^H \pi \int_0^\infty (-k_{1z} e^{-jk_{1z}z}) J_0(k_\rho \rho) k_\rho dk_\rho \right] \\
 &\quad - \lim_{z \rightarrow 0^+} \left[C^H \pi \cos 2\phi \int_0^\infty (-k_{1z} e^{-jk_{1z}z}) J_2(k_\rho \rho) k_\rho dk_\rho \right] \\
 &= \lim_{z \rightarrow 0^+} C^H \pi [i_0^H(\rho, z) - \cos 2\phi i_2^H(\rho, z)] \\
 &= I_0^H(\rho) - \cos 2\phi I_2^H(\rho)
 \end{aligned} \tag{5.47a}$$

The objective is to find $I_0^H(\rho)$ and $I_2^H(\rho)$ in closed form; this entails determining closed-form expressions for

$$\begin{aligned}
 \lim_{z \rightarrow 0^+} i_0^H(\rho, z) &= \lim_{z \rightarrow 0^+} \left[\int_0^\infty (-k_{1z} e^{-jk_{1z}z}) J_0(k_\rho \rho) k_\rho dk_\rho \right] \\
 &= \frac{I_0^H(\rho)}{C^H \pi} \\
 &= \frac{1}{C^H \pi} \int_0^\infty F_0^H(k_\rho) dk_\rho
 \end{aligned} \tag{5.47b}$$

and

$$\begin{aligned}
 \lim_{z \rightarrow 0^+} i_2^H(\rho, z) &= \lim_{z \rightarrow 0^+} \left[\int_0^\infty (-k_{1z} e^{-jk_{1z}z}) J_2(k_\rho \rho) k_\rho dk_\rho \right] \\
 &= \frac{I_2^H(\rho)}{C^H \pi} \\
 &= \frac{1}{C^H \pi} \int_0^\infty F_2^H(k_\rho) dk_\rho
 \end{aligned} \tag{5.47c}$$

In Eqs. (5.47b) and (5.47c), the integrands F_0^H and F_2^H can be expressed as

$$F_0^H(k_\rho) = \lim_{z \rightarrow 0^+} (-k_\rho k_{1z} e^{-jk_{1z}z}) J_0(k_\rho \rho) \tag{5.47d}$$

$$F_2^H(k_\rho) = \lim_{z \rightarrow 0^+} (-k_\rho k_{1z} e^{-jk_{1z}z}) J_2(k_\rho \rho) \tag{5.47e}$$

$\lim_{z \rightarrow 0^+} i_0^H(\rho, z)$ in Eq. (5.47b) can be found by utilizing the identity [85, Eq. (A3)]

$$- \lim_{z \rightarrow 0^+} \int_0^\infty dk_\rho k_\rho k_z J_0(k_\rho \rho) e^{-jk_z z} = \left(\frac{k}{\rho^2} - \frac{j}{\rho^3} \right) e^{-jk\rho} \tag{5.48a}$$

which in turn is derived from the Sommerfeld identity [86, Eq. (A1)]

$$\int_0^\infty dk_\rho \frac{k_\rho}{k_z} e^{-jk_z z} J_0(k_\rho \rho) = \frac{j e^{-jk\rho}}{r} \tag{5.48b}$$



where $r = \sqrt{\rho^2 + z^2}$, by differentiating twice with respect to z and then taking the limit $z \rightarrow 0^+$. In particular,

$$\begin{aligned} \lim_{z \rightarrow 0^+} i_0^H(\rho, z) &= \left(\frac{k_1}{\rho^2} - \frac{j}{\rho^3} \right) e^{-jk_1\rho} \\ &= \frac{I_0^H(\rho)}{C^H\pi} \end{aligned} \quad (5.48c)$$

The derivation of $\lim_{z \rightarrow 0^+} i_2^H(\rho, z)$ in Eq. (5.47c), on the other hand, requires more effort due to the presence of $J_2(k_\rho\rho)$ in the integrand. Subtracting the identities [87, Eq. 9.1.27]

$$J_1'(z) = J_0(z) - \frac{1}{z}J_1(z) \quad (5.49a)$$

$$J_1'(z) = -J_2(z) + \frac{1}{z}J_1(z) \quad (5.49b)$$

yields

$$J_2(z) = -J_0(z) + \frac{2}{z}J_1(z) \quad (5.49c)$$

Substituting Eqs. (5.49c) into (5.46c) gives

$$i_2^H = i_{21}^H - \frac{2}{\rho}i_{22}^H \quad (5.50a)$$

with

$$i_{21}^H = \int_0^\infty dk_\rho k_\rho k_{1z} e^{-jk_{1z}z} J_0(k_\rho\rho) \quad (5.50b)$$

$$i_{22}^H = \int_0^\infty dk_\rho k_{1z} e^{-jk_{1z}z} J_1(k_\rho\rho) \quad (5.50c)$$

Combining Eqs. (5.50b) and (5.48a) gives

$$\lim_{z \rightarrow 0^+} i_{21}^H(\rho, z) = \left(\frac{j}{\rho^3} - \frac{k_1}{\rho^2} \right) e^{-jk_1\rho} \quad (5.51)$$

$\lim_{z \rightarrow 0^+} i_{22}^H(\rho, z)$ can be determined as follows. Noting from the identity [87, Eq. 9.1.28] that

$$J_0'(z) = \frac{dJ_0(z)}{dz} = -J_1(z) \quad (5.52)$$

it follows that Eq. (5.50c) can be expressed as

$$i_{22}^H = \int u(k_\rho)v'(k_\rho)dk_\rho \quad (5.53a)$$

with

$$u(k_\rho) = k_{1z}e^{-jk_{1z}z} \quad (5.53b)$$

$$v(k_\rho) = -\frac{1}{\rho}J_0(k_\rho\rho) \quad (5.53c)$$



(the chain rule of differentiation applied to Eq. (5.53c) gives $v'(k_\rho) = J_1(k_\rho\rho)$). Applying the integration-by-parts formula [88]

$$\int u(k_\rho)v'(k_\rho)dk_\rho = u(k_\rho)v(k_\rho) - \int u'(k_\rho)v(k_\rho)dk_\rho \quad (5.54)$$

to the right-hand side Eq. (5.50c) expressed in the form of Eq. (5.53) gives

$$i_{22}^H = f_{22}^H - i_{221}^H \quad (5.55a)$$

with

$$f_{22}^H = -\frac{1}{\rho} \left[k_{1z} e^{-jk_{1z}z} J_0(k_\rho\rho) \right]_{k_\rho=0}^{k_\rho=\infty} \quad (5.55b)$$

$$i_{221}^H = \int_0^\infty u'(k_\rho)v(k_\rho)dk_\rho \quad (5.55c)$$

Combining Eq. (5.53b), (5.53c) and (5.55c) yields

$$\begin{aligned} i_{221}^H &= \frac{1}{\rho} \int_0^\infty dk_\rho \frac{k_\rho}{k_{1z}} e^{-jk_{1z}z} J_0(k_\rho\rho) - \frac{jz}{\rho} \int_0^\infty dk_\rho k_\rho e^{-jk_{1z}z} J_0(k_\rho\rho) \\ &= \frac{j}{\rho} \frac{e^{-jk_1 r}}{r} - \frac{jz^2}{\rho} \left(\frac{1}{r^3} + \frac{jk_1}{r^2} \right) e^{-jk_1 r} \end{aligned} \quad (5.56)$$

To arrive at the above result, use was made of the Sommerfeld identity Eq. (5.48b) as well as the identity

$$\int_0^\infty dk_\rho k_\rho e^{-jk_z z} J_0(k_\rho\rho) = z \left(\frac{1}{r^3} + \frac{jk}{r^2} \right) e^{-jkr} \quad (5.57)$$

which can be obtained by differentiating the Sommerfeld identity once with respect to z . From Eq. (5.56) it follows that

$$\lim_{z \rightarrow 0^+} i_{221}^H(\rho, z) = \frac{j e^{-jk_1 \rho}}{\rho^2} \quad (5.58)$$

Taking the limit $z \rightarrow 0^+$ with respect to Eq. (5.55b) yields

$$\begin{aligned} \lim_{z \rightarrow 0^+} f_{22}^H(\rho, z) &= - \lim_{z \rightarrow 0^+, k_\rho \rightarrow \infty} \frac{1}{\rho} \left[k_{1z} e^{-jk_{1z}z} J_0(k_\rho\rho) \right] \\ &\quad + \lim_{z \rightarrow 0^+, k_\rho \rightarrow 0} \frac{1}{\rho} \left[k_{1z} e^{-jk_{1z}z} J_0(k_\rho\rho) \right] \end{aligned} \quad (5.59)$$

The negative root $k_{1z} = -\sqrt{k_1^2 - k_\rho^2}$ is now chosen. If $k_\rho \rightarrow \infty$, then

$$k_{1z} \approx -\sqrt{-k_\rho^2} = -jk_\rho \quad (5.60a)$$

Furthermore,

$$\lim_{k_\rho \rightarrow 0} k_{1z} = -\sqrt{k_1^2} = -k_1 \quad (5.60b)$$



Combining Eqs. (5.60) and (5.59) gives

$$\begin{aligned}
 \lim_{z \rightarrow 0^+} f_{22}^H &= \lim_{z \rightarrow 0^+, k_\rho \rightarrow \infty} \frac{j}{\rho} \left[\sqrt{k_\rho} e^{-k_\rho z} \sqrt{\frac{2}{\pi \rho}} \cos(k_\rho \rho - \pi/4) \right] \\
 &+ \lim_{z \rightarrow 0^+} \frac{1}{\rho} \left[-k_1 e^{jk_1 z} \cdot 1 \right] \\
 &= 0 - \frac{k_1}{\rho} \\
 &= -\frac{k_1}{\rho}
 \end{aligned} \tag{5.61}$$

In finding the preceding result, the small and large-argument forms of the zero-order Bessel function J_0 was used [56].

In summary, the integrals $I_0^H(\rho)$ and $I_2^H(\rho)$ in Eq. (5.47a) can be expressed in closed form as follows. From Eq. (5.48c),

$$I_0^H(\rho) = C^H \pi \lim_{z \rightarrow 0^+} i_0^H(\rho, z) = \left(\frac{k_1}{\rho^2} - \frac{j}{\rho^3} \right) e^{-jk_1 \rho} \tag{5.62a}$$

while combining Eqs. (5.50a), (5.51), (5.55a), (5.58), and (5.61) gives

$$I_2^H(\rho) = C^H \pi \lim_{z \rightarrow 0^+} i_2^H(\rho, z) = \frac{2k_1}{\rho^2} + \left(\frac{3j}{\rho^3} - \frac{k_1}{\rho^2} \right) e^{-jk_1 \rho} \tag{5.62b}$$

5.3.2.2 H_x^{TE} of \hat{x} -directed HMD inside two-layer parallel-plate substrate with top conducting plate removed

Consider a substrate that is identical in every respect to the two-layer parallel-plate substrate of Fig. 5.8 except for the conducting plane adjacent to the ϵ_{r1} dielectric layer having been removed, and the half-space $z < 0$ being filled by the same dielectric material as layer 1. As before, the substrate is excited by a HMD at the origin, $\mathbf{M}_s = M_{sx} \hat{x} = \delta(x) \delta(y) \hat{x}$. For this substrate, the general multilayer TE mode spectral domain equivalent transmission line circuit ([71], Fig. 2.2) reduces to the circuit shown in Fig. 5.18.

As in the case of the previous substrates, H_x in layer 1 can be expressed in terms of the equivalent transmission line voltage V_1 (i.e., the voltage in the section of transmission line with characteristic admittance y_{01}^e) as follows:

$$H_x(x, y, z) = -\frac{j}{\mu_0} \int_{-\infty}^{\infty} \int_{-\infty}^{\infty} \frac{k_x}{k_1^2 - k_{1z}^2} \frac{\partial V_1(z)}{\partial z} e^{-jk_x x} e^{-jk_y y} dk_x dk_y \tag{5.63}$$

If only points in the plane $z = 0$ are considered, Eq. (5.63) reduces to

$$H_x(x, y, 0^+) = -\frac{j}{\mu_0} \int_{-\infty}^{\infty} \int_{-\infty}^{\infty} \frac{k_x}{k_1^2 - k_{1z}^2} \left[\frac{\partial V_1(z)}{\partial z} \right]_{z=0^+} e^{-jk_x x} e^{-jk_y y} dk_x dk_y \tag{5.64a}$$

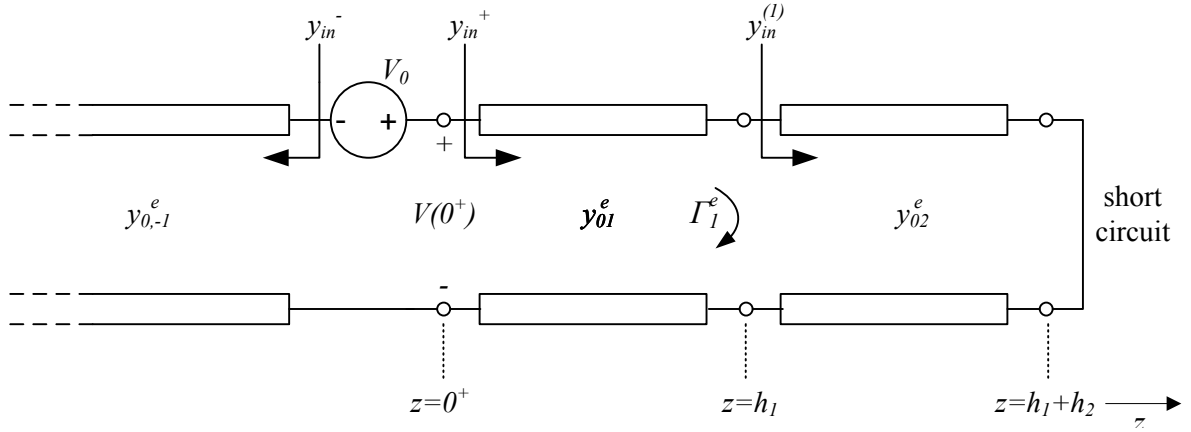


FIGURE 5.18: TE mode spectral domain equivalent circuit for two-layer parallel-plate substrate with top conducting plate removed.

In Eq. (5.64a), $V_1(z)$ can be found from [71, Eq. (2.25)] as

$$V_1(z) = V(0^+) \frac{e^{-jk_{1z}(z-h_1)} + \Gamma_1^e e^{jk_{1z}(z-h_1)}}{e^{jk_{1z}h_1} + \Gamma_1^e e^{-jk_{1z}h_1}} \quad (5.64b)$$

In Eq. (5.64b), which is the same as the corresponding equation for the two-layer-parallel-plate case, Γ_1^e is given by

$$\Gamma_1^e = \frac{y_{01}^e - y_{in}^{(1)}}{y_{01}^e + y_{in}^{(1)}} \quad (5.64c)$$

with $y_{in}^{(1)} = -jy_{02}^e \cot k_{2z}h_2$, and $y_{0i}^e = jk_{iz}/\mu_0$ the (TE) characteristic admittance of transmission line i , where $i = 1$ or 2 . Differentiating Eq. (5.64b) once with respect to z yields

$$\left[\frac{dV_1(z)}{dz} \right]_{z=0^+} = jk_{1z} V(0^+) \frac{-1 + \Gamma_1^e e^{-2jk_{1z}h_1}}{1 + \Gamma_1^e e^{-2jk_{1z}h_1}} \quad (5.64d)$$

$V(0^+)$ in Eq. (5.64d) can be found from voltage division (see Fig. 5.18) as

$$\begin{aligned} V(0^+) &= V_0 \frac{\frac{1}{y_{in}^+}}{\frac{1}{y_{in}^+} + \frac{1}{y_{in}^-}} \\ &= V_0 \frac{y_{in}^-}{y_{in}^- + y_{in}^+} \end{aligned} \quad (5.65a)$$

In the preceding equation, V_0 is the value of the voltage source in the equivalent circuit, while y_{in}^- and y_{in}^+ are given by

$$y_{in}^- = y_{0,-1}^e = y_{01}^e \quad (5.65b)$$

$$\begin{aligned} y_{in}^+ &= y_{01}^e \frac{y_{in}^{(1)} + jy_{01}^e \tan k_{1z}h_1}{y_{01}^e + jy_{in}^{(1)} \tan k_{1z}h_1} \\ &= y_{01}^e \frac{-jy_{02}^e \cot k_{2z}h_2 + jy_{01}^e \tan k_{1z}h_1}{y_{01}^e + y_{02}^e \cot k_{2z}h_2 \tan k_{1z}h_1} \end{aligned} \quad (5.65c)$$



In Eq. (5.65b), $y_{0,-1}^e$ is the (TE) characteristic admittance of transmission line $-l$ corresponding to the half-space $z < 0$.

Substituting Eqs. (5.65) and (5.64d) into Eq. (5.64a), and then implementing the change of variables Eq. (5.24) in order to effect a transformation in the spectral domain from rectangular to cylindrical coordinates ultimately gives

$$\begin{aligned} H_x(\rho, \phi, 0^+) &= \int_0^\infty F_0^A(k_\rho) dk_\rho - \cos 2\phi \int_0^\infty F_2^A(k_\rho) dk_\rho \\ &= I_0^A(\rho) - \cos 2\phi I_2^A(\rho) \end{aligned} \quad (5.66a)$$

The integrands $F_0^A(k_\rho)$ and $F_2^A(k_\rho)$ in Eq. (5.66a) may be expressed as

$$F_0^A(k_\rho) = C^A \pi k_\rho k_{1z} \frac{y_{01}^e}{y_{01}^e + y_{in}^+} \frac{-1 + \Gamma_1^e e^{-2jk_{1z}h_1}}{1 + \Gamma_1^e e^{-2jk_{1z}h_1}} J_0(k_\rho \rho) \quad (5.66b)$$

$$F_2^A(k_\rho) = C^A \pi k_\rho k_{1z} \frac{y_{01}^e}{y_{01}^e + y_{in}^+} \frac{-1 + \Gamma_1^e e^{-2jk_{1z}h_1}}{1 + \Gamma_1^e e^{-2jk_{1z}h_1}} J_2(k_\rho \rho) \quad (5.66c)$$

In Eqs. (5.66b) and (5.66c), $C^A = \frac{1}{4\pi^2 \omega \mu_0}$.

5.3.2.3 Evaluation of singular integrals for H_x^{TE} of \hat{x} -directed HMD against top conducting plate inside two-layer parallel-plate substrate

The integrands of the integrals required to find H_x for each of the three substrates discussed above (*i.e.*, the two-layer parallel-plate substrate, the homogeneous full-space and the two-layer parallel-plate substrate with top plate removed) are F_0 , F_2 , F_0^H , F_2^H , F_0^A , and F_2^A ; they are given in Eqs. (5.42b), (5.42c), (5.47d), (5.47e), (5.66b), and (5.66c) respectively. By combining these equations with Eq. (5.42a), the TE magnetic field due to an \hat{x} -directed HMD at the origin of the two-layer parallel-plate substrate of Fig. 5.8 can be expressed as follows:

$$\begin{aligned} H_x(\rho, \phi, 0) &= \int_0^\infty F_0(k_\rho) dk_\rho - \cos 2\phi \int_0^\infty F_2(k_\rho) dk_\rho \\ &= \int_0^\infty [(F_0 - F_0^A - F_0^H) + (F_0^A - F_0^H) + 2F_0^H] dk_\rho \\ &\quad - \cos 2\phi \int_0^\infty [(F_2 - F_2^A - F_2^H) + (F_2^A - F_2^H) + 2F_2^H] dk_\rho \\ &= I_{0,1} + I_{0,2} + 2I_0^H - \cos 2\phi (I_{2,1} + I_{2,2} + 2I_2^H) \end{aligned} \quad (5.67a)$$

with

$$I_{0,1} = \int_0^\infty (F_0 - F_0^A - F_0^H) dk_\rho \quad (5.67b)$$



$$I_{0,2} = \int_0^{\infty} (F_0^A - F_0^H) dk_{\rho} \quad (5.67c)$$

$$I_{2,1} = \int_0^{\infty} (F_2 - F_2^A - F_2^H) dk_{\rho} \quad (5.67d)$$

$$I_{2,2} = \int_0^{\infty} (F_2^A - F_2^H) dk_{\rho} \quad (5.67e)$$

Figure 5.19 shows graphs of the various substrate integrands F_0 , F_0^H and F_0^A as well as the difference functions $F_0 - F_0^A - F_0^H$ and $F_0^A - F_0^H$ that are the integrands in Eqs. (5.67b) and (5.67c) respectively. The graphs were calculated at $f = 10$ GHz for $\rho = 20$ mm, $h_1 = 0.813$ mm $= 0.05\lambda_d$, $h_2 = 5$ mm $= \lambda_0/6$, $\epsilon_{r1} = 3.38$, and $\epsilon_{r2} = 1$ (*i.e.*, Substrate I of Section 5.4.2.1 below; ρ is in the vicinity of λ_{CPW} , the wavelength at 10 GHz of a 50 Ω CPW on Substrate I). Figure 5.20 shows the corresponding graphs of F_2 , F_2^H and F_2^A and the difference functions $F_2 - F_2^A - F_2^H$ and $F_2^A - F_2^H$ that are the integrands in Eqs. (5.67d) and (5.67e). Similar graphs for $\rho = 64.5$ mm $= 3\lambda_{CPW}$ are given in Figs. 5.21 and 5.22.

While the integrands F_i , F_i^H and F_i^A where $i = 0$ or 2 are singular in the sense that they increase indefinitely as $k_{\rho} \rightarrow \infty$, the difference functions $F_i - F_i^A - F_i^H$ and $F_i^A - F_i^H$ are decaying oscillating functions for $k_{\rho} > k_1$ that converge relatively quickly (*i.e.*, compared to the Sommerfeld integral tails in the TM case). Hence the integrals $I_{0,1}$, $I_{0,2}$, $I_{2,1}$, and $I_{2,2}$ were repeatedly evaluated with finite but increasing upper bounds $k_{\rho,upper}$ in the manner of the TM Region 3 integrals of Section 5.3.1, until increasing the upper bound further made no significant difference to the answer; a maximum upper bound of $k_{\rho,upper} = 200k_0$ was sufficient. It should be noted that Eq. (5.67a) can be implemented only because closed-form expressions for I_0^H and I_2^H in its third and sixth terms are available (*cf.* Eq. (5.62)).

Since the integrals $I_{0,1}$, $I_{0,2}$, $I_{2,1}$, and $I_{2,2}$ in Eq. (5.67) are functions of ρ only, it is sufficient to evaluate them once for a suitable range of ρ and then store the resulting values in a lookup table from where they can be retrieved and/or interpolated in the course of evaluating Y_{12}^{int} .

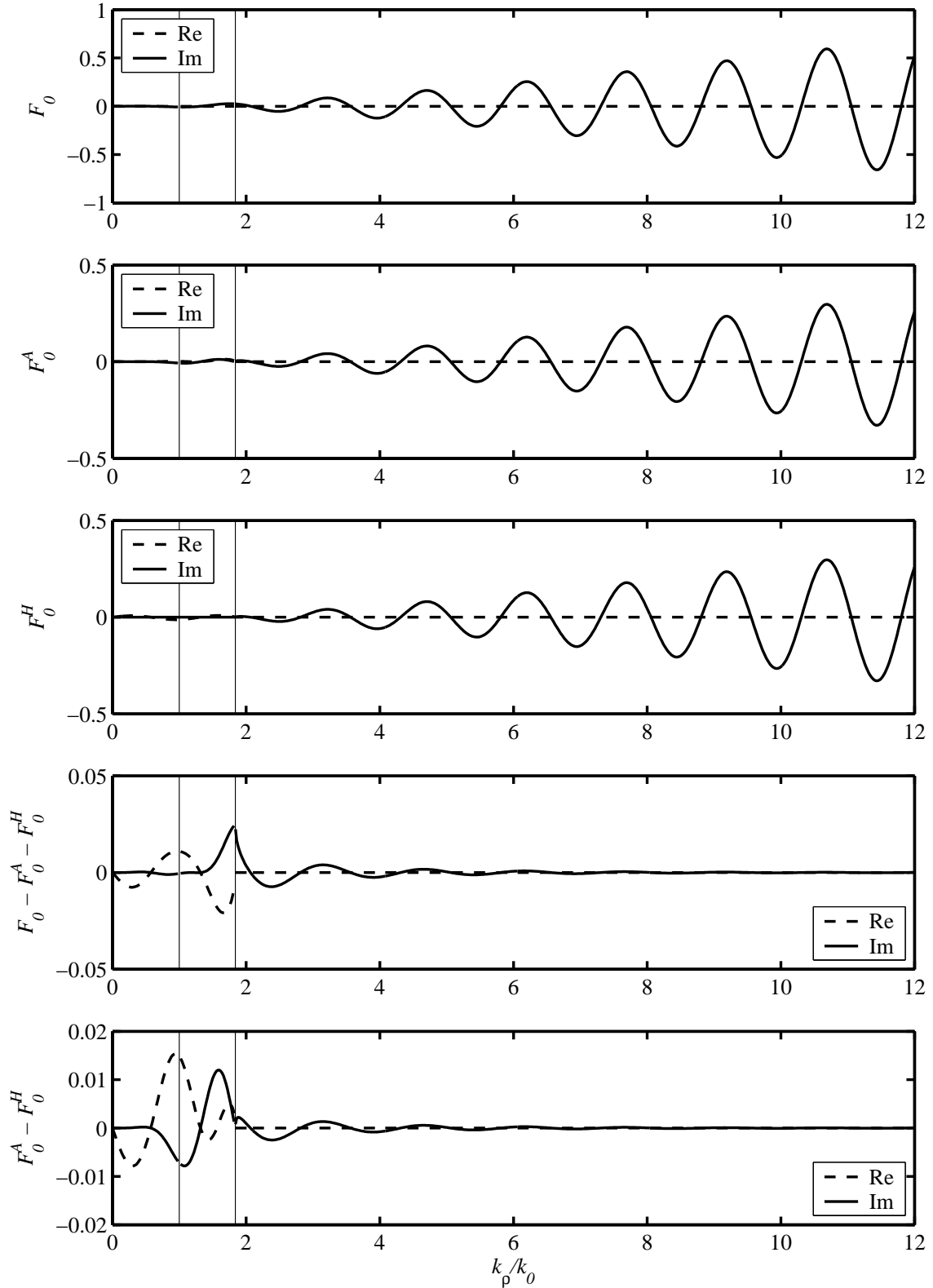


FIGURE 5.19: Plots of the TE integrands $F_0 - F_0^A - F_0^H$ and $F_0^A - F_0^H$, and their constituent functions F_0 , F_0^A , and F_0^H . The vertical lines (from left to right) correspond to $k_\rho = k_2$ and $k_\rho = k_1$ respectively. $f = 10$ GHz, $\rho = 20$ mm, $h_1 = 0.813$ mm $= 0.05\lambda_d$, $h_2 = 5$ mm $= \lambda_0/6$, $\epsilon_{r1} = 3.38$, $\epsilon_{r2} = 1$.

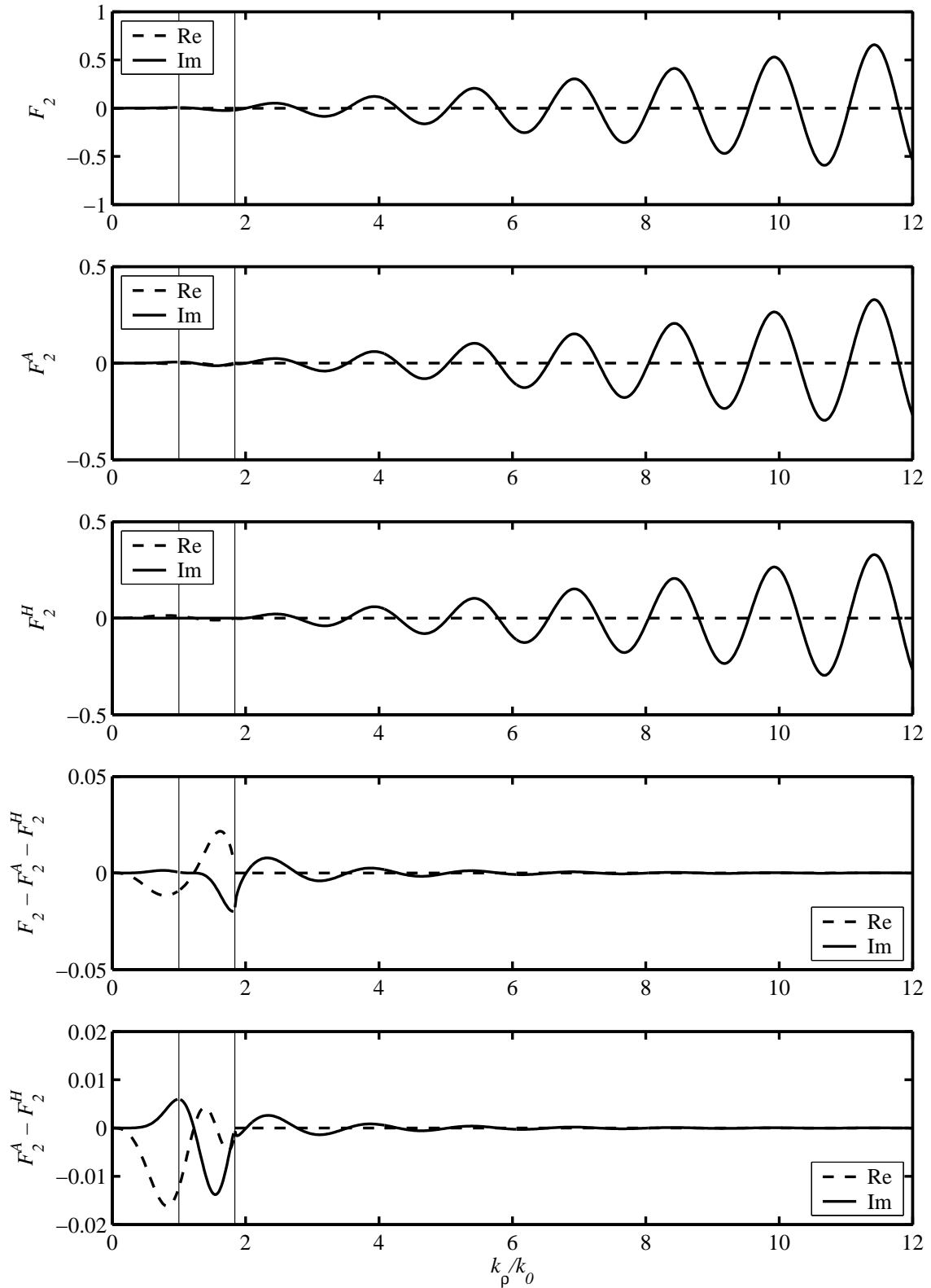


FIGURE 5.20: Plots of the TE integrands $F_2 - F_2^A - F_2^H$ and $F_2^A - F_2^H$, and their constituent functions F_2 , F_2^A , and F_2^H . The vertical lines (from left to right) correspond to $k_\rho = k_2$ and $k_\rho = k_1$ respectively. $f = 10$ GHz, $\rho = 20$ mm, $h_1 = 0.813$ mm $= 0.05\lambda_d$, $h_2 = 5$ mm $= \lambda_0/6$, $\epsilon_{r1} = 3.38$, $\epsilon_{r2} = 1$.

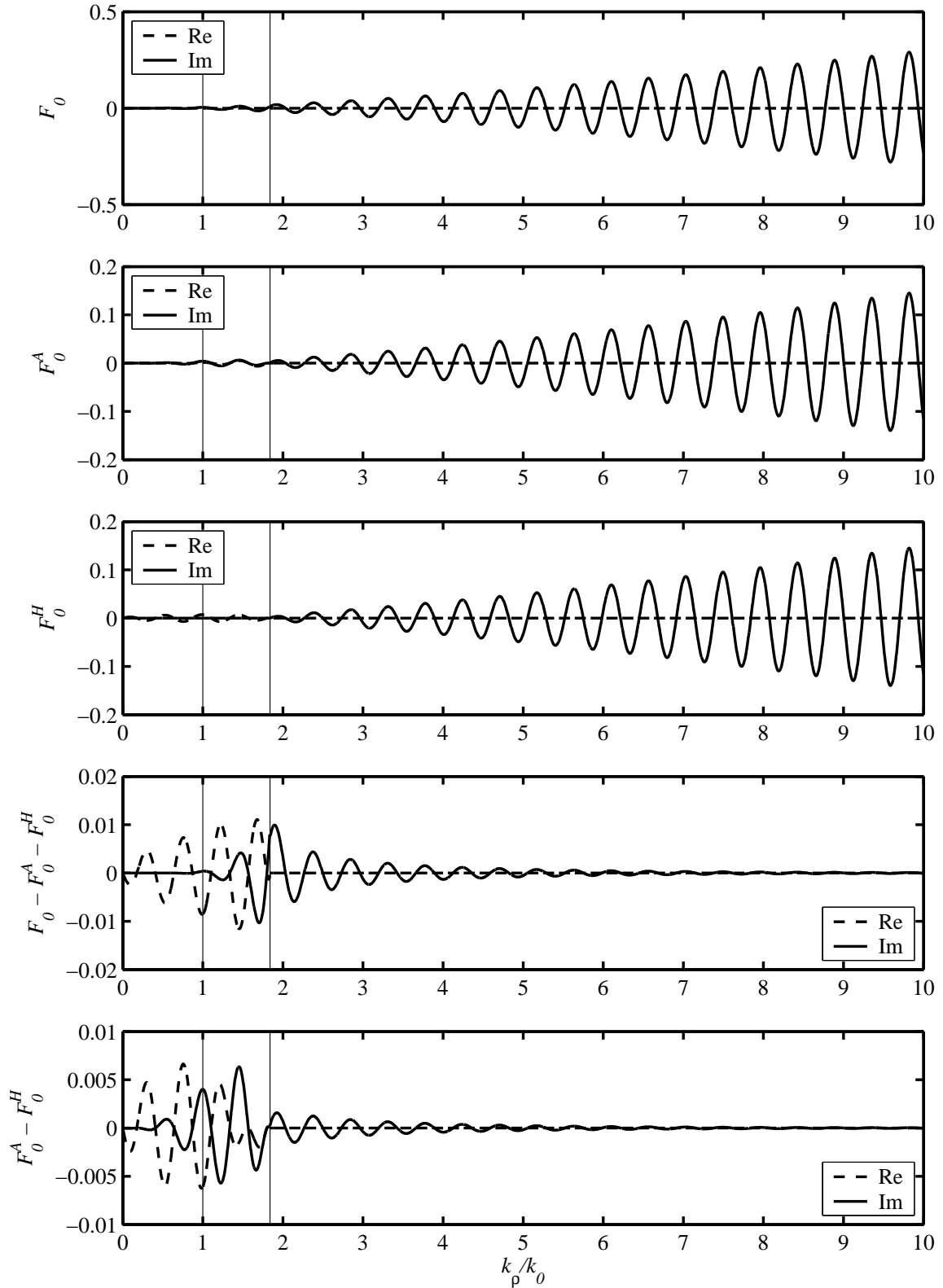


FIGURE 5.21: Plots of the TE integrands $F_0 - F_0^A - F_0^H$ and $F_0^A - F_0^H$, and their constituent functions F_0 , F_0^A , and F_0^H . The vertical lines (from left to right) correspond to $k_\rho = k_2$ and $k_\rho = k_1$ respectively. $f = 10$ GHz, $\rho = 64.5$ mm, $h_1 = 0.813$ mm $= 0.05\lambda_d$, $h_2 = 5$ mm $= \lambda_0/6$, $\epsilon_{r1} = 3.38$, $\epsilon_{r2} = 1$.

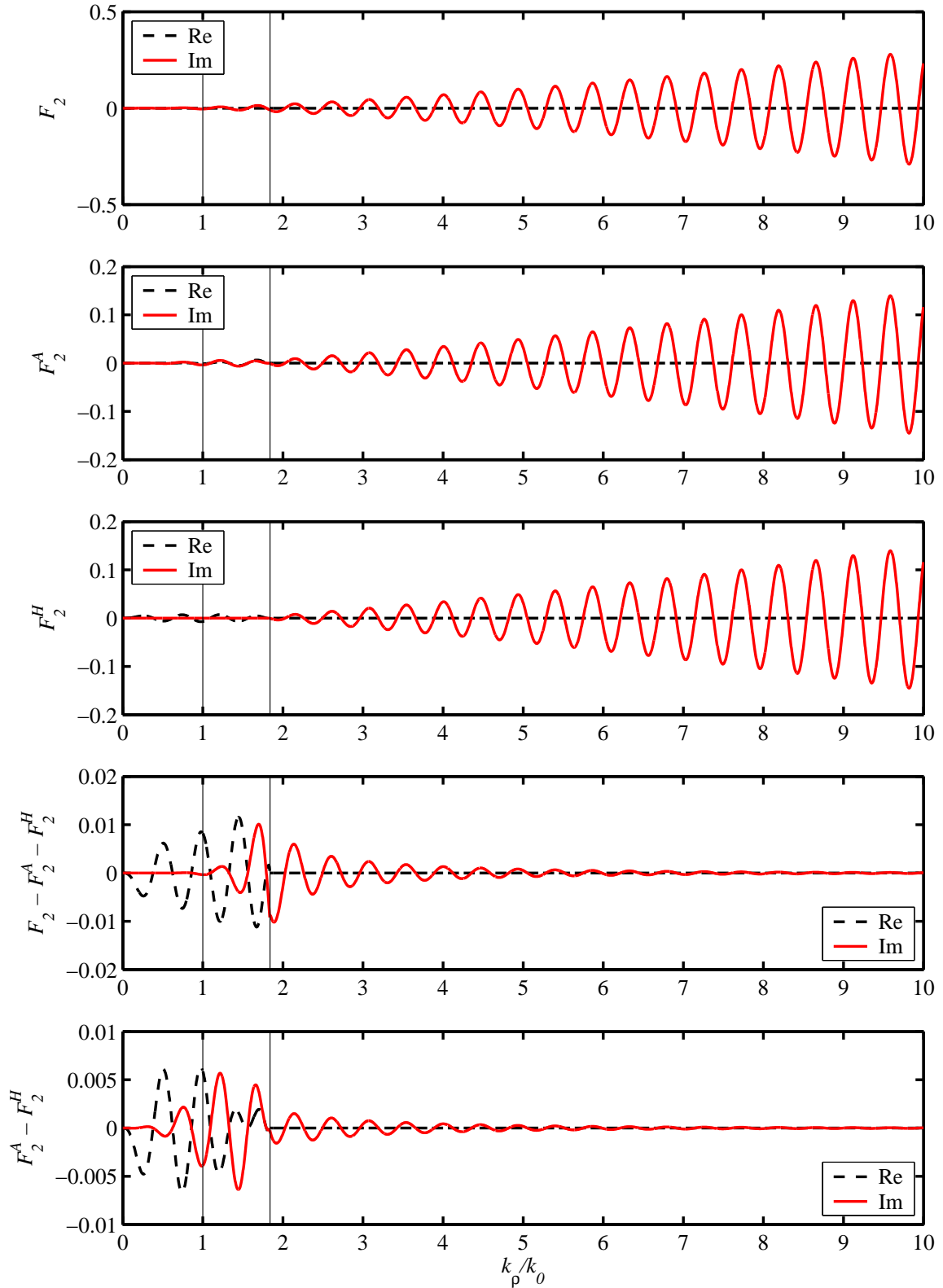


FIGURE 5.22: Plots of the TE integrands $F_2 - F_2^A - F_2^H$ and $F_2^A - F_2^H$, and their constituent functions F_2 , F_2^A , and F_2^H . The vertical lines (from left to right) correspond to $k_\rho = k_2$ and $k_\rho = k_1$ respectively. $f = 10$ GHz, $\rho = 64.5$ mm, $h_1 = 0.813$ mm $= 0.05\lambda_d$, $h_2 = 5$ mm $= \lambda_0/6$, $\epsilon_{r1} = 3.38$, $\epsilon_{r2} = 1$.



5.4 IMPLEMENTATION AND RESULTS

5.4.1 Implementation strategy

The present section gives details of the implementation of the reciprocity-based formulation developed in Section 5.2 for finding the mutual admittance between broadside CPW-fed slots on a two-layer parallel-plate substrate. It is also described how the moment-method-based simulator IE3D was used to generate results against which the reciprocity-formulation results could be compared. The actual computed results are presented in Section 5.4.2.

Mutual admittance Y_{12} as a function of broadside inter-slot distance d was computed at 10 GHz for slots on three substrates, namely

- Substrate I: $h_1 = 0.813 \text{ mm} = 0.05\lambda_d$; $h_2 = 5 \text{ mm} = \lambda_0/6$; $\epsilon_{r1} = 3.38$; $\epsilon_{r2} = 1$
- Substrate II: $h_1 = 1.21 \text{ mm} = 0.1\lambda_d$; $h_2 = 5 \text{ mm} = \lambda_0/6$; $\epsilon_{r1} = 6.15$; $\epsilon_{r2} = 1$
- Substrate III: $h_1 = 0.254 \text{ mm} = 0.013\lambda_d$; $h_2 = 5 \text{ mm} = \lambda_0/6$; $\epsilon_{r1} = 2.2$; $\epsilon_{r2} = 1$

(in the above, λ_d is the wavelength in the top dielectric layer, and λ_0 the free-space wavelength at 10 GHz). Substrate I, the substrate chosen as reference, was used in an earlier successful implementation of an 8-element uniform linear CPW-fed array [36]. Substrates II and III had top dielectric layers that were electrically significantly thicker and thinner, respectively, than that of Substrate I, *i.e.*, $0.1\lambda_d$ and $0.013\lambda_d$ as opposed to $0.05\lambda_d$. All substrates had an air bottom layer with an electric height of $\lambda_0/6$, and allowed for propagation of the TM_0 two-layer parallel-plate mode only.

Also computed was Y_{12} against frequency for a twin slot configuration on Substrate I where all dimensions including d were kept constant. This result was compared with a measurement to be discussed in Section 5.4.2.5.

Details of using IE3D to find Y_{12} against d for two CPW-fed slots on any of the above substrates at 10 GHz were as follows. Using a moment-method-based approach implies that the entire two-slot structure needs to be solved for each instance of d . Ports were defined at the ends of CPW feed lines that were $l_f = \lambda_{CPW}/2$ long; feed lines thus only extended as far as the terminal planes in Fig. 5.5 (λ_{CPW} is the CPW wavelength at 10 GHz). From the full-wave solution, IE3D calculates the two-port admittance matrix, or Y parameters of the structure referred to the above ports (choosing $l_f = \lambda_{CPW}/2$ ensured that Y parameters were referred to the centres of radiating slots). While $Y_{12} = Y_{21}$ was the parameter of interest, the two-port self-admittances $Y_{11} = Y_{22}$ were used in interpreting some of the results presented in Section 5.4.2. (A separation into external and internal

mutual admittances was of course not possible.)

When implementing the reciprocity-expression approach to find Y_{12} against d , each of the two CPW-fed slots were first simulated in isolation using IE3D.¹⁸ The geometry of isolated CPW-fed slot m is shown in Fig. 5.23, where $m = 1$ or 2. The CPW feed line length was $l_f = \lambda_{CPW}/2$. In IE3D, a port was defined at the end of the feed line, which coincided with the terminal voltage reference plane mm' , as noted in Section 5.2.2. Analyzing slot m in IE3D yielded the tangential electric field along the centre of the radiating slot, $\mathbf{E}_{m,slot} = E_{my,slot}\hat{y}$ (the longitudinal centre of the radiating slot coincides with the x axis in Fig. 5.23).¹⁹ A discretization allowing for only one cell across the width of the radiating slot was adopted. This facilitated implementation of the simplifying assumption that the transverse component of the slot field was constant, having its longitudinal centre value across the width of the slot. The analysis also yielded the terminal voltage V_m at terminal plane mm' .

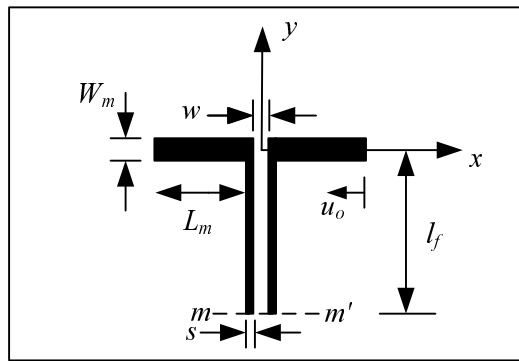


FIGURE 5.23: Top view of isolated CPW-fed slot m , where $m = 1$ or 2. $L_m \equiv$ half-length and $W_m \equiv$ width of radiating slot; $s \equiv$ slot width and $w \equiv$ centre strip width of feed line; $l_f \equiv$ length of feed line; $u_o \equiv$ distance from outer edge.

From the electric fields in the isolated slots, external and internal equivalent magnetic currents M_{1x}^{ext} , M_{2x}^{ext} , M_{1x}^{int} , and M_{2x}^{int} were obtained using Eqs. (5.4), (5.6), (5.10), and (5.11). M_{1x}^{ext} and M_{1x}^{int} are required to find H_{21x}^{ext} and H_{21x}^{int} using Eqs. (5.8a) and (5.13b) respectively. Subsequently, Y_{12}^{ext} and Y_{12}^{int} in Eqs. (5.7) and (5.12) were evaluated for each instance of slot separation d , and the total mutual admittance Y_{12} was found from $Y_{12} = Y_{12}^{ext} + Y_{12}^{int}$. In accordance with the definition of the quantities that constitute Eq. (5.2), M_{1x}^{ext} , M_{2x}^{ext} , M_{1x}^{int} , M_{2x}^{int} , V_1 and V_2 were kept the same for all values of d . The actual implementation of integrals in the preceding equations were done in Matlab using the NAG routine D01FCF [89].

¹⁸ In the case of twin slots, only one slot needed to be simulated.

¹⁹ As noted before, the \hat{x} -component of the field was considered negligible.



Further comment is in order regarding the terminal voltage V_m of an isolated slot m (*cf.* Fig. 5.23; $m = 1$ or 2). Consider first a narrow rectangular slot on an infinite ground plane in free space that is fed at its centre by means of two wires. The aperture tangential electric field can be approximated in an accurate manner by a piecewise sinusoidal function. If the field is assumed constant across the width of the slot, the slot's terminal voltage is readily calculated as the product of the field at the centre of the slot, and the slot width. The calculation procedure does not depend on slot length;²⁰ the terminal voltage is always determined from the field value at the centre of the slot.

An exploratory numerical investigation was carried out to determine whether the terminal voltage of an isolated CPW-fed slot on a two-layer parallel-plate substrate (*i.e.*, the voltage seen at the reference plane mm' in Fig. 5.23) could be determined in a like manner from its radiating slot electric field. First, IE3D was used to design an isolated slot with a width $W = 0.4$ mm on Substrate I to be at its second resonance at 10 GHz; this resulted in a half-length of $L_{res} = 10.87$ mm and a resonant self-impedance of about 14Ω (*cf.* Section 4.2.2). The CPW feed line was $l_f = \lambda_{CPW}/2$ long. Subsequently, IE3D was used to analyze eleven slots that were identical in all respects to the above resonant slot except for their half-lengths L that varied in the range $0.85L_{res} \leq L \leq 1.15L_{res}$ (as before, the moment-method discretization was done such that only one cell was allowed across the radiating slot width.) For each L , the longitudinal tangential electric field in the centre of the slot, as well as the port voltage V_t was recorded; the port was defined at the terminal plane mm' shown in Fig. 5.23 (the IE3D port voltage V_t is the same as the terminal voltage V_m , and includes the effect of the CPW-to-radiating-slot transition). The aim was to find out whether (and where) for a particular slot length a radiating slot voltage could be found that was equal to the (CPW slot) terminal voltage. Here, the radiating slot voltage V_{slot} at a position x in the slot is defined as $V_{slot}(x) = W \cdot E_{y,slot}(x)$, where $E_{y,slot}(x)\hat{y}$ is the slot tangential electric field (the field is assumed constant in the transverse direction). Hence, for each L , a $V_{slot}^o = V_{slot}(x_o)$ was determined, which was the value of $V_{slot}(x)$ closest to the terminal voltage V_t out of all possible $V_{slot}(x)$ (V_{slot}^o was located at $x = x_o$).

In Table 5.1, the position of V_{slot}^o , expressed as normalized distance from the radiating slot outer edge u_o/L (see Fig. 5.23), is listed against L/L_{res} . Two measures pertaining to the closeness between V_{slot}^o and V_t is also given. These reveal a generally close correspondence between V_{slot}^o and V_t ; the biggest difference in magnitude occurred for $L = L_{res}$, where $|V_{slot}^o|$ was about 7% smaller than $|V_t|$. If the right half of the CPW-fed slot of Fig. 5.23 is considered, the position where V_{slot}^o must be “read off” coincides with the boundary between the CPW slot and radiating slot for all L . The implication is that, if the reciprocity-based expressions are intended to be used in an array design algorithm requiring multiple evaluations, it will be straightforward to establish terminal voltages once

²⁰ Center-fed slots in an infinite ground plane are normally assumed to operate around their first resonant lengths.



slot electric fields are known. Slot field information can be obtained at the same time lookup tables for the self-admittances of isolated slots are compiled via moment-method-based calculations (*e.g.*, [19,35]). Alternatively, only the complex amplitude of the slot field (as opposed to the complete field distribution) can be obtained from the isolated slot analysis, and then used to scale generic functions that approximate the slot field; for example, it is relatively simple to relate piecewise sinusoidal functions to slot field magnitudes.

TABLE 5.1: Position in slot of radiating slot voltage closest to terminal voltage for various slot half-lengths, and difference between radiating slot voltage and terminal voltage. u_o is distance from the radiating slot outer edge. $W = 0.4$ mm; $h_1 = 0.813$ mm; $h_2 = 5$ mm; $\epsilon_{r1} = 3.38$; $\epsilon_{r2} = 1$.

$\frac{L}{L_{res}}$	$\frac{u_o}{L}$	$\frac{ V_{slot} - V_t }{ V_t }$ (%)	$\angle(V_{slot}) - \angle(V_t)$ (deg.)
0.85	1.00	3.7	-3.9
0.88	1.00	2.1	-4.2
0.91	1.00	-0.2	-4.3
0.94	1.00	-3.2	-3.7
0.97	1.00	-6.5	-1.8
1.00	1.00	-7.4	0.0
1.03	1.00	-5.9	1.7
1.06	0.99	-3.5	2.3
1.09	0.99	-1.6	2.1
1.12	0.99	-2.1	1.1
1.15	0.99	-1.2	0.8

5.4.2 Results

In this section, results are presented for the computation of Y_{12} against d for slots on Substrates I, II, and III (Sections 5.4.2.1, 5.4.2.2 and 5.4.2.3), and for Y_{12} against frequency for twin slots with a fixed spacing on Substrate I (Section 5.4.2.5). In all cases, results obtained using the reciprocity-expression approach are compared to moment-method-based results computed using IE3D.

5.4.2.1 Substrate I: $h_1 = 0.05\lambda_d$, $h_2 = \lambda_0/6$, $\epsilon_{r1} = 3.38$, $\epsilon_{r2} = 1$

A 50 Ω CPW feed line was designed on this substrate in IE3D with $w = 3.7$ mm and $s = 0.2$ mm (*cf.* Section 4.2.2). Subsequently, an isolated CPW-fed slot with a width W of 0.4 mm was designed to operate at its second resonance at 10 GHz, resulting in a half-length $L = L_{res} = 10.87$ mm and a



resonant self-impedance of about 14Ω .

Mutual admittance Y_{12} against distance d with $0.9\lambda_{CPW} \leq d \leq 3\lambda_{CPW}$ was computed for four pairs of identical broadside slots, *i.e.*, twin slots, based on the above slot (λ_{CPW} is the CPW wavelength at 10 GHz). While all four pairs had $W_1 = W_2 = 0.4$ mm, their half-lengths $L_1 = L_2$ were $0.85L_{res}$, $0.95L_{res}$, L_{res} , and $1.1L_{res}$.²¹ In all cases, feed line lengths were $l_f = 0.5\lambda_{CPW}$.

The real and imaginary parts of the mutual admittance Y_{12} against normalized broadside distance d/λ_{CPW} for twin slots with $L_1 = L_2 = 0.85L_{res} = 9.24$ mm are shown in Fig. 5.24; results from both the reciprocity-expression approach and IE3D are represented. Likewise, Y_{12} for twin slots with $L_1 = L_2 = 0.95L_{res} = 10.33$ mm, $L_1 = L_2 = L_{res} = 10.87$ mm, and $L_1 = L_2 = 1.1L_{res} = 11.96$ mm are shown in Figs. 5.25, 5.26, and 5.29 respectively. For the case $L_1 = L_2 = L_{res}$, Figs. 5.27 and 5.28 show the magnitude and phase of Y_{12} against d/λ_{CPW} .

Figs. 5.24–5.29 reveal close agreement between Y_{12} computed using the reciprocity-expression approach, and IE3D. Agreement is very good for twin slots with half-lengths $L = 0.85L_{res}$, and somewhat less so for the cases $L_1 = L_2 = 0.95L_{res}$, $1.1L_{res}$, and L_{res} in order of decreasing goodness of agreement. Especially in the case $L_1 = L_2 = L_{res}$, IE3D curves seem visually “irregular” in the sense that each appears like a version of the corresponding curve from the reciprocity-expression approach with some oscillation superimposed (*cf.* Figs. 5.26 and 5.27)²² – this is true to a lesser extent of the cases $L = 1.1L_{res}$ and $L = 0.95L_{res}$.

In order to investigate the above differences further, two-port self-admittances $Y_{11} = Y_{22}$ calculated by IE3D were considered in conjunction with the Y_{12} curves of Figs. 5.24–5.29. Fig. 5.30 shows the real and imaginary parts of the two-port self-admittance Y_{11} against broadside distance d/λ_{CPW} for the case $L_1 = L_2 = L_{res}$ at 10 GHz. The (resonant) self-admittance of the corresponding isolated slot, $Y_{self} = 72$ mS computed using IE3D is also shown; it can be seen that Y_{11} takes the form of a decaying oscillation about Y_{self} . Fig. 5.31 displays the magnitude of Y_{11} against d/λ_{CPW} , as well as $|Y_{self}|$; Fig. 5.32 gives the corresponding phases. As d increases, Y_{11} approaches Y_{self} , as expected. Similarly, Fig. 5.33 shows $|Y_{11}|$ against d/λ_{CPW} for the case $L_1 = L_2 = 0.85L_{res}$, and $|Y_{self}|$ for an isolated $0.85L_{res}$ slot, which has $Y_{self} = 29.2\angle 52^\circ$ mS (again computed using IE3D); corresponding phases are given in Fig. 5.34. Magnitude and phase curves for the case $L_1 = L_2 = 1.1L_{res}$ are presented in Figs. 5.35 and Fig. 5.36. For an isolated $1.1L_{res}$ slot, $Y_{self} = 50.5\angle -53.7^\circ$ mS.

²¹ Only broadside slots were investigated as this is the configuration relevant to series-fed linear array designs [35, 36].

²² This was noted previously in Section 4.2.3.

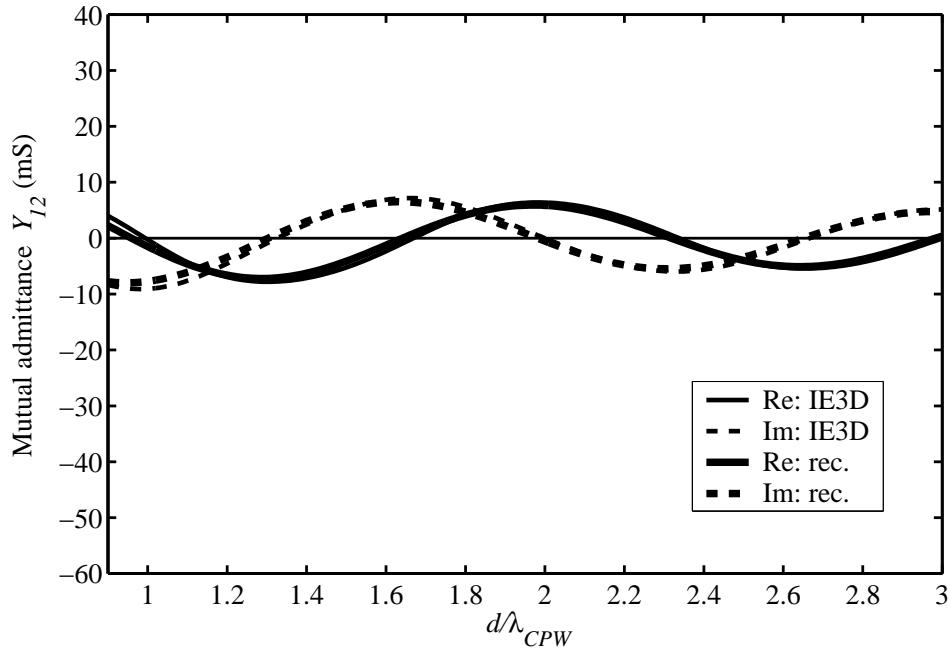


FIGURE 5.24: Mutual admittance Y_{12} against broadside distance d/λ_{CPW} at 10 GHz for CPW-fed twin slots with $L_1 = L_2 = 0.85L_{res} = 9.24$ mm on Substrate I. $W_1 = W_2 = 0.4$ mm; $h_1 = 0.813$ mm; $h_2 = 5$ mm; $\epsilon_{r1} = 3.38$; $\epsilon_{r2} = 1$; $l_f = 0.5\lambda_{CPW}$. (rec.: computed using reciprocity-expression approach.)

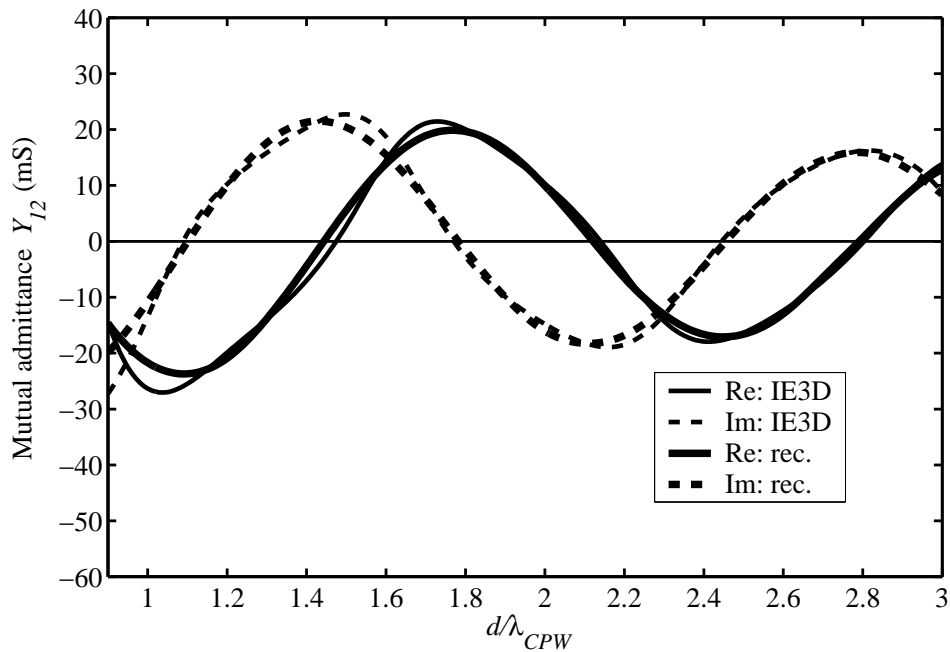


FIGURE 5.25: Mutual admittance Y_{12} against broadside distance d/λ_{CPW} at 10 GHz for CPW-fed twin slots with $L_1 = L_2 = 0.95L_{res} = 10.33$ mm on Substrate I. $W_1 = W_2 = 0.4$ mm; $h_1 = 0.813$ mm; $h_2 = 5$ mm; $\epsilon_{r1} = 3.38$; $\epsilon_{r2} = 1$; $l_f = 0.5\lambda_{CPW}$.

In accordance with Eq. (5.2), the reciprocity-expression approach utilizes magnetic currents

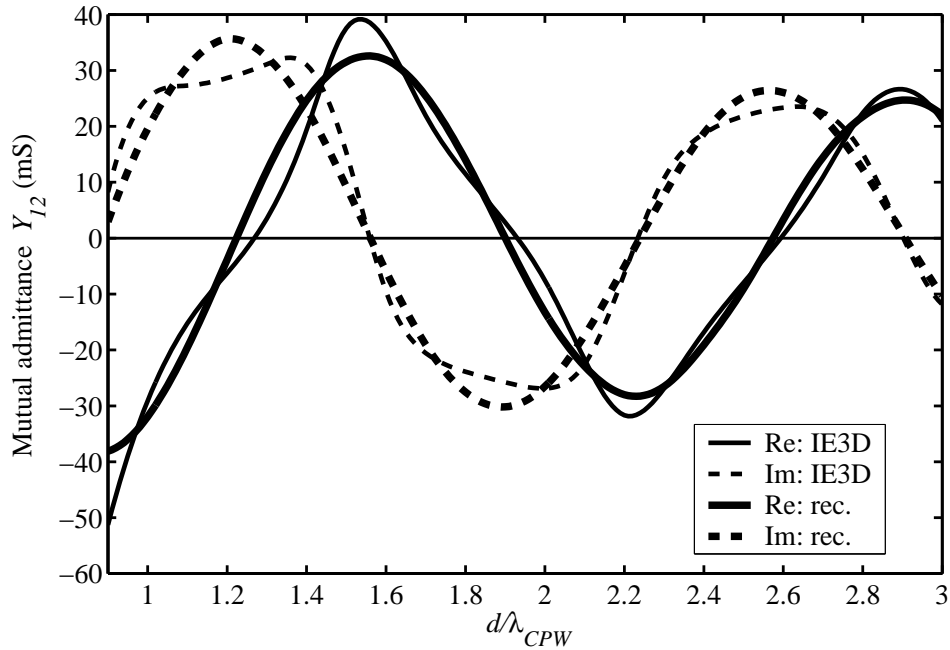


FIGURE 5.26: Mutual admittance Y_{12} against broadside distance d/λ_{CPW} at 10 GHz for CPW-fed twin slots with $L_1 = L_2 = L_{res} = 10.87$ mm on Substrate I. $W_1 = W_2 = 0.4$ mm; $h_1 = 0.813$ mm; $h_2 = 5$ mm; $\epsilon_{r1} = 3.38$; $\epsilon_{r2} = 1$; $l_f = 0.5\lambda_{CPW}$.

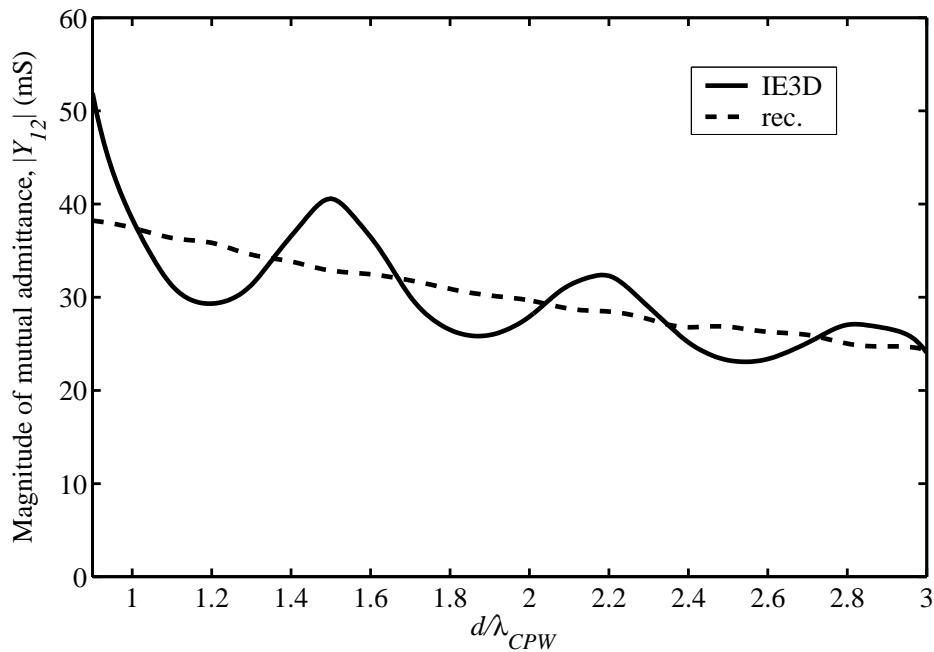


FIGURE 5.27: Magnitude of mutual admittance Y_{12} against broadside distance d/λ_{CPW} at 10 GHz for CPW-fed twin slots with $L_1 = L_2 = L_{res} = 10.87$ mm on Substrate I. $W_1 = W_2 = 0.4$ mm; $h_1 = 0.813$ mm; $h_2 = 5$ mm; $\epsilon_{r1} = 3.38$; $\epsilon_{r2} = 1$; $l_f = 0.5\lambda_{CPW}$.

associated with slots radiating in isolation, *i.e.*, impressed currents; the underlying assumption is that slot self-admittances do not change with d . The two-port self-admittances computed by IE3D,

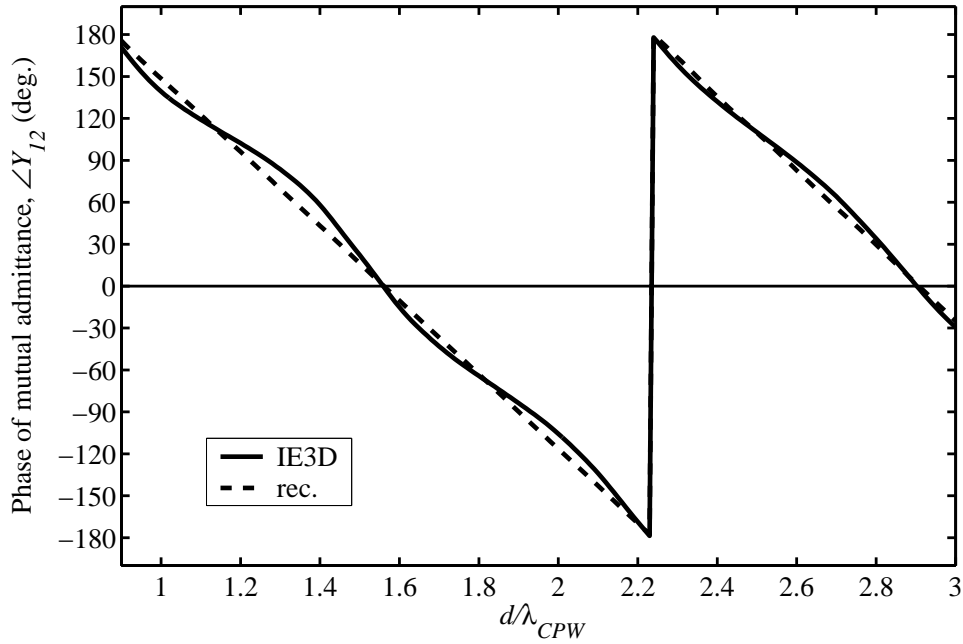


FIGURE 5.28: Phase of mutual admittance Y_{12} against broadside distance d/λ_{CPW} at 10 GHz for CPW-fed twin slots with $L_1 = L_2 = L_{res} = 10.87$ mm on Substrate I. $W_1 = W_2 = 0.4$ mm; $h_1 = 0.813$ mm; $h_2 = 5$ mm; $\epsilon_{r1} = 3.38$; $\epsilon_{r2} = 1$; $l_f = 0.5\lambda_{CPW}$.

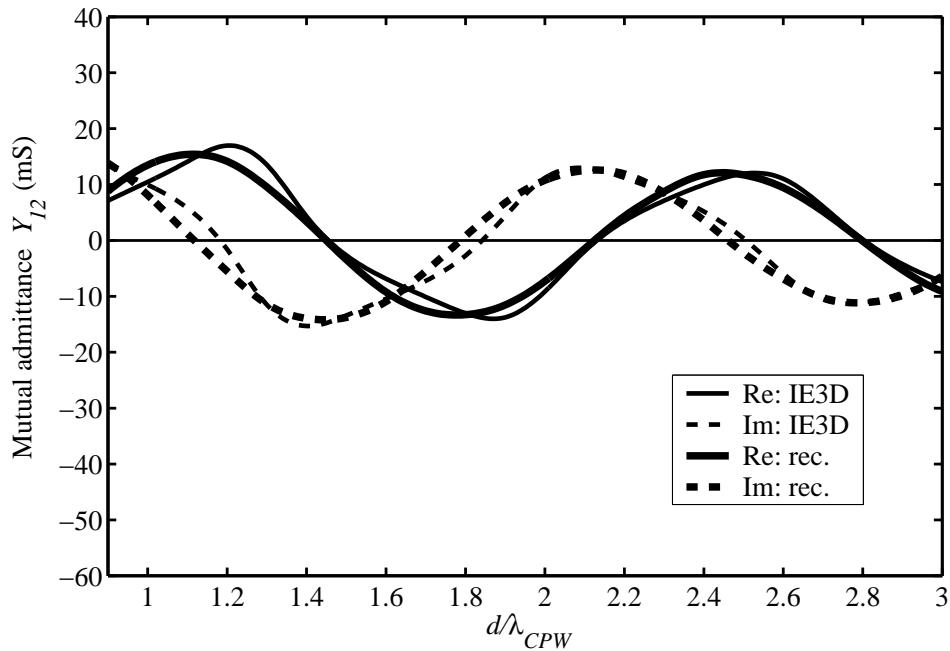


FIGURE 5.29: Mutual admittance Y_{12} against broadside distance d/λ_{CPW} at 10 GHz for CPW-fed twin slots with $L_1 = L_2 = 1.1L_{res} = 11.96$ mm on Substrate I. $W_1 = W_2 = 0.4$ mm; $h_1 = 0.813$ mm; $h_2 = 5$ mm; $\epsilon_{r1} = 3.38$; $\epsilon_{r2} = 1$; $l_f = 0.5\lambda_{CPW}$.

however, appear to oscillate about the self-admittances of the isolated slots. This is most marked for the case $L_1 = L_2 = L_{res}$ as seen in the magnitude plot of Fig. 5.31, and (considerably) less so



for the cases $L_1 = L_2 = 0.85L_{res}$ and $L_1 = L_2 = 1.1L_{res}$ in Figs. 5.33 and 5.35 respectively. The extent of the oscillations are mirrored by the extent of the apparent “superimposed oscillations” of the IE3D Y_{12} curves: it is the most marked for the case $L_1 = L_2 = L_{res}$, and least significant for $L_1 = L_2 = 0.85L_{res}$; furthermore, $|Y_{11}|$ and $|Y_{12}|$ oscillations appear to be synchronized (*e.g.*, Figs. 5.31 and 5.27). Hence discrepancies between IE3D and the reciprocity-expression approach for Y_{12} can be related to different accounts for slot self-admittances in the two models.

In order to subject the reciprocity-expression approach to further verification, the mutual admittance between two pairs of non-identical slots were computed. Fig. 5.37 shows the real and imaginary parts of Y_{12} for the first pair, which had $L_1 = 0.85L_{res}$, $L_2 = 1.1L_{res}$, and $W_1 = W_2 = 0.4$ mm. The second pair had $L_1 = 0.85L_{res}$, $L_2 = L_{res}$, and $W_1 = W_2 = 0.4$ mm; these results are displayed in Fig. 5.38. Good agreement is observed between results obtained using the reciprocity-expression approach and IE3D.

The reciprocity-expression approach can be used to form an estimate of the relative contributions of external and internal mutual admittances to the total mutual admittance; the external and internal admittances can be expressed as $Y_{12}^{ext} = G_{12}^{ext} + jB_{12}^{ext}$ and $Y_{12}^{int} = G_{12}^{int} + jB_{12}^{int}$. Fig. 5.39(a)–(d) show Y_{12}^{ext} and Y_{12}^{int} for each of the cases $L_1 = L_2 = 0.85L_{res}$, $0.95L_{res}$, L_{res} , and $1.1L_{res}$. It is clear that the internal mutual admittance predominates. Fig. 5.40 shows the magnitudes of Y_{12}^{ext} and Y_{12}^{int} for the above cases on one graph. For each of the four half-lengths, the magnitude of the internal mutual admittance starts out at about 2.6 times the magnitude of the external mutual admittance. At the end of the range of d/λ_{CPW} , $|Y_{12}^{int}|$ is about five times the value of $|Y_{12}^{ext}|$. This is not unexpected since $|Y_{12}^{int}|$ is determined by guided fields, unlike $|Y_{12}^{ext}|$.

5.4.2.2 Substrate II: $h_1 = 0.1\lambda_d$, $h_2 = \lambda_0/6$, $\epsilon_{r1} = 6.15$, $\epsilon_{r2} = 1$

The top layer of Substrate II has the greatest electrical thickness of the three substrates, namely $0.1\lambda_d$ compared to $0.05\lambda_d$ of Substrate I and $0.013\lambda_d$ of Substrate II. It is included here for purposes of verification of the reciprocity-expression approach, and would not be a substrate of choice for antenna applications over Substrates I and III that have lower effective dielectric permittivities and hence greater radiation efficiency (*cf.* Chapters 2 and 3). The procedure for presentation and organization of results essentially follows that of the previous section. A 50Ω CPW feed line was designed on Substrate II with $w = 0.68$ mm and $s = 0.15$ mm. Next, an isolated CPW-fed radiating slot with a width W of 0.7 mm was designed to operate at its second resonance at 10 GHz by adjusting its half-length to $L = L_{res} = 7.77$ mm; its resonant self-impedance was about 10Ω .

The real and imaginary parts of the mutual admittance Y_{12} against normalized broadside

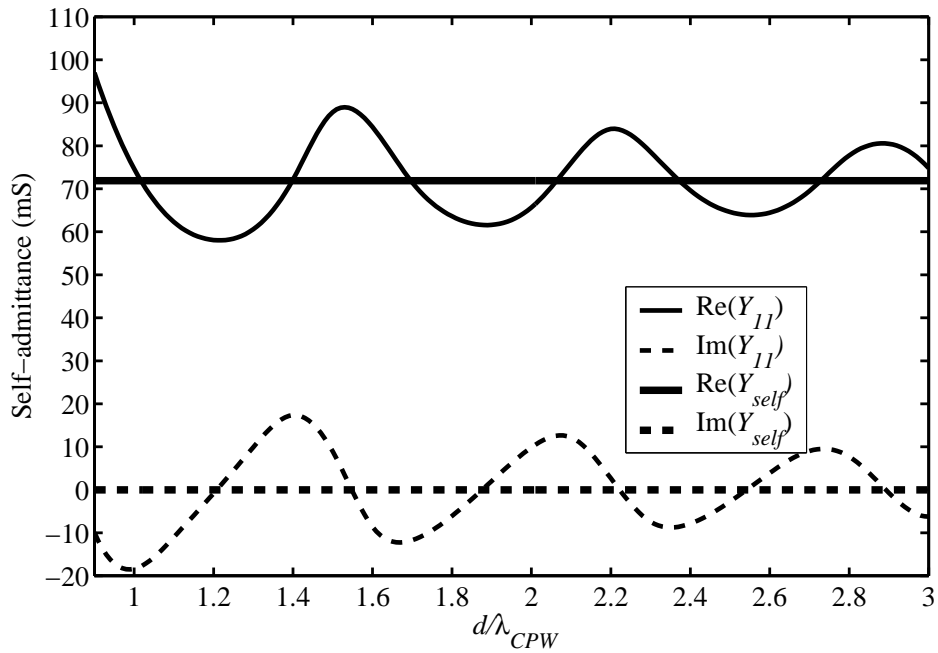


FIGURE 5.30: Two-port self-admittance Y_{11} against broadside distance d/λ_{CPW} for CPW-fed twin slots with $L_1 = L_2 = L_{res} = 10.87$ mm on Substrate I, and resonant isolated self-admittance Y_{self} (both computed at 10 GHz with IE3D). $W_1 = W_2 = 0.4$ mm; $h_1 = 0.813$ mm; $h_2 = 5$ mm; $\epsilon_{r1} = 3.38$; $\epsilon_{r2} = 1$; $l_f = 0.5\lambda_{CPW}$.

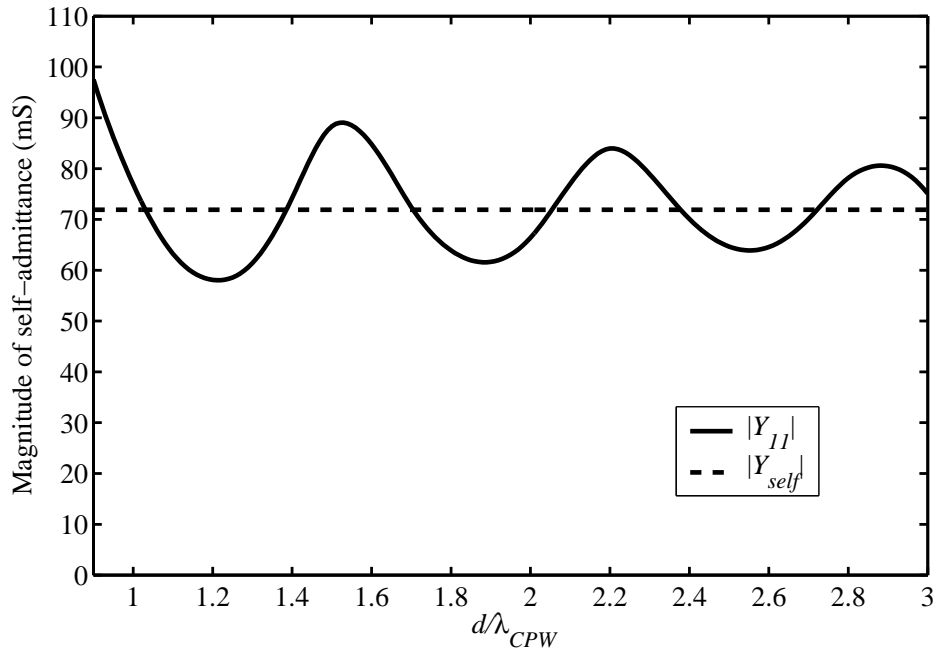


FIGURE 5.31: Magnitude of two-port self-admittance Y_{11} against broadside distance d/λ_{CPW} for CPW-fed twin slots with $L_1 = L_2 = L_{res} = 10.87$ mm on Substrate I, and magnitude of resonant isolated self-admittance Y_{self} (both computed at 10 GHz with IE3D). $W_1 = W_2 = 0.4$ mm; $h_1 = 0.813$ mm; $h_2 = 5$ mm; $\epsilon_{r1} = 3.38$; $\epsilon_{r2} = 1$; $l_f = 0.5\lambda_{CPW}$.

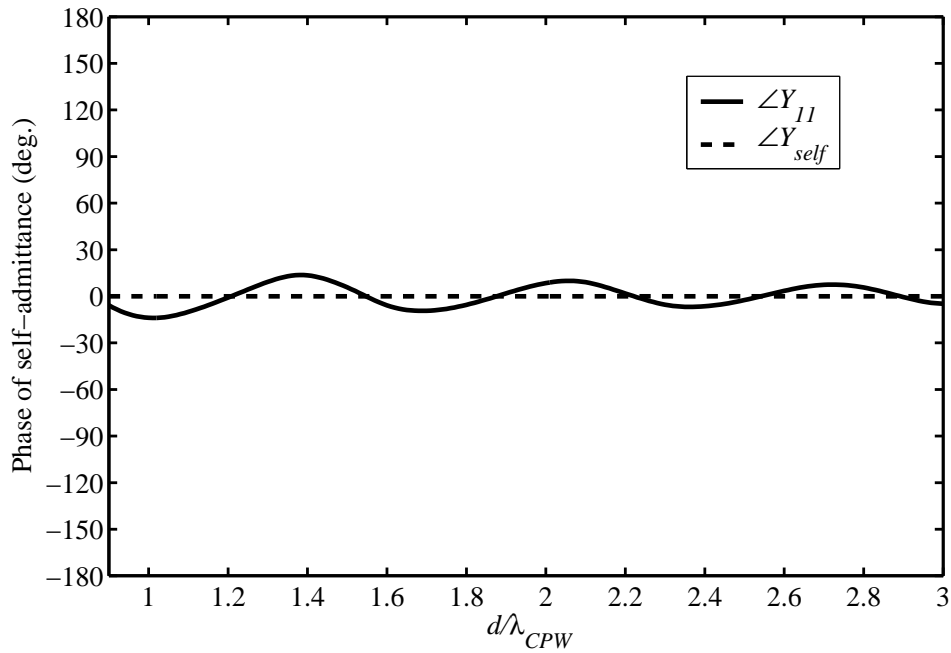


FIGURE 5.32: Phase of two-port self-admittance Y_{11} against broadside distance d/λ_{CPW} for CPW-fed twin slots with $L_1 = L_2 = L_{res} = 10.87$ mm on Substrate I, and phase of resonant isolated self-admittance Y_{self} (both computed at 10 GHz with IE3D). $W_1 = W_2 = 0.4$ mm; $h_1 = 0.813$ mm; $h_2 = 5$ mm; $\epsilon_{r1} = 3.38$; $\epsilon_{r2} = 1$; $l_f = 0.5\lambda_{CPW}$.

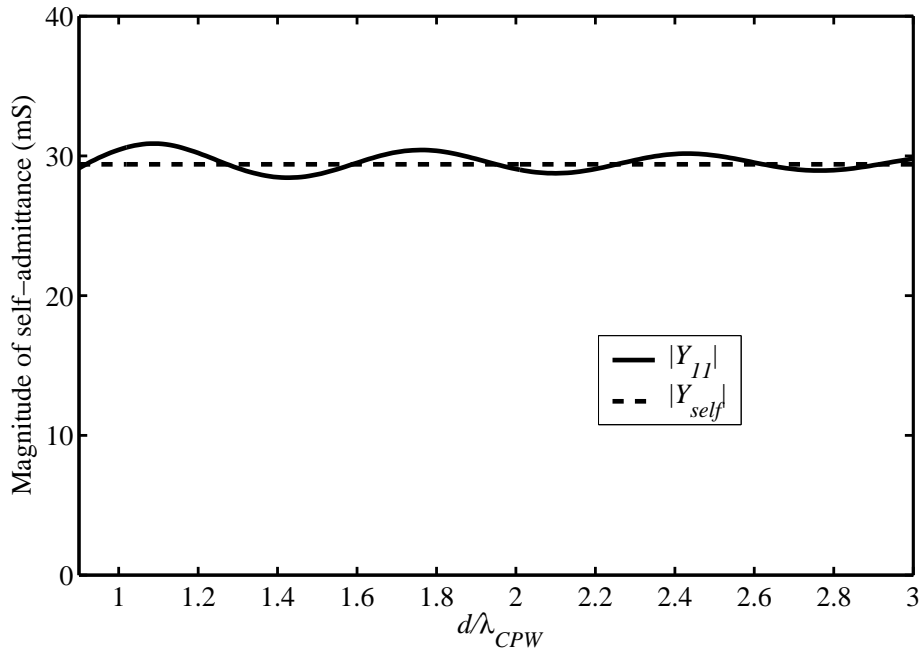


FIGURE 5.33: Magnitude of two-port self-admittance Y_{11} against broadside distance d/λ_{CPW} for CPW-fed twin slots with $L_1 = L_2 = 0.85L_{res} = 9.24$ mm on Substrate I, and magnitude of resonant isolated self-admittance Y_{self} (both computed at 10 GHz with IE3D). $W_1 = W_2 = 0.4$ mm; $h_1 = 0.813$ mm; $h_2 = 5$ mm; $\epsilon_{r1} = 3.38$; $\epsilon_{r2} = 1$; $l_f = 0.5\lambda_{CPW}$.

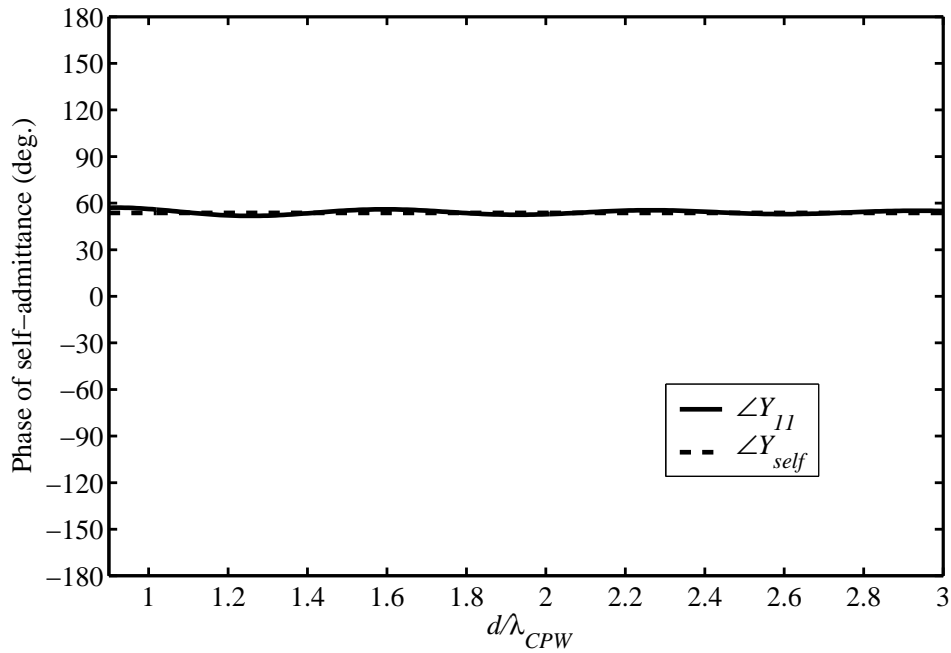


FIGURE 5.34: Phase of two-port self-admittance Y_{11} against broadside distance d/λ_{CPW} for CPW-fed twin slots with $L_1 = L_2 = 0.85L_{res} = 9.24$ mm on Substrate I, and phase of resonant isolated self-admittance Y_{self} (both computed at 10 GHz with IE3D). $W_1 = W_2 = 0.4$ mm; $h_1 = 0.813$ mm; $h_2 = 5$ mm; $\epsilon_{r1} = 3.38$; $\epsilon_{r2} = 1$; $l_f = 0.5\lambda_{CPW}$.

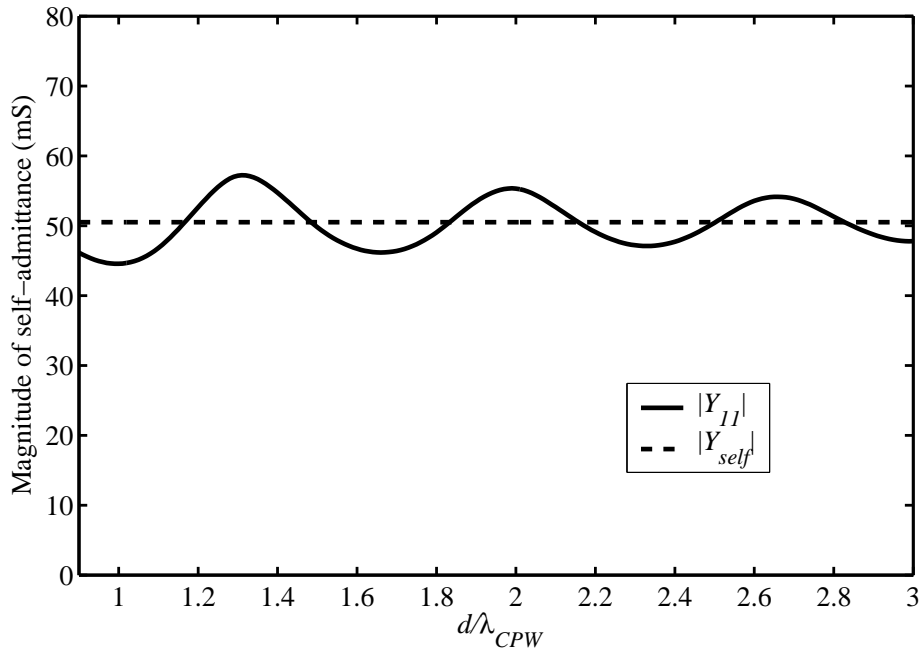


FIGURE 5.35: Magnitude of two-port self-admittance Y_{11} against broadside distance d/λ_{CPW} for CPW-fed twin slots with $L_1 = L_2 = 1.1L_{res} = 11.96$ mm on Substrate I, and magnitude of resonant isolated self-admittance Y_{self} (both computed at 10 GHz with IE3D). $W_1 = W_2 = 0.4$ mm; $h_1 = 0.813$ mm; $h_2 = 5$ mm; $\epsilon_{r1} = 3.38$; $\epsilon_{r2} = 1$; $l_f = 0.5\lambda_{CPW}$.

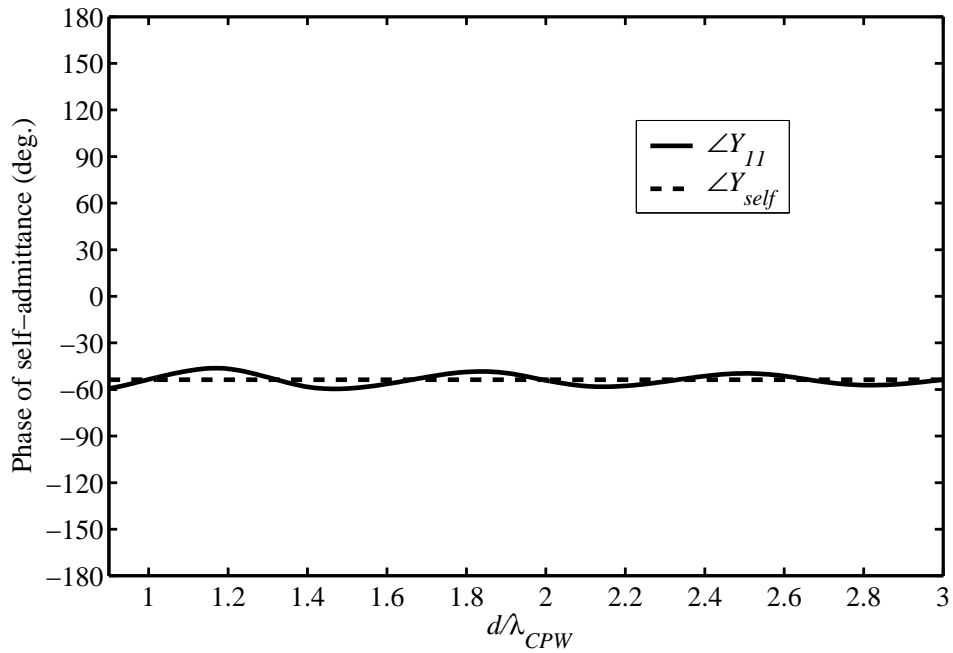


FIGURE 5.36: Phase of two-port self-admittance Y_{11} against broadside distance d/λ_{CPW} for CPW-fed twin slots with $L_1 = L_2 = 1.1L_{res} = 11.96$ mm on Substrate I, and phase of resonant isolated self-admittance Y_{self} (both computed at 10 GHz with IE3D). $W_1 = W_2 = 0.4$ mm; $h_1 = 0.813$ mm; $h_2 = 5$ mm; $\epsilon_{r1} = 3.38$; $\epsilon_{r2} = 1$; $l_f = 0.5\lambda_{CPW}$.

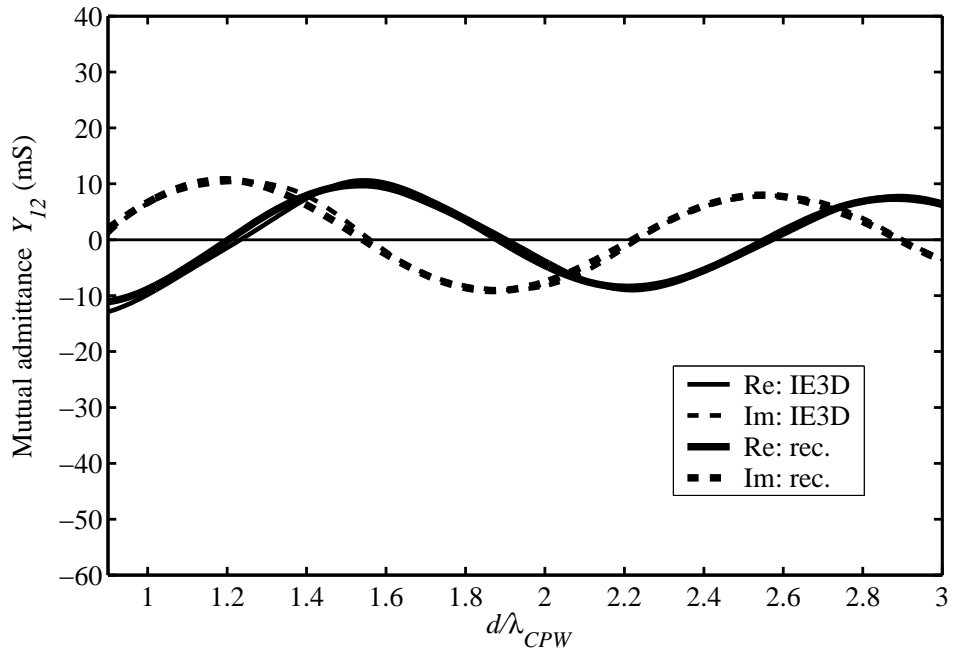


FIGURE 5.37: Mutual admittance Y_{12} against broadside distance d/λ_{CPW} at 10 GHz for *non-identical* CPW-fed broadside slots with $L_1 = 0.85L_{res} = 9.24$ mm and $L_2 = 1.1L_{res} = 11.96$ mm on Substrate I. $W_1 = W_2 = 0.4$ mm; $h_1 = 0.813$ mm; $h_2 = 5$ mm; $\epsilon_{r1} = 3.38$; $\epsilon_{r2} = 1$; $l_f = 0.5\lambda_{CPW}$.

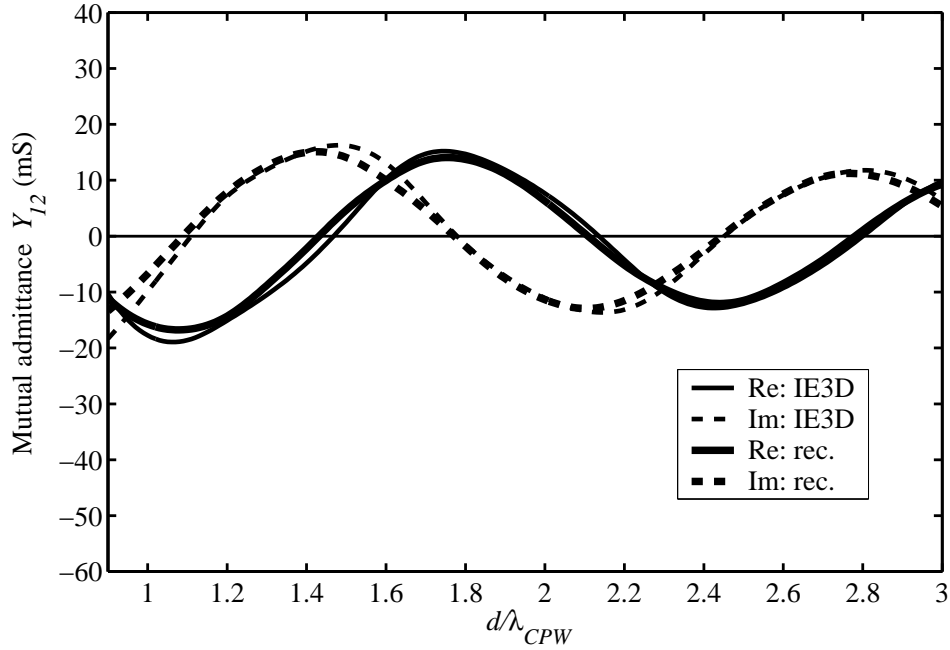


FIGURE 5.38: Mutual admittance Y_{12} against broadside distance d/λ_{CPW} at 10 GHz for *non-identical* CPW-fed broadside slots with $L_1 = 0.85L_{res} = 9.24$ mm and $L_2 = L_{res} = 10.87$ mm on Substrate I. $W_1 = W_2 = 0.4$ mm; $h_1 = 0.813$ mm; $h_2 = 5$ mm; $\epsilon_{r1} = 3.38$; $\epsilon_{r2} = 1$; $l_f = 0.5\lambda_{CPW}$.

distance d/λ_{CPW} for twin slots with $L_1 = L_2 = 0.9L_{res} = 6.99$ mm computed using the reciprocity-expression approach and IE3D are shown in Fig. 5.41. Likewise, Y_{12} against d/λ_{CPW} for twin slots with $L_1 = L_2 = L_{res} = 7.77$ mm, and $L_1 = L_2 = 1.1L_{res} = 8.55$ mm are shown in Figs. 5.42 and 5.45 respectively. For the case $L_1 = L_2 = L_{res}$, Fig. 5.43 shows the magnitude of Y_{12} against d/λ_{CPW} , and Fig. 5.44 the phase. Feed line lengths were $l_f = 0.5\lambda_{CPW}$ throughout.

Figs. 5.41–5.45 shows a similar pattern of agreement between Y_{12} computed using the reciprocity expression and IE3D as in the case of Substrate I: agreement is best for the shortest twin slots, while for the L_{res} twin slots IE3D curves seem irregular when compared to the reciprocity-expression curves in a manner similar to that observed for L_{res} twin slots on Substrate I. However, in the case of Substrate II the irregularity seems more marked. In order to investigate this further, two-port self-admittances $Y_{11}(= Y_{22})$ calculated using IE3D were considered in conjunction with the Y_{12} curves of Figs. 5.41–5.45. Fig. 5.46 shows the real and imaginary parts of the two-port self-admittance Y_{11} against broadside distance d/λ_{CPW} for the case $L_1 = L_2 = L_{res}$ at 10 GHz. Fig. 5.47 shows the magnitude of Y_{11} against d/λ_{CPW} , as well as the magnitude of the resonant isolated self-admittance, $Y_{self} = 100$ mS, computed using IE3D as described earlier; Fig. 5.48 gives the corresponding phases. Similarly, Fig. 5.49 shows $|Y_{11}|$ against d/λ_{CPW} for the case $L_1 = L_2 = 0.9L_{res}$, and $|Y_{self}|$ for an isolated $0.9L_{res}$ slot, which has $Y_{self} = 45.4\angle 53^\circ$ mS; corresponding phases are given in Fig. 5.50. Magnitude and phase curves for the case $L_1 = L_2 = 1.1L_{res}$ are presented in Figs. 5.51

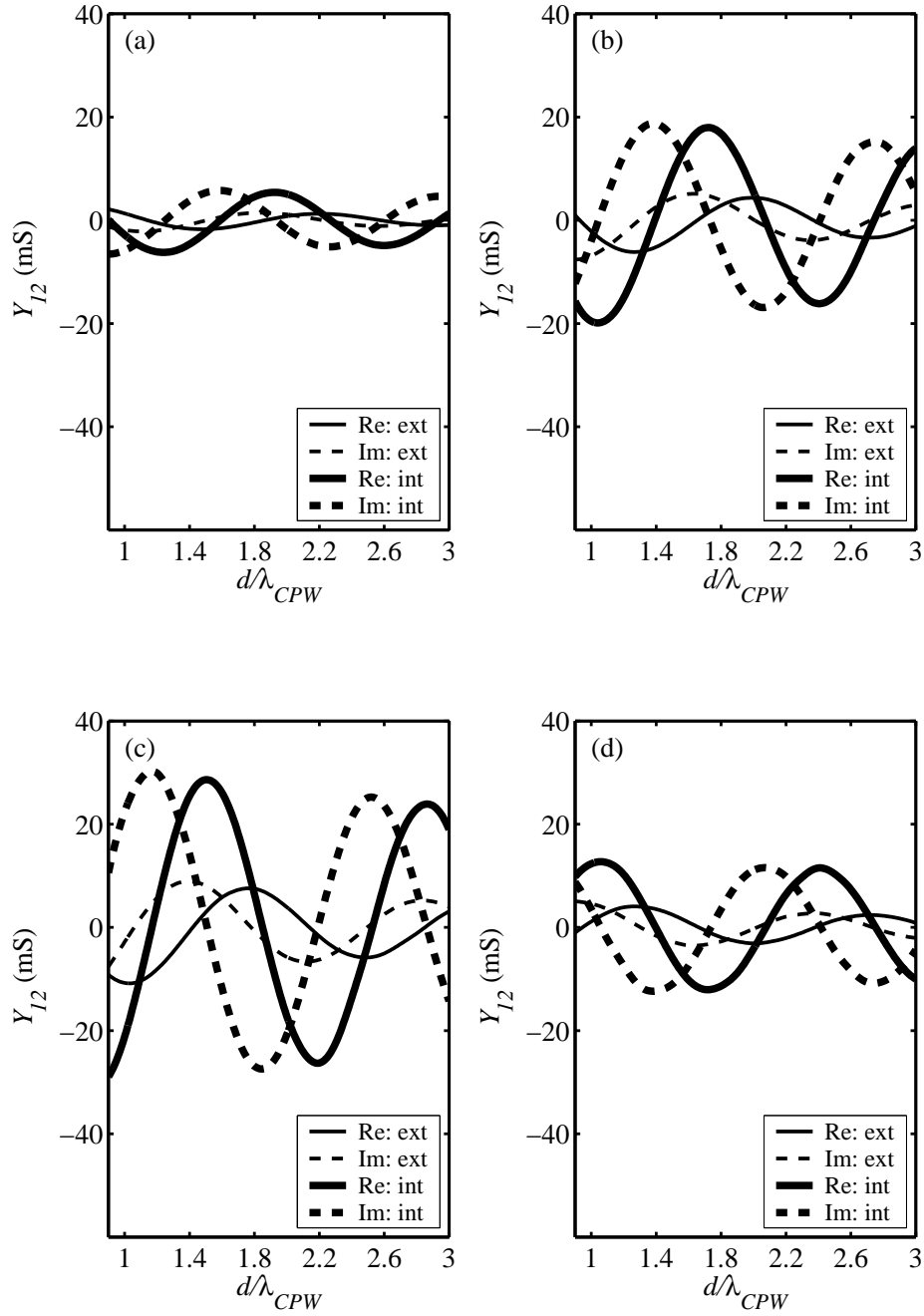


FIGURE 5.39: Y_{12}^{ext} and Y_{12}^{int} against d/λ_{CPW} computed using the reciprocity-expression approach for slots on Substrate I with (a) $L_1 = L_2 = 0.85L_{res}$, (b) $L_1 = L_2 = 0.95L_{res}$, (c) $L_1 = L_2 = L_{res}$, and (d) $L_1 = L_2 = 1.1L_{res}$. $W_1 = W_2 = 0.4$ mm; $h_1 = 0.813$ mm; $h_2 = 5$ mm; $\epsilon_{r1} = 3.38$; $\epsilon_{r2} = 1$; $l_f = 0.5\lambda_{CPW}$.

and Fig. 5.52. For an isolated $1.1L_{res}$ slot, $Y_{self} = 59.6\angle -60.9^\circ$ mS.

As for slots on Substrate I, the two-port self-admittances computed by IE3D appear to oscillate with a decaying envelope about the self-admittances of the isolated slots that are assumed constant regardless of d in the reciprocity-expression approach. This is most apparent for the case

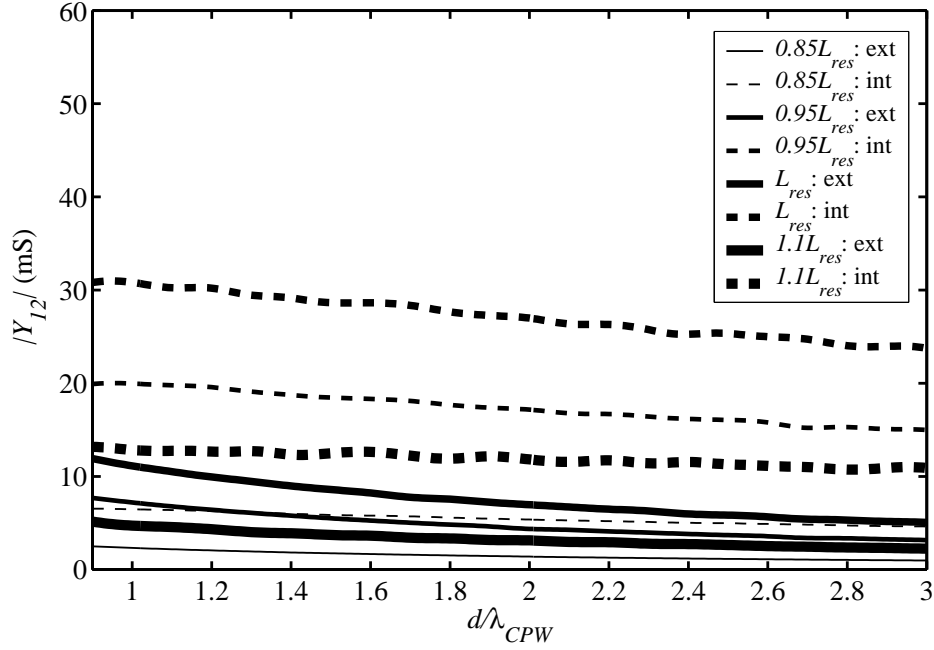


FIGURE 5.40: $|Y_{12}^{ext}|$ and $|Y_{12}^{int}|$ against d/λ_{CPW} for twin slots on Substrate I with $L_1 = L_2 = 0.85L_{res}$, $L_1 = L_2 = 0.95L_{res}$, $L_1 = L_2 = L_{res}$, and $L_1 = L_2 = 1.1L_{res}$. $W_1 = W_2 = 0.4$ mm; $h_1 = 0.813$ mm; $h_2 = 5$ mm; $\epsilon_{r1} = 3.38$; $\epsilon_{r2} = 1$; $l_f = 0.5\lambda_{CPW}$.

$L_1 = L_2 = L_{res}$ as seen in Fig. 5.47, and less so for the cases $L_1 = L_2 = 0.9L_{res}$ and $1.1L_{res}$ (Figs. 5.49 and 5.51). The extent of these oscillations are reflected in the “irregularities” of the IE3D curves for Y_{12} that are the most marked for the case $L_1 = L_2 = L_{res}$, and least significant for $L_1 = L_2 = 0.9L_{res}$; also, $|Y_{11}|$ and $|Y_{12}|$ oscillations appear to be synchronized. As before, discrepancies between IE3D and the reciprocity-expression approach for Y_{12} are consistent with differing accounts for self-admittances in the two models.

As noted previously, the reciprocity-expression approach allows for an estimation of the relative contributions of external and internal mutual admittances to the total mutual admittance,²³ and Fig. 5.53(a)–(c) show Y_{12}^{ext} and Y_{12}^{int} for each of the cases $L_1 = L_2 = 0.9L_{res}$, L_{res} , and $1.1L_{res}$. It is clear that the internal mutual admittance is the dominant contributor. Fig. 5.54 shows the magnitudes of Y_{12}^{ext} and Y_{12}^{int} for the above cases on one plot. It is seen that for each of the three slot half-lengths, the magnitude of the internal mutual admittance is about three times greater than that of the external mutual admittance when $d = 0.9\lambda_{CPW}$, and between five and six times greater when $d = 3\lambda_{CPW}$. Compared to the corresponding curves for Substrate I (*i.e.*, Fig. 5.39 and Fig. 5.40), the electrically thicker top layer of Substrate II appears to concentrate the fields more within it, resulting in greater coupling within the substrate (*cf.* [12]).

²³ The term “estimation” is particularly apt for the $L_1 = L_2 = L_{res}$ case; here the biggest difference is observed between the total mutual admittance obtained using IE3D and the reciprocity-expression approach.

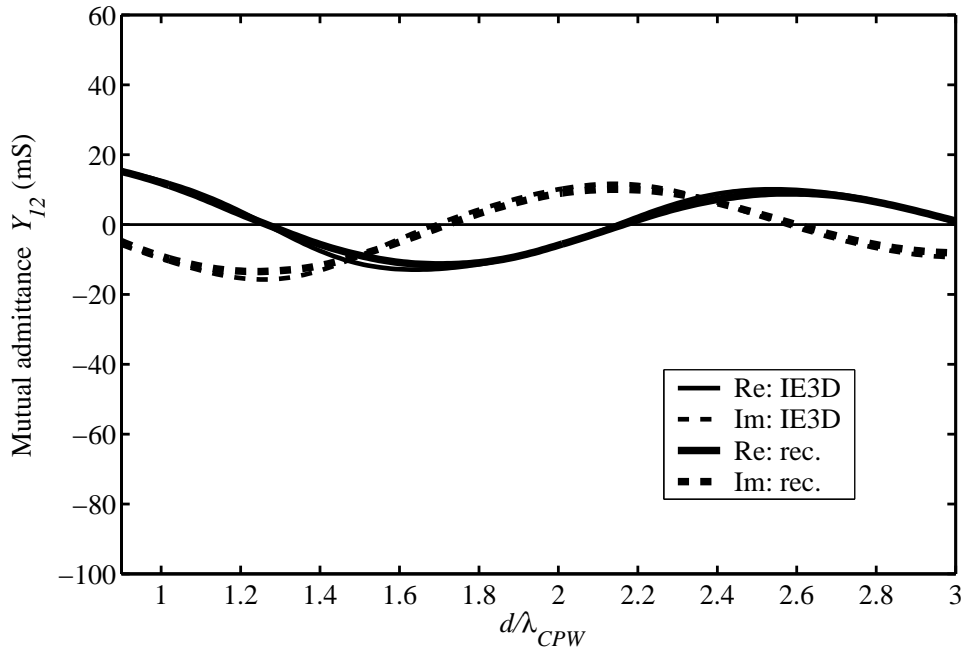


FIGURE 5.41: Mutual admittance Y_{12} against broadside distance d/λ_{CPW} at 10 GHz for CPW-fed twin slots with $L_1 = L_2 = 0.9L_{res} = 6.99$ mm on Substrate II. $W_1 = W_2 = 0.7$ mm; $h_1 = 1.21$ mm; $h_2 = 5$ mm; $\epsilon_{r1} = 6.15$; $\epsilon_{r2} = 1$; $l_f = 0.5\lambda_{CPW}$.

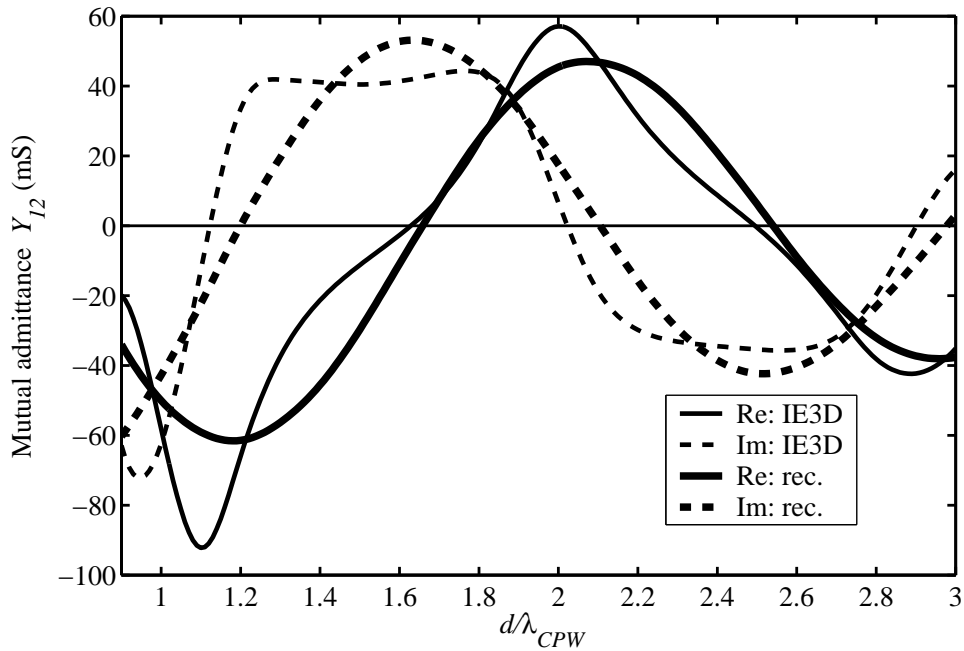


FIGURE 5.42: Mutual admittance Y_{12} against broadside distance d/λ_{CPW} at 10 GHz for CPW-fed twin slots with $L_1 = L_2 = L_{res} = 7.77$ mm on Substrate II. $W_1 = W_2 = 0.7$ mm; $h_1 = 1.21$ mm; $h_2 = 5$ mm; $\epsilon_{r1} = 6.15$; $\epsilon_{r2} = 1$; $l_f = 0.5\lambda_{CPW}$.

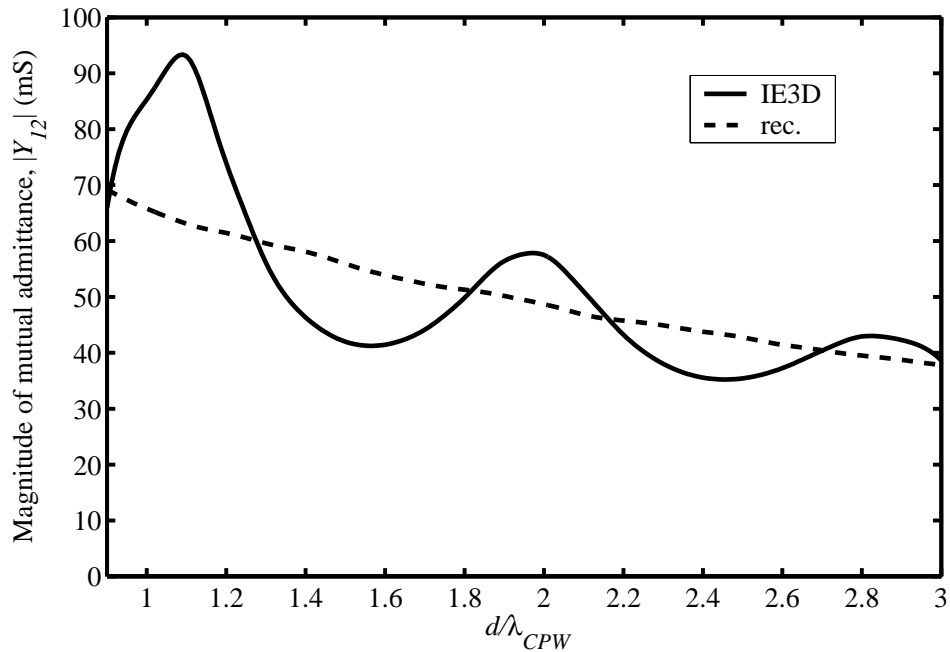


FIGURE 5.43: Magnitude of mutual admittance Y_{12} against broadside distance d/λ_{CPW} at 10 GHz for CPW-fed twin slots with $L_1 = L_2 = L_{res} = 7.77$ mm on Substrate II. $W_1 = W_2 = 0.7$ mm; $h_1 = 1.21$ mm; $h_2 = 5$ mm; $\epsilon_{r1} = 6.15$; $\epsilon_{r2} = 1$; $l_f = 0.5\lambda_{CPW}$.

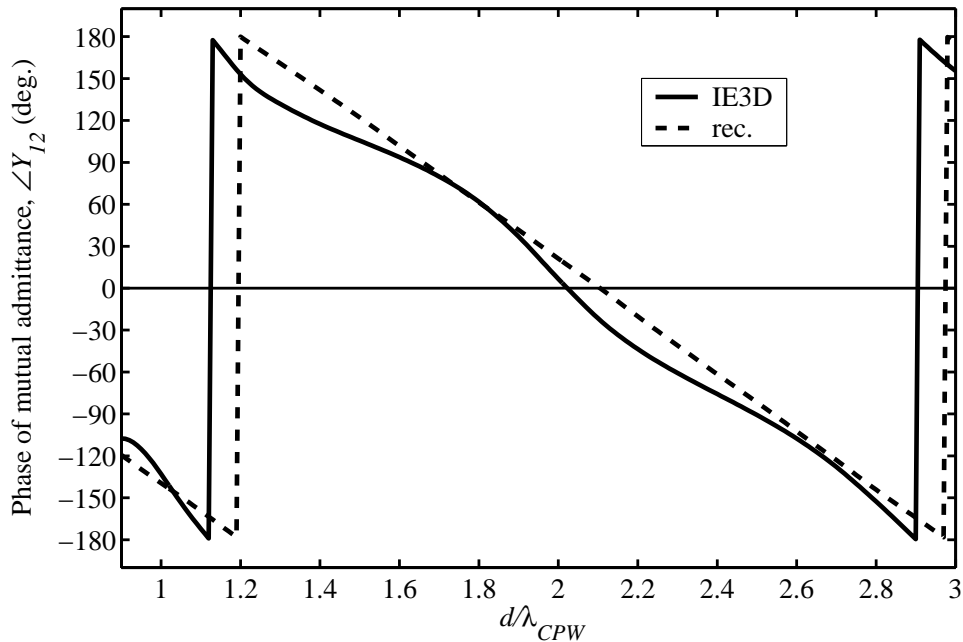


FIGURE 5.44: Phase of mutual admittance Y_{12} against broadside distance d/λ_{CPW} at 10 GHz for CPW-fed twin slots with $L_1 = L_2 = L_{res} = 7.77$ mm on Substrate II. $W_1 = W_2 = 0.7$ mm; $h_1 = 1.21$ mm; $h_2 = 5$ mm; $\epsilon_{r1} = 6.15$; $\epsilon_{r2} = 1$; $l_f = 0.5\lambda_{CPW}$.

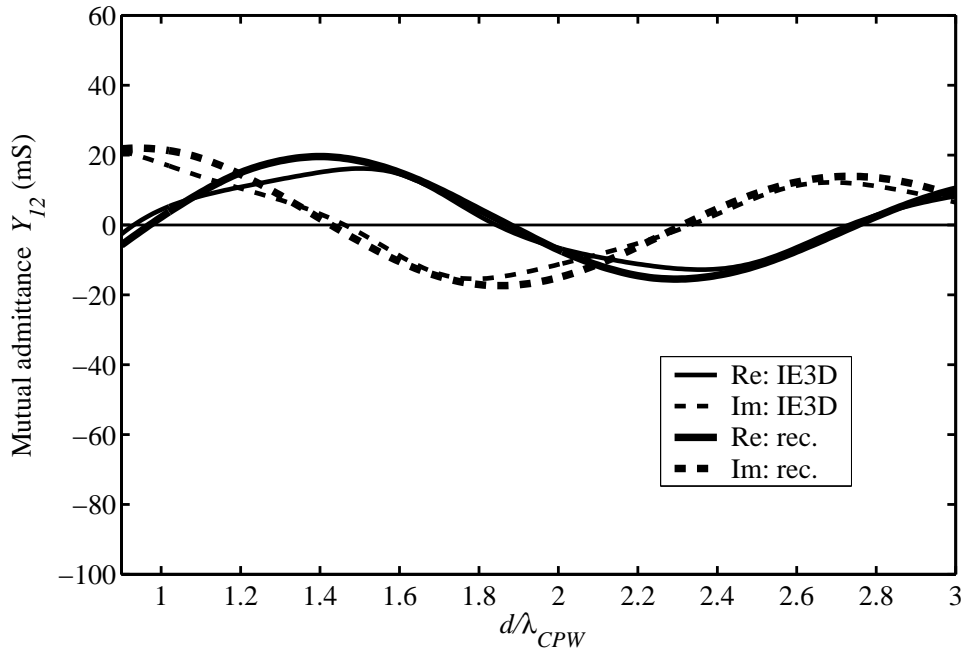


FIGURE 5.45: Mutual admittance Y_{12} against broadside distance d/λ_{CPW} at 10 GHz for CPW-fed twin slots with $L_1 = L_2 = 1.1L_{res} = 8.55$ mm on Substrate II. $W_1 = W_2 = 0.7$ mm; $h_1 = 1.21$ mm; $h_2 = 5$ mm; $\epsilon_{r1} = 6.15$; $\epsilon_{r2} = 1$; $l_f = 0.5\lambda_{CPW}$.

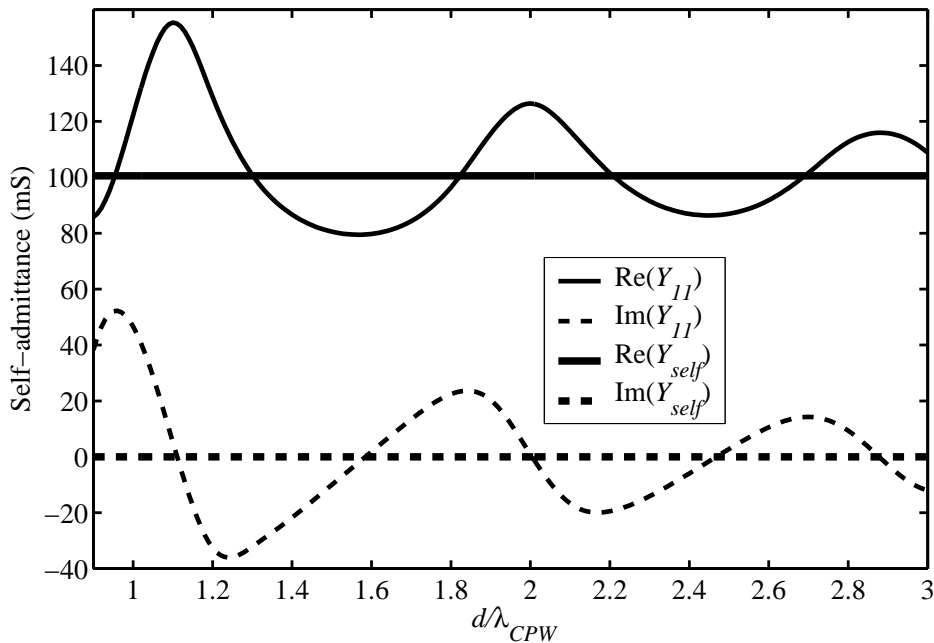


FIGURE 5.46: Two-port self-admittance Y_{11} against broadside distance d/λ_{CPW} for CPW-fed twin slots with $L_1 = L_2 = L_{res} = 7.77$ mm on Substrate II, and resonant isolated self-admittance Y_{self} (both computed at 10 GHz with IE3D). $W_1 = W_2 = 0.7$ mm; $h_1 = 1.21$ mm; $h_2 = 5$ mm; $\epsilon_{r1} = 6.15$; $\epsilon_{r2} = 1$; $l_f = 0.5\lambda_{CPW}$.

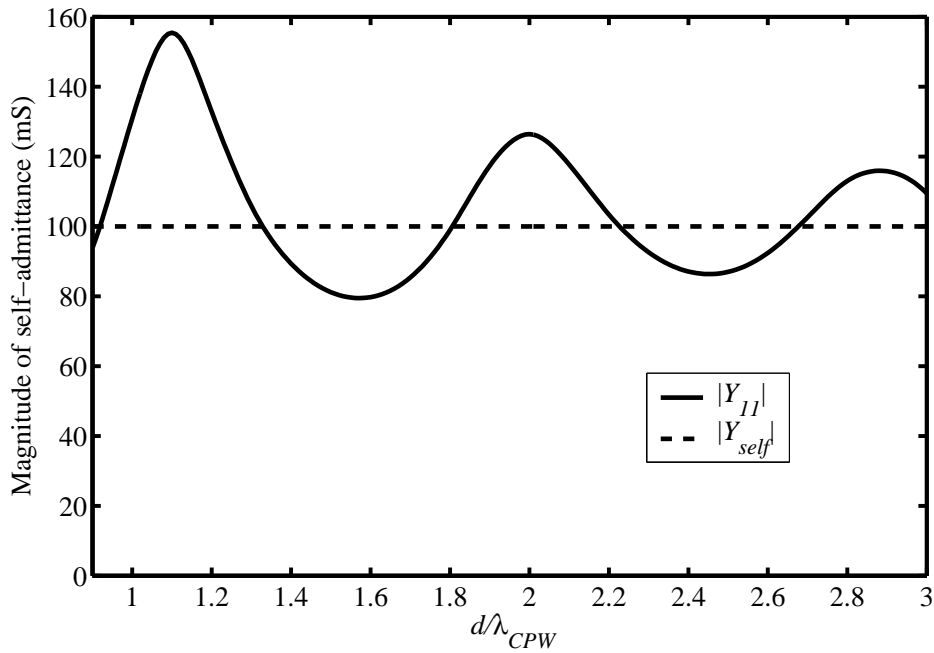


FIGURE 5.47: Magnitude of two-port self-admittance Y_{11} against broadside distance d/λ_{CPW} for CPW-fed twin slots with $L_1 = L_2 = L_{res} = 7.77$ mm on Substrate II, and magnitude of resonant isolated self-admittance Y_{self} (both computed at 10 GHz with IE3D). $W_1 = W_2 = 0.7$ mm; $h_1 = 1.21$ mm; $h_2 = 5$ mm; $\epsilon_{r1} = 6.15$; $\epsilon_{r2} = 1$; $l_f = 0.5\lambda_{CPW}$.

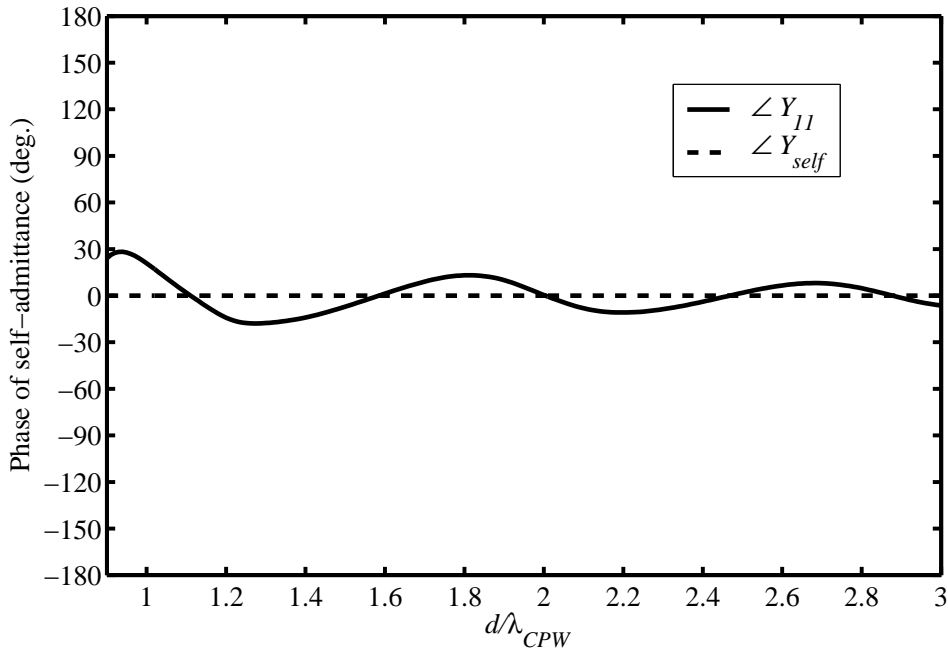


FIGURE 5.48: Phase of two-port self-admittance Y_{11} against broadside distance d/λ_{CPW} for CPW-fed twin slots with $L_1 = L_2 = L_{res} = 7.77$ mm on Substrate II, and phase of resonant isolated self-admittance Y_{self} (both computed at 10 GHz with IE3D). $W_1 = W_2 = 0.7$ mm; $h_1 = 1.21$ mm; $h_2 = 5$ mm; $\epsilon_{r1} = 6.15$; $\epsilon_{r2} = 1$; $l_f = 0.5\lambda_{CPW}$.

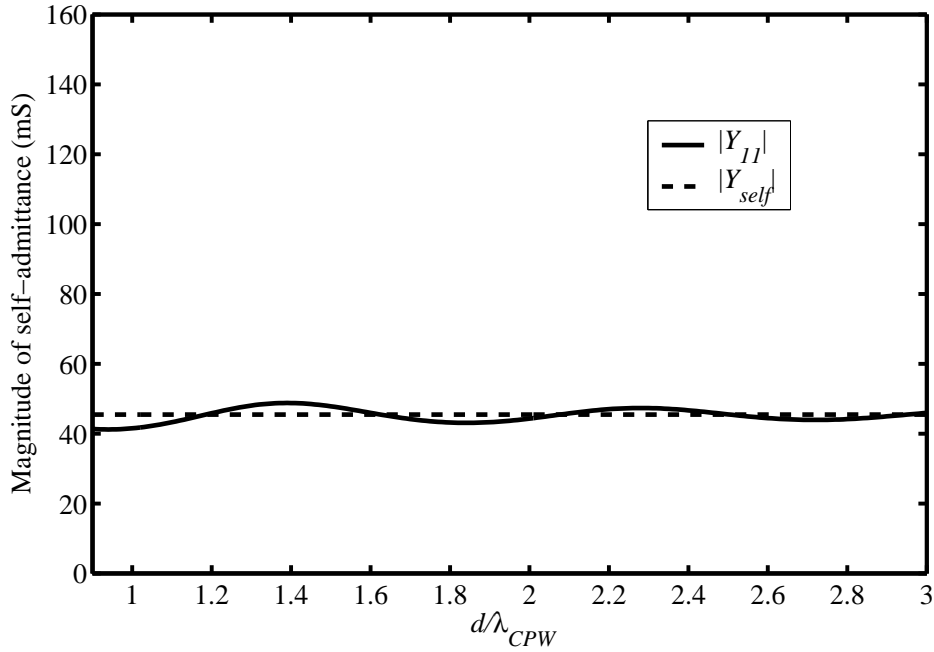


FIGURE 5.49: Magnitude of two-port self-admittance Y_{11} against broadside distance d/λ_{CPW} for CPW-fed twin slots with $L_1 = L_2 = 0.9L_{res} = 6.99$ mm on Substrate II, and magnitude of resonant isolated self-admittance Y_{self} (both computed at 10 GHz with IE3D). $W_1 = W_2 = 0.7$ mm; $h_1 = 1.21$ mm; $h_2 = 5$ mm; $\epsilon_{r1} = 6.15$; $\epsilon_{r2} = 1$; $l_f = 0.5\lambda_{CPW}$.

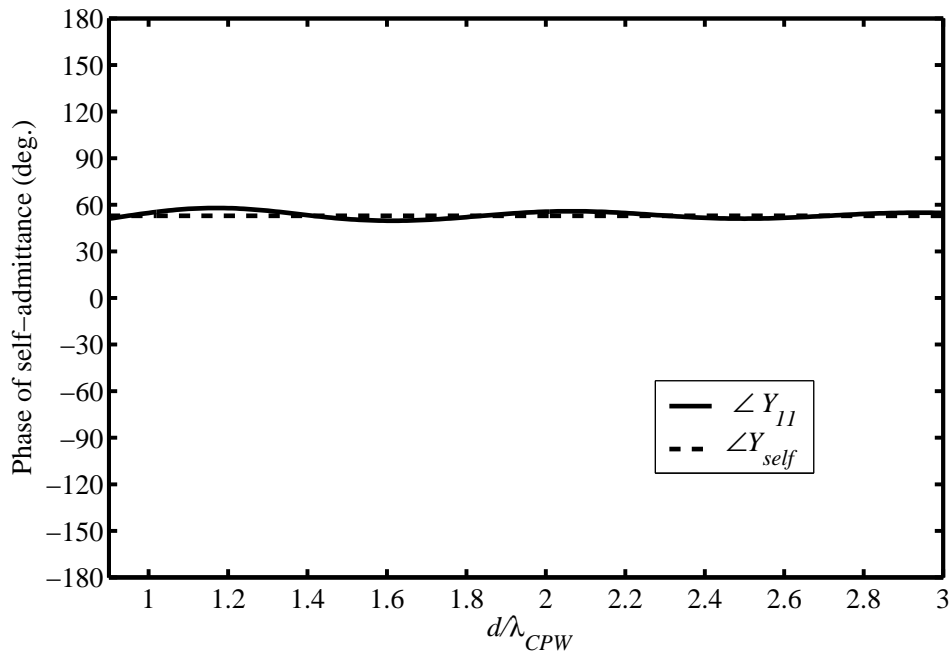


FIGURE 5.50: Phase of two-port self-admittance Y_{11} against broadside distance d/λ_{CPW} for CPW-fed twin slots with $L_1 = L_2 = 0.9L_{res} = 6.99$ mm on Substrate II, and phase of resonant isolated self-admittance Y_{self} (both computed at 10 GHz with IE3D). $W_1 = W_2 = 0.7$ mm; $h_1 = 1.21$ mm; $h_2 = 5$ mm; $\epsilon_{r1} = 6.15$; $\epsilon_{r2} = 1$; $l_f = 0.5\lambda_{CPW}$.

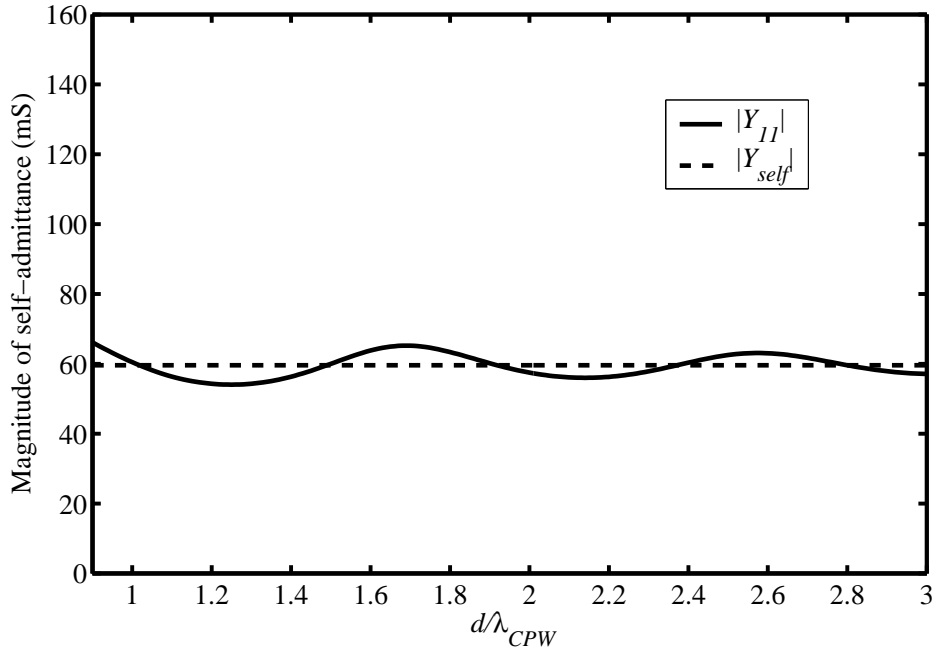


FIGURE 5.51: Magnitude of two-port self-admittance Y_{11} against broadside distance d/λ_{CPW} for CPW-fed twin slots with $L_1 = L_2 = 1.1L_{res} = 8.55$ mm on Substrate II, and magnitude of resonant isolated self-admittance Y_{self} (both computed at 10 GHz with IE3D). $W_1 = W_2 = 0.7$ mm; $h_1 = 1.21$ mm; $h_2 = 5$ mm; $\epsilon_{r1} = 6.15$; $\epsilon_{r2} = 1$; $l_f = 0.5\lambda_{CPW}$.

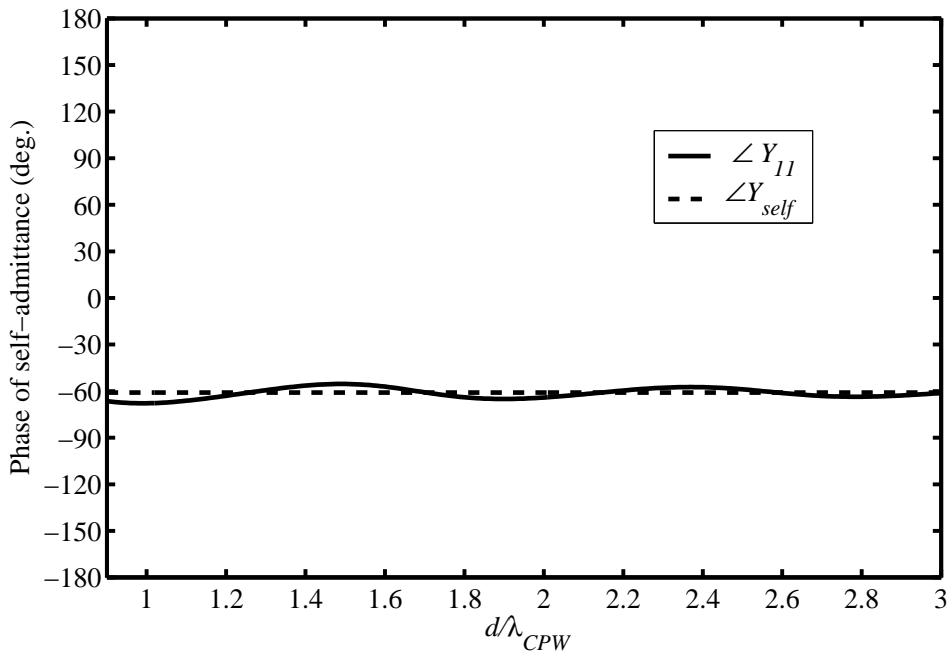


FIGURE 5.52: Phase of two-port self-admittance Y_{11} against broadside distance d/λ_{CPW} for CPW-fed twin slots with $L_1 = L_2 = 1.1L_{res} = 8.55$ mm on Substrate II, and phase of resonant isolated self-admittance Y_{self} (both computed at 10 GHz with IE3D). $W_1 = W_2 = 0.7$ mm; $h_1 = 1.21$ mm; $h_2 = 5$ mm; $\epsilon_{r1} = 6.15$; $\epsilon_{r2} = 1$; $l_f = 0.5\lambda_{CPW}$.

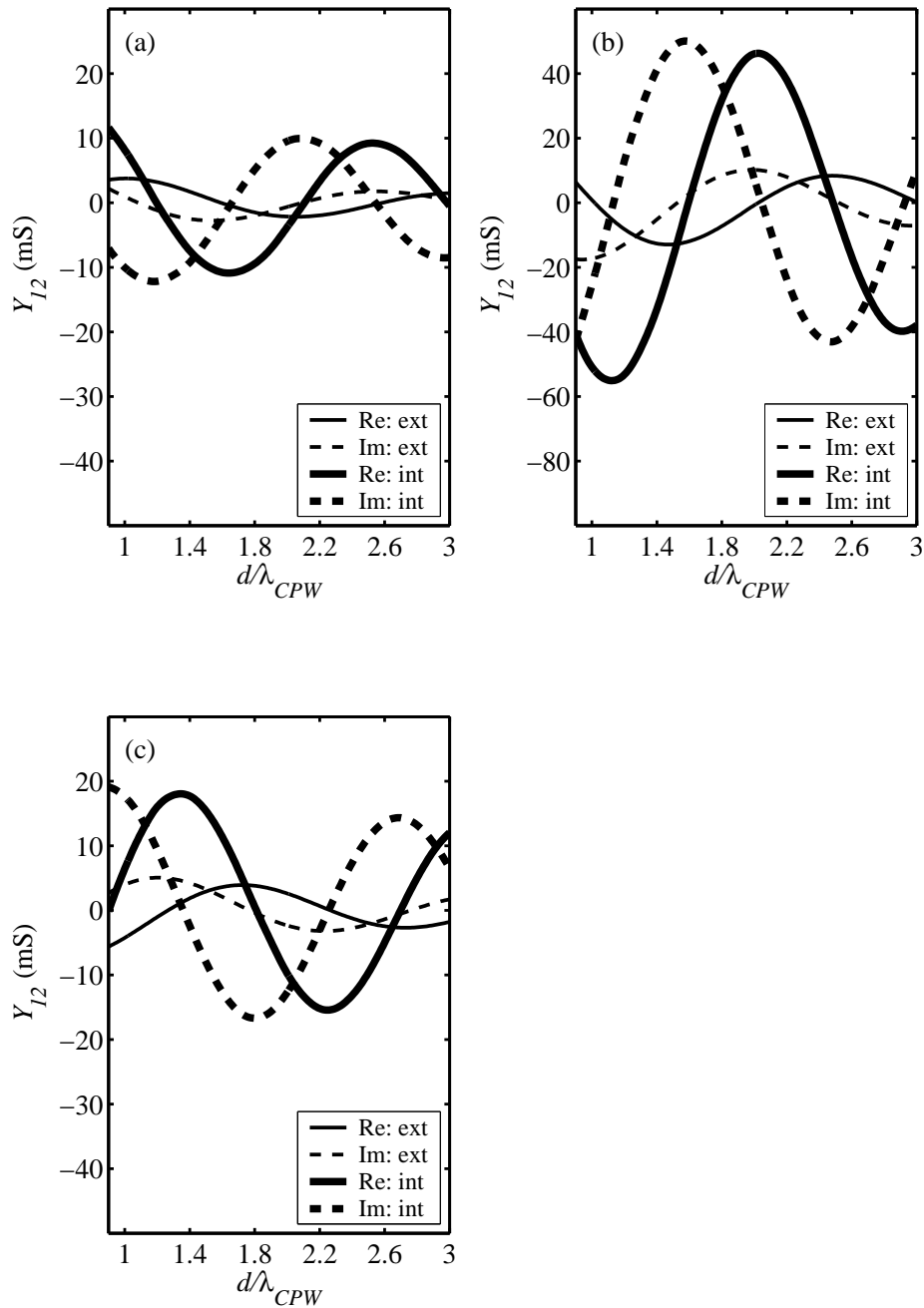


FIGURE 5.53: Y_{12}^{ext} and Y_{12}^{int} against d/λ_{CPW} computed using the reciprocity-expression approach for slots on Substrate II with (a) $L_1 = L_2 = 0.9L_{res}$, (b) $L_1 = L_2 = L_{res}$, and (c) $L_1 = L_2 = 1.1L_{res}$. $W_1 = W_2 = 0.7$ mm; $h_1 = 1.21$ mm; $h_2 = 5$ mm; $\epsilon_{r1} = 6.15$; $\epsilon_{r2} = 1$; $l_f = 0.5\lambda_{CPW}$.

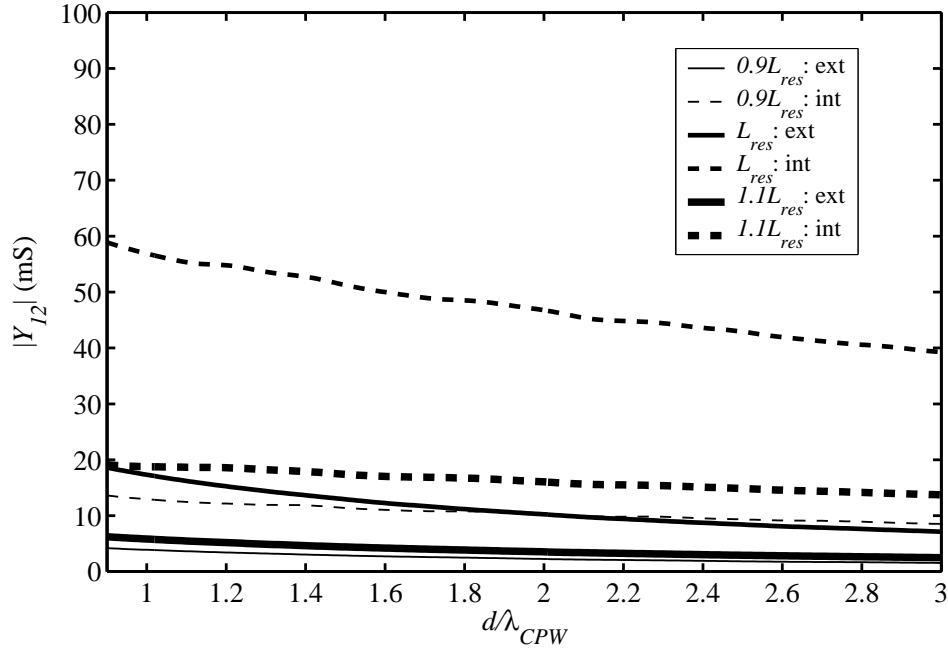


FIGURE 5.54: $|Y_{12}^{ext}|$ and $|Y_{12}^{int}|$ against d/λ_{CPW} for twin slots on Substrate II with $L_1 = L_2 = 0.9L_{res}$, $L_1 = L_2 = L_{res}$, and $L_1 = L_2 = 1.1L_{res}$. $W_1 = W_2 = 0.7$ mm; $h_1 = 1.21$ mm; $h_2 = 5$ mm; $\epsilon_{r1} = 6.15$; $\epsilon_{r2} = 1$; $l_f = 0.5\lambda_{CPW}$.

5.4.2.3 Substrate III: $h_1 = 0.013\lambda_d$, $h_2 = \lambda_0/6$, $\epsilon_{r1} = 2.2$, $\epsilon_{r2} = 1$

The top layer of Substrate III is substantially thinner electrically than that of Substrate I, *i.e.*, $0.013\lambda_d$ as opposed to $0.05\lambda_d$. An 86Ω CPW feed line was designed on this substrate in IE3D that had $w = 1.2$ mm and $s = 0.3$ mm. Next, an isolated CPW-fed radiating slot with a width W of 0.18 mm was designed to operate at its second resonance at 10 GHz resulting in $L = L_{res} = 12.75$ mm and a resonant self-impedance of about 16Ω . Mutual admittance Y_{12} against distance d with $0.9\lambda_{CPW} \leq d \leq 3\lambda_{CPW}$ was computed for three instances of twin slots with $W_1 = W_2 = 0.18$ mm throughout, and slot half-lengths of $L_1 = L_2 = 0.9L_{res}$, L_{res} , and $1.1L_{res}$.

The real and imaginary parts of the mutual admittance Y_{12} against normalized broadside distance d/λ_{CPW} for twin slots with $L_1 = L_2 = 0.9L_{res} = 11.48$ mm computed using the reciprocity-expression approach and IE3D are shown in Fig. 5.55. Y_{12} curves for twin slots with half-lengths $L_{res} = 12.75$ mm and $1.1L_{res} = 14.03$ mm are shown in Figs. 5.56 and 5.57 respectively; feed line lengths were $l_f = 0.5\lambda_{CPW}$ throughout. Figs. 5.55–5.57 confirm the main trends exhibited by slots on Substrates I and II; given this similarity and the detailed investigations already presented in Sections 5.4.2.1 and 5.4.2.2, the present substrate will not be treated further here.

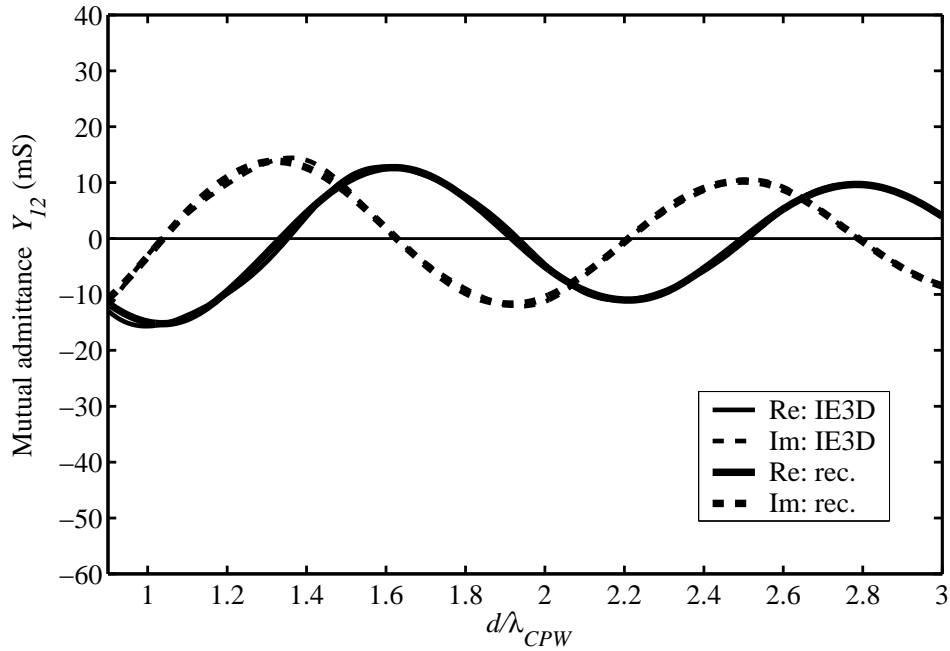


FIGURE 5.55: Mutual admittance Y_{12} against broadside distance d/λ_{CPW} at 10 GHz for CPW-fed twin slots with $L_1 = L_2 = 0.9L_{res} = 11.48$ mm on Substrate III. $W_1 = W_2 = 0.18$ mm; $h_1 = 0.254$ mm; $h_2 = 5$ mm; $\epsilon_{r1} = 2.2$; $\epsilon_{r2} = 1$; $l_f = 0.5\lambda_{CPW}$.

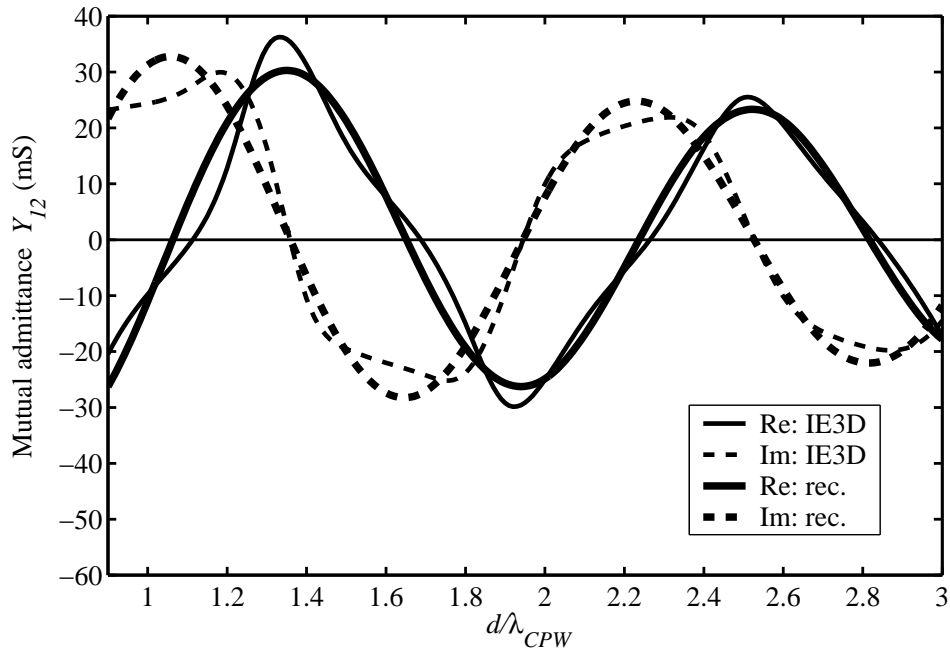


FIGURE 5.56: Mutual admittance Y_{12} against broadside distance d/λ_{CPW} at 10 GHz for CPW-fed twin slots with $L_1 = L_2 = L_{res} = 12.75$ mm on Substrate III. $W_1 = W_2 = 0.18$ mm; $h_1 = 0.254$ mm; $h_2 = 5$ mm; $\epsilon_{r1} = 2.2$; $\epsilon_{r2} = 1$; $l_f = 0.5\lambda_{CPW}$.

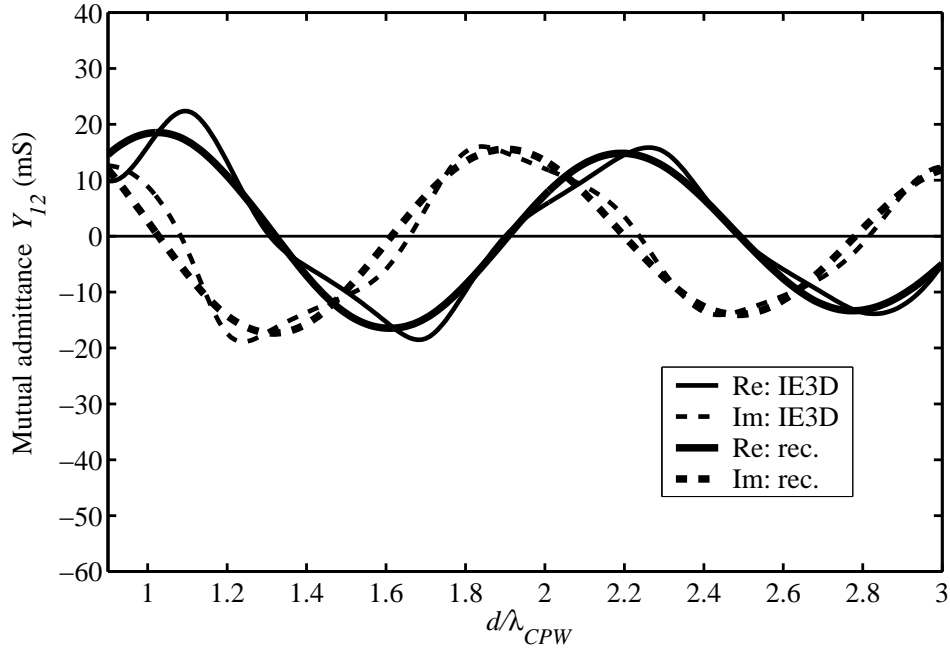


FIGURE 5.57: Mutual admittance Y_{12} against broadside distance d/λ_{CPW} at 10 GHz for CPW-fed twin slots with $L_1 = L_2 = 1.1L_{res} = 14.03$ mm on Substrate III. $W_1 = W_2 = 0.18$ mm; $h_1 = 0.254$ mm; $h_2 = 5$ mm; $\epsilon_{r1} = 2.2$; $\epsilon_{r2} = 1$; $l_f = 0.5\lambda_{CPW}$.

5.4.2.4 Effect of shift in two-port reference planes

Noting that a shift in reference planes has impedance transformation implications, Y_{12} against d was computed for broadside twin slots on Substrate I with $L_1 = L_2 = L_{res}$, and CPW feed lines of length $l_f = 0.4\lambda_{CPW}$ (instead of $0.5\lambda_{CPW}$ as before). Results obtained using the reciprocity-expression approach and IE3D are shown in Fig. 5.58. The IE3D result is now free from the “irregular” behaviour displayed in Fig. 5.26 for feed line lengths of $0.5\lambda_{CPW}$, and the agreement between the two methods is quite good. Fig. 5.59 shows the real and imaginary parts of the two-port self-admittance Y_{11} against d/λ_{CPW} , as well as the isolated self-admittance Y_{self} computed using a $0.4\lambda_{CPW}$ feed line; the quantities are in close agreement. The moment-method (IE3D) Y_{11} is essentially free from the oscillatory behaviour about the isolated slot self-admittance seen in the $l_f = 0.5\lambda_{CPW}$ case (*cf.* Fig. 5.30). Hence, when reference planes are defined at the ends of feed lines of length $l_f = 0.4\lambda_{CPW}$, the assumption in the reciprocity-expression method of slot self-admittances that do not change from the isolated slot self-admittance value as d varies, is borne out by the IE3D two-port Y_{11} . This explains the good agreement between the two methods in regard to Y_{12} of Fig. 5.58.

In a further step, the IE3D Y parameters of Figs. 5.58 and 5.59 were transformed to the original reference planes at the ends of $l_f = 0.5\lambda_{CPW}$ feed lines by converting them to S parameters using

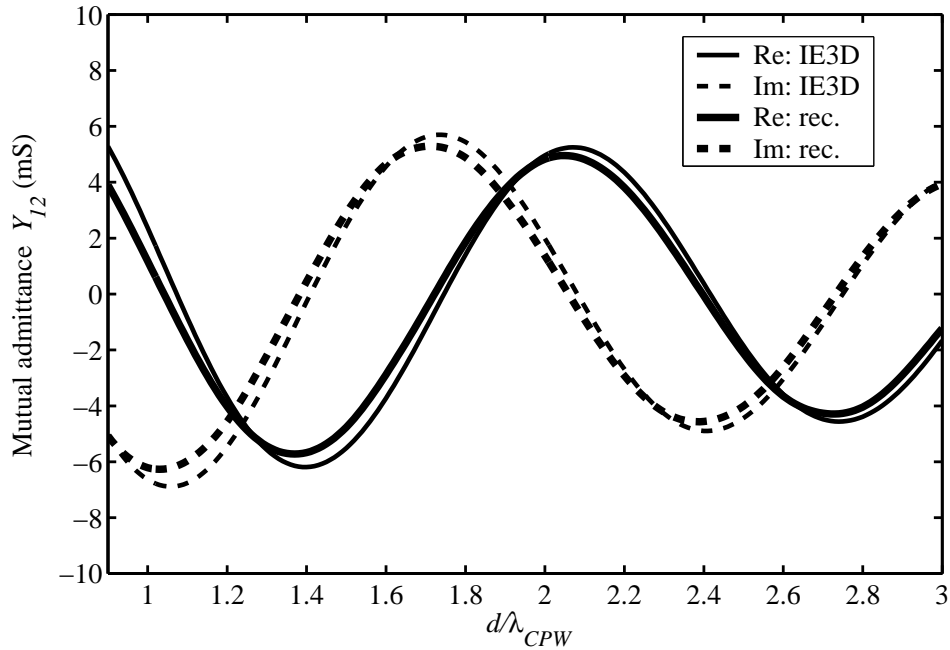


FIGURE 5.58: Mutual admittance Y_{12} against broadside distance d/λ_{CPW} at 10 GHz for CPW-fed twin slots with $L_1 = L_2 = L_{res} = 10.87$ mm on Substrate I with $l_f = 0.4\lambda_{CPW}$. $W_1 = W_2 = 0.4$ mm; $h_1 = 0.813$ mm; $h_2 = 5$ mm; $\epsilon_{r1} = 3.38$; $\epsilon_{r2} = 1$.

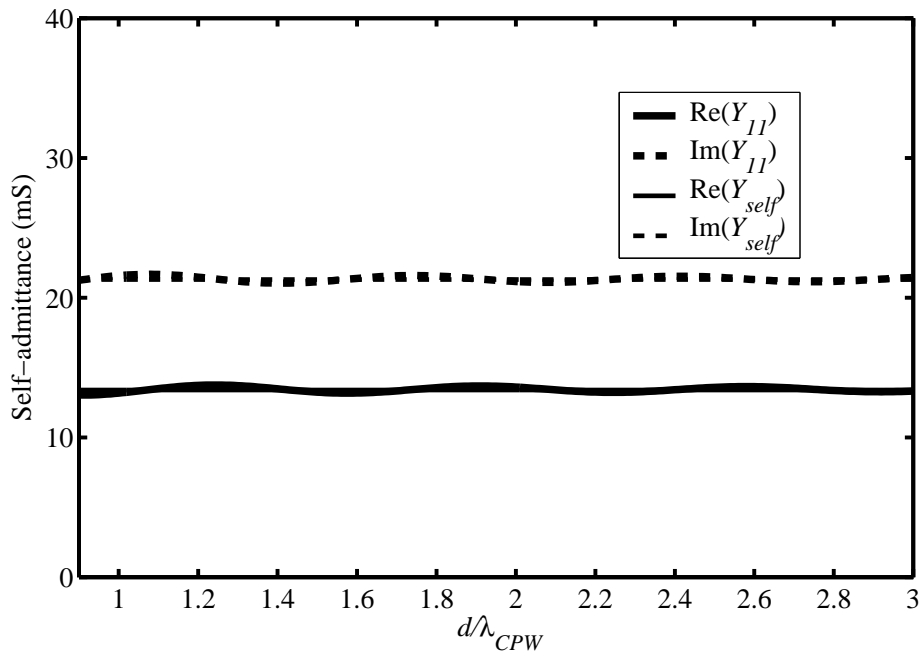


FIGURE 5.59: Two-port self-admittance Y_{11} against broadside distance d/λ_{CPW} for CPW-fed twin slots with $L_1 = L_2 = L_{res} = 10.87$ mm on Substrate I with $l_f = 0.4\lambda_{CPW}$, and isolated slot self-admittance Y_{self} (both computed with IE3D at 10 GHz). $W_1 = W_2 = 0.4$ mm; $h_1 = 0.813$ mm; $h_2 = 5$ mm; $\epsilon_{r1} = 3.38$; $\epsilon_{r2} = 1$.

standard formulas [90, Table 4.2], multiplying these S parameters by a phase factor corresponding to an outward shift in reference planes of $0.1\lambda_{CPW}$, and converting the transformed S parameters



back to Y parameters. Results for Y_{11} and Y_{12} were very close to the original IE3D Y_{11} and Y_{12} of Figs. 5.30 and 5.26, suggesting that these $0.1\lambda_{CPW}$ sections of CPW for the original twin slot configuration ($l_f = 0.5\lambda_{CPW}$) fulfill a largely impedance-transforming role in the manner of sections of transmission line, with minimal coupling to other slots in the twin slot configuration.

Transforming the reciprocity-expression Y_{12} of Fig. 5.58 ($l_f = 0.4\lambda_{CPW}$) in conjunction with Y_{self} of Fig. 5.59 ($l_f = 0.4\lambda_{CPW}$) back to reference planes corresponding to $l_f = 0.5\lambda_{CPW}$, yielded a Y_{12} in close agreement with the original IE3D-computed Y_{12} of Fig. 5.26, as shown in Fig. 5.60 (in the 2×2 matrix of two-port Y parameters, the positions on the diagonal were filled by Y_{self} for all values of d). Notably, the reciprocity-expression Y_{12} curves now are “irregular” in a manner similar to the IE3D curves obtained for $l_f = 0.5\lambda_{CPW}$. This suggests that the reciprocity-expression approach can be used as follows to obtain Y_{12} curves for L_{res} twin slots – referred to the centres of radiating slots – that take on the “irregular” behaviour of the corresponding IE3D curves. First, identify a set of reference planes (and the corresponding feed line lengths) for which Y_{11} against d is relatively constant. Second, since the reciprocity-expression assumption of unchanging self-admittances would apply, determine Y_{12} using the reciprocity-expression method; this includes a once-off moment-method analysis of the corresponding isolated slot, which could yield the isolated self-admittance Y_{self} in addition to the required slot field and terminal voltage. Finally, construct an approximate Y parameter matrix from Y_{self} and Y_{12} for each value of d , and transform it to $l_f = 0.5\lambda_{CPW}$ reference planes as described above.

In order to confirm the above observations, Y_{12} against d was computed for CPW-fed twin slots with $L_1 = L_2 = L_{res}$ and $W_1 = W_2 = 0.7$ mm on Substrate II with feed lines of length $l_f = 0.4\lambda_{CPW}$. Results obtained using the reciprocity-expression approach and IE3D are shown in Fig. 5.61. The agreement between the two methods is very good. Fig. 5.62 shows the real and imaginary parts of the two-port self-admittance Y_{11} against d/λ_{CPW} , as well as the isolated self-admittance Y_{self} computed using a $0.4\lambda_{CPW}$ feed line; the quantities are in very close agreement. Hence the assumption in the reciprocity-expression method of slot self-admittances that do not change with d is validated by the IE3D two-port Y_{11} , explaining the good agreement between the two methods with respect to Y_{12} in Fig. 5.61.

As before, the IE3D Y parameters of Figs. 5.61 and 5.62 were transformed back to reference planes at the ends of the original $l_f = 0.5\lambda_{CPW}$ feed lines. Results for Y_{11} and Y_{12} were virtually identical to the original IE3D Y_{11} and Y_{12} of Figs. 5.46 and 5.42, suggesting in regard to the original twin slot configuration ($l_f = 0.5\lambda_{CPW}$) that there is negligible interaction between the outermost $0.1\lambda_{CPW}$ sections of CPW and the rest of the structure. Hence these $0.1\lambda_{CPW}$ sections of CPW

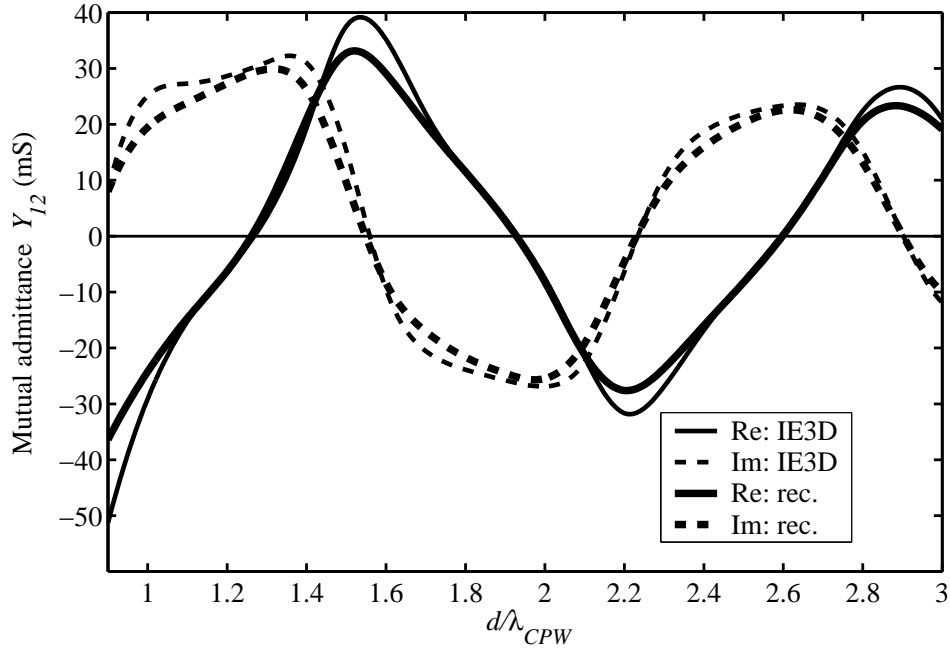


FIGURE 5.60: Mutual admittance Y_{12} against broadside distance d/λ_{CPW} at 10 GHz for CPW-fed twin slots with $L_1 = L_2 = L_{res} = 10.87$ mm on Substrate I. Reciprocity-expression results were transformed from reference planes $l_f = 0.4\lambda_{CPW}$ to $l_f = 0.5\lambda_{CPW}$ (IE3D results are the same as in Fig. 5.26). $W_1 = W_2 = 0.4$ mm; $h_1 = 0.813$ mm; $h_2 = 5$ mm; $\epsilon_{r1} = 3.38$; $\epsilon_{r2} = 1$.

appear to behave in a purely transmission-line-like manner.

Transforming the reciprocity-expression Y_{12} of Fig. 5.61 ($l_f = 0.4\lambda_{CPW}$) in conjunction with Y_{self} of Fig. 5.62 back to reference planes corresponding to $l_f = 0.5\lambda_{CPW}$ in the manner described above, yielded a Y_{12} in close agreement with the original IE3D-computed Y_{12} of Fig. 5.42, as shown in Fig. 5.63 (in the matrix of two-port Y parameters, the positions on the diagonal were filled by Y_{self} for all values of d). As in the Substrate I case, the reciprocity-expression Y_{12} curves were now “irregular” in a manner similar to that of the IE3D curves obtained for $l_f = 0.5\lambda_{CPW}$. This confirms that accurate Y_{12} curves referred to the centres of radiating slots can be obtained from the reciprocity-expression approach in the manner proposed above.

5.4.2.5 Experimental results

Y_{12} against frequency was computed using the reciprocity-expression approach and IE3D for a twin slot configuration with a layout such as that of Fig. 5.1 on Substrate I (see Section 5.4.2.1) using fixed radiating slot dimensions $L_1 = L_2 = L_{res, 10\text{ GHz}} = 10.87$ mm and $W_1 = W_2 = 0.4$ mm, and a fixed inter-slot spacing $d = \lambda_{CPW, 10\text{ GHz}} = 21.5$ mm, where $L_{res, 10\text{ GHz}}$ and $\lambda_{CPW, 10\text{ GHz}}$ are the slot second-resonant half-length and CPW wavelength respectively at 10 GHz (CPW dimensions were those of Section 5.4.2.1).

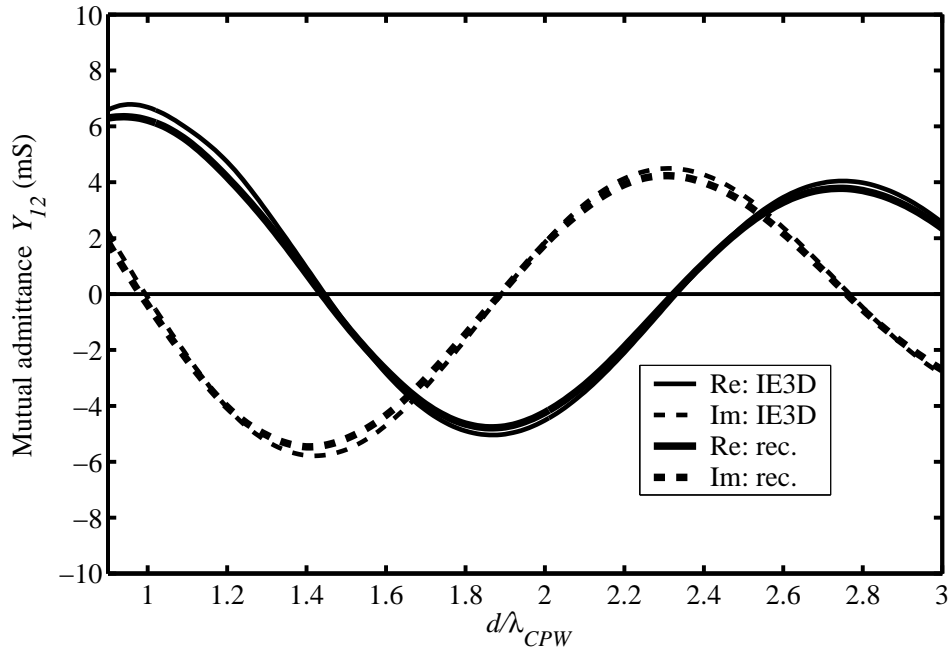


FIGURE 5.61: Mutual admittance Y_{12} against broadside distance d/λ_{CPW} at 10 GHz for CPW-fed twin slots with $L_1 = L_2 = L_{res} = 7.77$ mm on Substrate II with $l_f = 0.4\lambda_{CPW}$. $W_1 = W_2 = 0.7$ mm; $h_1 = 1.21$ mm; $h_2 = 5$ mm; $\epsilon_{r1} = 6.15$; $\epsilon_{r2} = 1$.

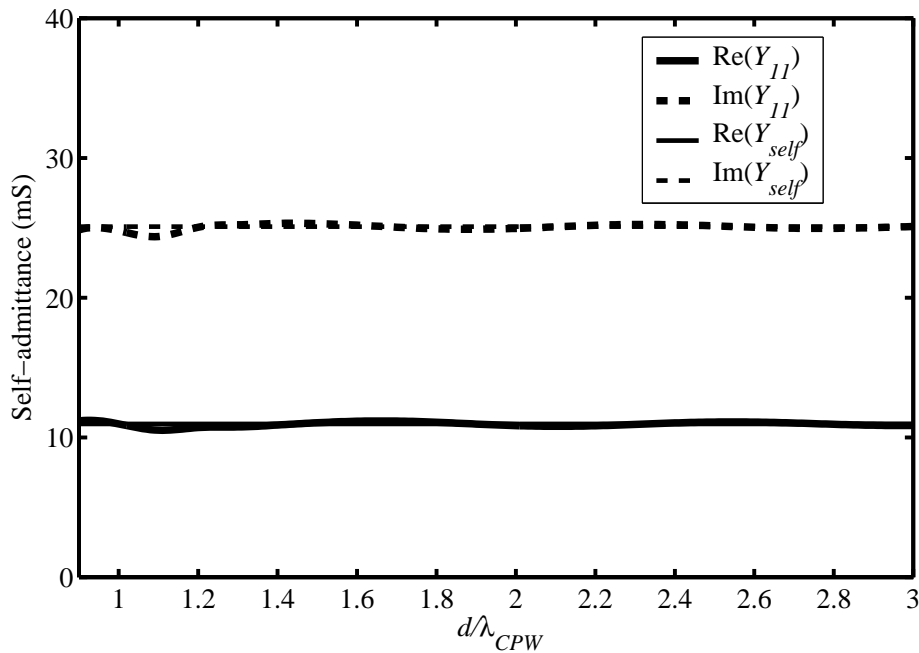


FIGURE 5.62: Two-port self-admittance Y_{11} against broadside distance d/λ_{CPW} at 10 GHz computed with IE3D for CPW-fed twin slots with $L_1 = L_2 = L_{res} = 7.77$ mm on Substrate II with $l_f = 0.4\lambda_{CPW}$. $W_1 = W_2 = 0.7$ mm; $h_1 = 1.21$ mm; $h_2 = 5$ mm; $\epsilon_{r1} = 6.15$; $\epsilon_{r2} = 1$.

The twin slot configuration was subsequently etched on RO4003C laminate that served as top

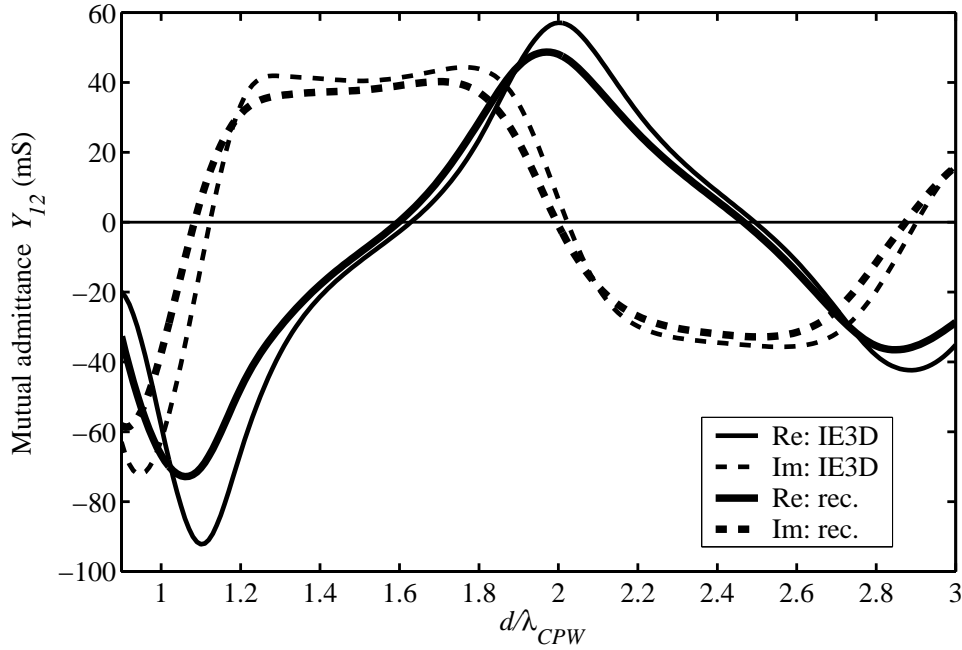


FIGURE 5.63: Mutual admittance Y_{12} against broadside distance d/λ_{CPW} at 10 GHz for CPW-fed twin slots with $L_1 = L_2 = L_{res} = 7.77$ mm on Substrate II. Reciprocity-expression results were transformed from reference planes $l_f = 0.4\lambda_{CPW}$ to $l_f = 0.5\lambda_{CPW}$ (IE3D results are the same as in Fig. 5.42). $W_1 = W_2 = 0.7$ mm; $h_1 = 1.21$ mm; $h_2 = 5$ mm; $\epsilon_{r1} = 6.15$; $\epsilon_{r2} = 1$.

dielectric layer (RO4003C has $\epsilon_r = 3.38 \pm 0.05$ and $\tan \delta = 0.0027$ at 10 GHz [91]); polystyrene was used for the bottom (air) layer. The CPW feed lines were each extended for $9\lambda_{CPW, 10\text{ GHz}}$ beyond the $l_f = 0.5\lambda_{CPW, 10\text{ GHz}}$ reference planes to allow for proper gating out in the time-domain of transition phenomena associated with the coax-launcher-to-CPW transitions at the edges of the substrate; measured S parameters were subsequently transformed back to the $l_f = 0.5\lambda_{CPW, 10\text{ GHz}}$ reference planes taking into account dielectric and conductor losses on the CPW extensions that were estimated via a reflection measurement involving a short-circuited section of CPW transmission line. S parameters were converted to Y parameters using standard relations [90, Table 4.2]. Fig. 5.64 shows good agreement between the computed and measured mutual admittance Y_{12} against frequency for the above twin slots.

5.5 CONCLUSIONS

An approach based on a well-known reciprocity-based expression was developed for finding the mutual admittance between two broadside CPW-fed slots on a conductor-backed two-layer substrate. The approach is simpler than a full moment-method analysis, and hence more amenable to repeated evaluation in an array design procedure. It entails a number of simplifying assumptions: these include negligible interaction of radiating slots with CPW feed lines, and of feed lines with themselves; and

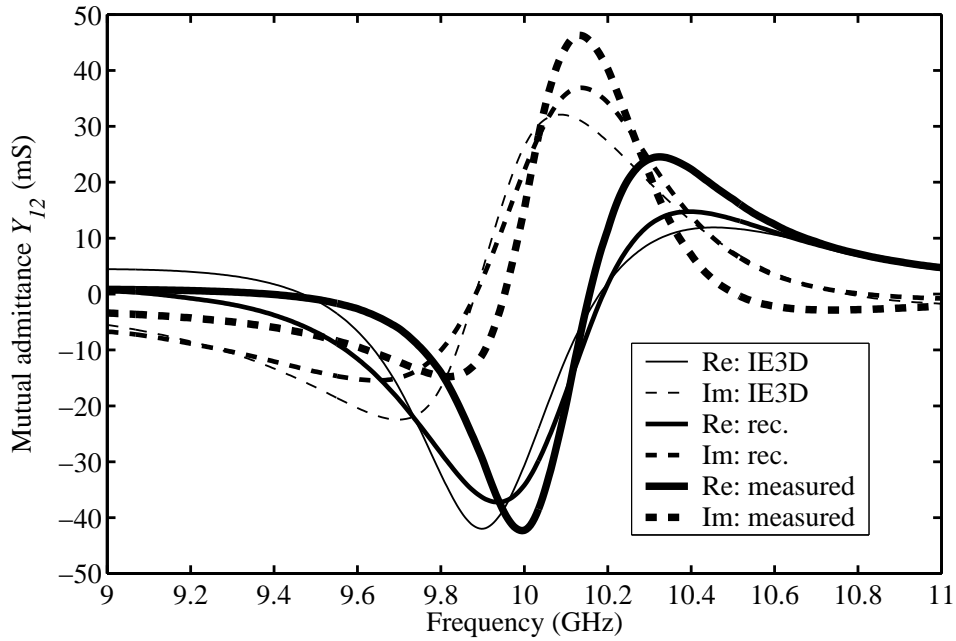


FIGURE 5.64: Mutual admittance Y_{12} against frequency of CPW-fed twin slots on Substrate I. $L_1 = L_2 = L_{res, 10 GHz} = 10.87$ mm; $W_1 = W_2 = 0.4$ mm; $d = \lambda_{CPW, 10 GHz} = 21.5$ mm; $h_1 = 0.813$ mm; $h_2 = 5$ mm; $\epsilon_{r1} = 3.38$; $\epsilon_{r2} = 1$.

a radiating slot aperture field that is directed across the width of the slot. In order to compute Y_{12} between two CPW-fed slots against inter-slot spacing d , the reciprocity-expression approach requires the electric field and “terminal” voltage of each slot radiating in isolation (*i.e.*, the voltage at the end of the CPW feed line, which includes the effect of the CPW-to-radiating-slot transition). This implies the necessity of a once-only moment-method analysis of each isolated slot.

The logistic implications for an array design procedure is not excessive, since in traditional design algorithms [19, 35], isolated slot self-admittance data need to be generated anyway (typically by means of the moment method). Afterwards, the reciprocity-expression approach allows for the mutual admittance between slot pairs of arbitrary dimensions and inter-slot spacings to be evaluated using isolated slot terminal voltages in conjunction with isolated slot electric field distributions. Alternatively, only the complex amplitude of the slot field (as opposed to the complete field distribution) can be extracted from the isolated slot analysis, and then used to scale generic functions that approximate the slot field; for example, it is straightforward to relate piecewise sinusoidal functions to slot field magnitudes.

The reciprocity-expression approach evaluates external and internal contributions to the total mutual admittance separately. The internal mutual admittance formulation required derivation of a spatial-domain Green’s function for finding the \hat{x} -component of the magnetic field inside



the two-layer parallel-plate substrate due to an \hat{x} -directed equivalent surface magnetic current density representing a radiating slot in the top conducting plate. From known spectral-domain equivalent circuits for general layered media, equivalent circuits for the TM and TE contributions to the \hat{x} -component of the magnetic field of an appropriately-positioned \hat{x} -directed HMD in the conductor-backed two-layer substrate were obtained. Using these as a starting point, the spatial-domain Green's function was determined as a sum of singular Sommerfeld-type integrals (to the knowledge of the author, this has not been published before); treatment of the singularities was discussed.

Using the reciprocity-expression approach, mutual admittance Y_{12} against slot separation d was computed for broadside CPW-fed twin slots and some non-identical slot pairs on three different conductor-backed two-layer substrates. The substrates had the same air bottom layer, and top layers of contrasting dielectric thickness. For each substrate, three or four broadside twin slot configurations were considered that had radiating slot half-lengths in the vicinity of the second-resonant half-length of an isolated slot on the substrate. Results from the reciprocity-expression method were compared to results from moment-method-based simulations using IE3D.

Good agreement was observed between the above methods when Y parameter calculations were, as is customary, referred to radiating slot centres by choosing CPW feed lines that were $0.5\lambda_{CPW}$ long. The greatest discrepancy occurred for twin slots that had the same half-length as an isolated second-resonant slot on the substrate. Here, IE3D curves appeared like “irregular” versions of the reciprocity-expression curves, with the deviation the most marked for the substrate with the top layer that had the greatest dielectric thickness. (The effect was considerably less marked for twin slots with half-lengths away from the isolated second-resonant half-length, and virtually unobservable for half-lengths that were 10-15% shorter than the resonant half-length.) Further investigation linked the discrepancy for the resonant-length slots to the manner in which slot self-properties are accounted for in the two models: the reciprocity-expression approach assumes unchanging slot self-admittance values equal to the corresponding isolated slot self-admittances, while IE3D in fact predicted two-port self-admittances that were not constant as a function of inter-slot distance, “oscillating” about the isolated slot self-admittances.

By contrast, completely “regular” IE3D mutual admittance curves, as well as essentially constant two-port self-admittance curves that equalled the isolated slot self-admittance values, were obtained for resonant-length slots when a shift of reference planes was established by reducing feed line lengths, *i.e.*, to $0.4\lambda_{CPW}$ in this particular case. Reciprocity-expression Y_{12} calculations furthermore matched the IE3D results very closely. Starting from this finding, it was established that more



accurate (*i.e.*, “irregular” in the above sense) Y_{12} curves for the resonant-length slots (referred to the centres of radiating slots) can be obtained from the reciprocity-expression approach as follows. First, identify a set of reference planes (and corresponding feed line lengths) for which Y_{11} against d is essentially constant (*e.g.*, $0.4\lambda_{CPW}$ in the above case). Second, since the reciprocity-expression assumption of unchanging self-admittances would be valid, determine Y_{12} with respect to the new reference planes using the reciprocity-expression method; this of course includes a once-off moment-method analysis of the corresponding isolated slots, which for each slot could yield the isolated self-admittance Y_{self} in addition to the terminal voltage and electric field. Finally, construct an approximate Y parameter matrix from Y_{self} and Y_{12} for each value of d , and transform it to the desired $l_f = 0.5\lambda_{CPW}$ reference planes.

Using the reciprocity-expression approach, it was possible to estimate external and internal contributions to the mutual admittance. For the reference substrate, the internal contribution clearly was predominant with a magnitude of more than double that of the external mutual admittance. The relative size of the internal mutual admittance increased as the dielectric thickness of the top layer was increased. The predominance of internal mutual admittance is contrary to the case of longitudinal slots in the broad wall of rectangular waveguide, where in general the external coupling is most pronounced [19,20].

For the purposes of experimental verification, Y_{12} was computed against frequency for a fixed twin slot configuration on one of the above conductor-backed two-layer substrates using both of the above methods. The antenna was manufactured and its S parameters measured; when converted to Y parameters, the measured Y_{12} agreed well with computations using the reciprocity-expression approach and IE3D.

In conclusion, the present chapter reveals the reciprocity-based approach for mutual admittance calculations between CPW-fed slots on a two-layer parallel-plate substrate to be a viable alternative to a moment-method-based approach. The reciprocity-expression approach would however be significantly simpler to implement in an array design procedure.